



Modelling of the characteristics of iron ore granules formed during the granulation process of mixtures that contain concentrate and micropellets

By Mutombo Alain Nyembwe

A dissertation submitted for the degree

Philosophy Doctor

Department of Materials Science and Metallurgical Engineering
University of Pretoria

February 2017

Certification

By submitting this thesis in fulfilment of the requirements for the award of Philosophy Doctor in the School of Engineering, Department of Materials science and Metallurgical Engineering, Faculty of Engineering, Built Environment and Information Technology, University of Pretoria, I state that this thesis is entirely my own work unless otherwise referenced. I have not previously submitted this thesis for a degree at this or any other tertiary institution.

Signature

Mutombo Alain Nyembwe

February 2017

Summary

The depletion of high-grade lump ore and increased blast furnace productivity with the use of prepared burden have resulted in increased use of iron ore sinter and pellets. There is considerable interest in including fine iron ore concentrate and micropellets into raw material mixtures. These materials need to be accommodated in the mixture without adversely affecting the permeability of the sinter bed.

Addition of fine concentrate and micropellets to the raw material mixture will significantly affect the particle size distribution of the granules in the sinter feed. Finer materials form less permeable sinter beds and consequently can reduce the productivity of the sinter plant. The most convenient technique of converting fine ores into a useful sinter feed is granulation. This process consists of the mixing of raw materials (iron ore fines, return fines, fluxes and coke breeze) in a drum granulator for several minutes with the addition of moisture. The granules produced are considered semi-products, whose properties must be monitored in order to achieve improved bed permeability in the sintering process.

In this thesis, the granule size distribution was predicted via the mathematical model of Litster. The auto-layering process was found to be the main mechanism of granulation, whereby finer material adheres around large particles. Litster's model was applied to the ore mixtures with four mass fractions of concentrate and micropellets. The results obtained indicated that the predicted size distributions of granules are in good agreement with the experimental data.

The analysis of the granule shape is a challenge in iron ore sinter. X-ray microtomography was used to capture the three-dimensional shape of the granules. Different shape parameters were used in the characterisation of the granule shape. The results showed that the shape factor and sphericity increase with the addition of concentrate and micropellets. Zingg's diagram was also used as a tool to estimate the overall shape of granules from granulated mixtures.

The pressure drop through the green granule bed was modelled by coupling Rocky DEM (Discrete Element Method) and Fluent CFD (Computational Fluid Dynamics). Systems of mono and bi-sized glass beads were used to validate the applicability of the developed DEM – CFD model to packed beds in a permeameter. Comparisons resulted in good agreement between the predicted and measured pressure drops for both systems of glass beads. The deviations were within $\pm 10\%$. Ergun's equation could not satisfactorily describe the experimental results, with deviations beyond $\pm 20\%$.

Coupled DEM – CFD simulations were extended to granulated mixtures that contain concentrate and micropellets. The importance of the stiffness, friction, size distribution and shape of granules was investigated. The size distribution was truncated at 0.5 mm size fraction to reduce the number of DEM particles and computational costs. A parametric analysis of the DEM parameters was also investigated to determine the reliable values of stiffness and adhesion force fraction and particle shape. The stiffness was adjusted for mixtures with addition of concentrate and micropellets. A good agreement between the predicted and measured pressure drops was achieved.

Acknowledgements

All the Glory belongs to the Mighty One, my Lord Jesus Christ, for been there for me every single moment in this journey.

This PhD program gave me the opportunity to grow up professionally and work with very smart people. But what is most important is that I had the opportunity to discover a scope where most metallurgical processes can be modelled.

For this reason I would like to thank my supervisors, Prof. Andrie Garbers-Craig and Dr. Robert Cromarty for their support and for giving me the opportunity to travel during my PhD. I am grateful to both of you for your advice and encouragement. Thank you also to all members of the Centre for Pyrometallurgy for their moral support. I truly enjoyed the time I shared with you guys.

I would like to thank all the personnel of Anglo American Kumba Iron Ore for assisting me with all experimental tests. Thank you especially to Kobus Vreugdenburg and Andre Dippenaar for your help with my research and my experiments. Thank you to Anglo American Kumba Iron Ore for funding this project.

Thank you to Frikkie de Beer and Robert Nshimirimana for enabling me to carry out the particle shape analysis using X-ray micro-tomography in their department at NESCA. You have been helpful for the time I spent with you.

Thank you to all members of my family!

Table of contents

Certification	I
Summary	II
Acknowledgements	IV
Table of contents	V
Table of Figures	XI
List of Tables	XV
Nomenclature	XVII
List of publications	XXI
1. Introduction	1
1.1. Granulation for iron ore sinter	1
1.2. Objectives of this study	2
1.3. Outline of the Thesis	3
2. Literature Review	5
2.1. Granulation	5
2.2. Mechanisms of granulation for iron ore sinter	7
2.3. Parameters of granulation	10
2.3.1. Properties of the primary particles	10
2.3.1.1. Feed particle size distribution	10
2.3.1.2. Shape of primary particles	12
2.3.1.3. Porosity of primary particles	12
2.3.2. Moisture content	12
2.4. Granulator devices	15
2.5. Permeability of the sinter bed	16
2.5.2.1. Size of granule	18
2.5.2.2. Shape of granules	21

2.5.2.3. Void fraction of the bed	21
2.5.2.4. Angle of repose	22
3. Experimental work.....	24
3.1. Experimental	24
3.1.1. Raw materials.....	24
3.1.2. Raw material mixtures before granulation	26
3.1.3. Granulation	28
3.1.4. Pressure drop measurement	29
3.1.5. Granule size distribution	30
3.1.6. Void fraction of the granulated mixture	31
3.1.7. Measurement of the angle of repose	32
3.1.8. Stereo microscopy.....	32
3.2. Results and discussion	32
3.2.1. Permeability – moisture correlations	35
3.2.2. Effect of concentrate addition on green bed permeability.....	37
3.2.3. Effect of micropellet addition on green bed permeability	38
3.2.4. Factors affecting the green bed permeability.....	39
3.2.4.1. Mean granule size	39
3.2.4.2. Voidage.....	40
3.2.4.3. Angle of repose	42
3.3. Conclusions.....	43
4. Study of structure and shape of granules produced during granulation of mixtures with addition of concentrate and micropellets	45
4.1. Introduction	45
4.2. X-ray microtomography.....	46
4.3. Analysis of three-dimensional particle shape	47

4.4. Experimental	52
4.4.1. Iron ore granules	52
4.4.2. X-ray microtomography analysis of granules.....	53
4.5. Results and discussion	54
4.5.1. Structures of granules	54
4.5.2. Three-dimensional shape of granules	57
4.5.2.1. Evaluation of the sphericity of each granule.....	57
4.5.2.2. Mean value of each shape parameter for the granulated mixture ..	60
4.5.3. Effect of the granule shape on the green bed permeability	62
4.5.4. Sphericity distribution using the Zingg diagram	64
4.6. Conclusion	66
5. Prediction of the granule size distribution of iron ore sinter feeds that contain concentrate and micropellets	68
5.1. Introduction	68
5.2. Background to Litster’s model	69
5.3. Materials and methods	73
5.3.1. Raw materials and mixtures before granulation	73
5.3.2. Partitioning of each particle size to different granule size fractions	74
5.3.3. Structural analysis of granules	74
5.4. Results and discussion	74
5.4.1. Particle partition distribution	74
5.4.2. Comparison of Litster’s model to measured data	76
5.4.3. Variation of partition coefficient parameter $x_{0.5}$ and granule growth with addition of concentrate and micropellets.....	80
5.5. Conclusions.....	83
6. Numerical validation of the pressure drop across glass bead beds using Rocky DEM – Fluent CFD coupling.....	84

6.1. Introduction	84
6.2. Background	85
6.2.1. Mathematical approach	86
6.2.1.1. Void fraction	86
6.2.1.2. Pressure drop calculation.....	89
6.2.2. Numerical approach	90
6.2.2.1. Discrete Element Method (DEM)	91
6.2.2.2. Computational Fluid Dynamics (CFD).....	92
6.3. Experimental procedure	95
6.3.1. Characterisation of glass beads	95
6.3.2. Numerical simulation procedures	97
6.3.3. Simulation of angle of repose	99
6.4. Results and discussion	100
6.4.1. Comparison between measured and simulated static friction of glass beads	100
6.4.2. Predicted void fractions by DEM simulations and mathematical correlations	101
6.4.3. Influence of mesh size on pressure drop.....	105
6.4.4. CFD Model Validation for monosized glass beads	107
6.4.5. Pressure drop through binary mixtures	108
6.4.6. Scale down of the packed bed of glass beads	110
6.4.7. Comparison with Ergun's equation	112
6.5. Conclusions.....	113
7. DEM – CFD coupling simulation of the pressure drop through a packed bed of iron ore granules	115
7.1. Introduction	115
7.2. Key parameters of DEM – CFD coupling method	117

7.2.1. Numerical simulation of packed bed.....	118
7.2.1.1. Inter-particle forces	119
7.2.1.2. Particle size distribution	122
7.2.1.3. Particle shape	123
7.2.2. Fluid flow simulation	123
7.3. Numerical simulation configuration	124
7.4. Results and discussion	125
7.4.1. DEM – CFD simulations for the base mixture.....	125
7.4.1.1. Effect of spring stiffness (Young's modulus)	125
7.4.1.2. Effect of adhesion force (force fraction)	126
7.4.1.3. Effect of fine size fraction	127
7.4.1.4. Effect of granule shape	129
7.4.2. DEM – CFD simulations for mixtures with concentrate and micropellets	131
7.5. Conclusions.....	134
8. Conclusions	136
8.1. Introduction	136
8.2. Conclusions.....	136
8.2.1. Experimental and analytical studies	136
8.2.2. DEM – CFD simulations	138
9. Recommendations for future work	141
REFERENCES.....	142
Appendix A.....	157
Chemical analysis of iron ores and concentrate and raw material mixtures	157
Appendix B.....	159
Material transfer between the size fractions	159

Appendix C.....	163
Particle partition distribution	163
Appendix D.....	168
Comparison between initial particle size distributions (PSD) and calculated particle size distributions from partition tests for raw material mixtures with concentrate and micropellets	168
Appendix E.....	170
X-ray microtomography images of granules from granulated mixtures with addition of concentrate and micropellets	170
Appendix F	172
Validation of the pressure drop through glass beads: Two-way coupling simulation	172
Appendix G	174
Comparison of the predicted and measured pressure drops through granulated mixtures.....	174
Appendix H.....	176
Particle size segregation at the top and base of the packed beds	176

Table of Figures

Figure 1.1. Flow scheme for a sinter plant (Hu and Rose, 1993)	1
Figure 2.1. Particle size distribution before and after granulation (Ball et al., 1973; Voice et al., 1953)	5
Figure 2.2. Images showing the mechanism of granulation (Newitt and Conway-Jones, 1958; Rumpf, 1958)	7
Figure 2.3. Schematic representation of granulation for iron ore sinter showing: a) exclusion of intermediates from the layering process; b) two-stage auto-layering	9
Figure 2.4. Schematic representation of different liquid bridge regimes in a wet particulate system (Newitt and Conway-Jones, 1958; Rumpf, 1958)	13
Figure 2.5. Bed permeability as the function of moisture content (Ball et al., 1973; Voice et al., 1953)	14
Figure 2.6. Effect of moisture content on granule size (Litster et al., 1986).....	15
Figure 2.7. Schematic representation of a granulator (Sherrington and Oliver, 1981)	16
Figure 3.1. Images of raw materials a) fine iron ore (< 10 mm particle size); b) concentrate (< 100 μm particle size); c) micropellets (< 5 mm particle size)	25
Figure 3.2. Particle size distribution of fine iron ore, concentrate and micropellets ..	26
Figure 3.3. Image showing a bench - scale tumbling drum	29
Figure 3.4. Schematic representation of the permeability/pressure drop test.....	30
Figure 3.5. Angle of repose for granulated mixtures where granules are sticky	32
Figure 3.6. Stereo microscopic images of produced granules (5.5% moisture content): a) base case; b) with concentrate addition; c) with micropellet addition	35
Figure 3.7. Effect of (a) concentrate and (b) micropellet addition on green bed permeability	36
Figure 3.8. Variation of the maximum permeability with concentrate and micropellet addition.....	37

Figure 3.9. Variation of mean granule size with concentrate and micropellet addition at optimum moisture content	40
Figure 3.10. Variation of voidage with concentrate and micropellet addition	41
Figure 3.11. Variation of angle of repose with (a) concentrate and (b) micropellet addition.....	43
Figure 4.1. Shape description of aggregate: form (dashed ellipse), roundness (dashed circle), and texture (short dashed circles) (Barrett, 1980).....	48
Figure 4.2. Chart for visual evaluation of roundness (Krumbein, 1941).....	49
Figure 4.3. Granule shape based upon morphological observations (Powers, 1953)	49
Figure 4.4. The principal dimensions of an aggregate particle (Erdoğan, 2003)	50
Figure 4.5. Description (a) particle forms using the Zingg diagram (Zingg, 1935) and (b) iso- sphericity curves defined by Krumbein and Sloss (1963).....	52
Figure 4.6. Nikon XTH/225-ST Microfocus X-ray microtomography system	53
Figure 4.7. Schematic experimental setup of the X-ray microtomography (De Beer, 2005).....	54
Figure 4.8. X-ray microtomographs of granules a) base case; b) with concentrate addition; c) with micropellet addition	55
Figure 4.9. Group distribution of granules from ore mixtures with addition of (a) concentrate and (b) micropellets	57
Figure 4.10. Images of granules (base case) captured by X-ray microtomography .	58
Figure 4.11. Mean values of true sphericity, operational sphericity, Krumbein sphericity, Corey shape factor and Janke form factor for granules with a) concentrate and b) micropellets	61
Figure 4.12. Mean sphericity of the granulated mixtures with concentrate and micropellets	62
Figure 4.13. Effect of concentrate and micropellet addition on the mean sphericity and bed permeability	63
Figure 4.14. Variation of granule shape using Zingg's diagram	65

Figure 4.15. Sphericity distribution of the population of the granules from base mixture and mixtures with concentrate and micropellet addition	66
Figure 5.1. Variation of the ratio R with concentrate and micropellet addition at optimum moisture content	77
Figure 5.2. Comparison of model predicted and experimental granule size distributions for the different mixtures: (a): base case; (b) to (e): 10% - 40% concentrate; (f) to (i): 10% - 40% micropellets.	79
Figure 5.3. Comparison of model predicted and experimental granule sizes for the different mixtures. ●: base case; ■: concentrate; ▲: micropellet.	80
Figure 5.4. Effect of concentrate and micropellet addition on the partition coefficient parameter $x_{0.5}$	81
Figure 5.5. Variation of the granule growth with addition of concentrate and micropellets	82
Figure 6.1. Void fractions of bi-sized packed beds. ϵ_1 and ϵ_2 are void fractions of mono sized packing (Furnas, 1929)	87
Figure 6.2. Experimental test of pile formation (3 mm diameter glass beads, 150 mm diameter of the plate)	96
Figure 6.3. Schematic representation of the simulation model for packing of 3 mm glass beads into a permeameter	98
Figure 6.4. Rocky DEM simulation of pile formation test after release (3 mm diameter beads, 60 mm diameter of the tube, 150 mm diameter of the plate)	100
Figure 6.5. Comparison between measured and simulated coefficients of static friction.....	101
Figure 6.6. Comparison of predicted and measured void fractions. Rocky DEM, Dixon's and Furnas's equation used to predict void fraction	103
Figure 6.7. Comparison of predicted and calculated void fractions of beds randomly packed with binary mixtures of 3 mm and 6 mm glass beads	104
Figure 6.8. Effect of mesh size on pressure drop through the glass beads.....	106

Figure 6.9. Variation in deviation (error) between the simulated and measured pressure drop with mesh size..... 107

Figure 6.10. Comparison between pressure drops obtained with 36 mm and 48 mm mesh size for binary mixtures of glass beads..... 110

Figure 7.1. Two-particle contact with overlap in normal direction. r_i and r_j are the positions of particles i and j respectively. 118

Figure 7.2. Spring dashpot model for contact forces between particles 119

Figure 7.3. Contact bond model for a sticky material 120

Figure 7.4. Variation of pressure drop with adhesion force (force fraction) 127

Figure 7.5. Variation of pressure drop with particle shape 130

Figure 7.6. Variation of size fraction with the addition of concentrate and micropellets 132

Figure 7.7. Variation of the number of DEM particles with the addition of concentrate and micropellets 133

Figure 7.8. Comparison between the measured and predicted pressure drops through granulated mixtures with addition of concentrate and micropellets 134

List of Tables

Table 2.1. Typical definitions of particle size (Allen, 1990).....	20
Table 3.1. Compositions of the raw material mixtures.....	27
Table 3.2. Particle size distributions of the raw material mixtures	27
Table 3.3. Ratios between mass size fractions	28
Table 3.4. Permeability and voidage of granulated mixtures.....	33
Table 4.1. Correlation of Shape factor of 3D particle shape (Corey, 1949; Janke, 1966; Krumbein, 1941; Wadell, 1933, 1932).....	51
Table 4.2. Classification based on ratios W/L and T/W (Zingg, 1935).....	52
Table 4.3. Geometric characteristics of granules from the base case sample	58
Table 4.4. Sphericity and shape factors of the selected granules from base case..	59
Table 4.5. Number of the selected granules.....	60
Table 5.1. Sauter mean diameter (SMD) for examined mixtures before granulation	73
Table 5.2. Particle partition distribution of the base case sample at 5.5% moisture.	75
Table 5.3. Partition coefficient of particle size fraction	76
Table 6.1. Measured properties of glass beads of different sizes	95
Table 6.2. Measured angles of repose and coefficients of static friction of different glass bead sizes.....	96
Table 6.3. Restitution coefficient of glass beads of different glass bead sizes	97
Table 6.4. Interaction properties of glass beads.....	102
Table 6.5. Void fractions of the packed beds	102
Table 6.6 Calculated and predicted void fractions in binary mixtures of 3 mm and 6 mm glass beads	104
Table 6.7. Comparison between simulated and measured pressure drops for monosized glass beads.....	108
Table 6.8. Comparison of measured pressure drop and predicted pressure drop for binary mixtures of 3 mm and 6 mm glass beads	109

Table 6.9. Column-to-glass bead diameter ratio and glass bead diameter-to-packing height ratio of full and reduced scale packing.	111
Table 6.10. Deviation of the simulated pressure drop across full and reduced scale packed columns	111
Table 6.11. Deviations between measured and predicted pressure drop using Ergun’s equation and MacDonald’s equation	112
Table 7.1. Input parameters for DEM-CFD simulation.....	125
Table 7.2. Comparison of measured pressure drop and predicted pressure drop for different Young’s modulus parameters.....	126
Table 7.3. Mass percentage of full and truncate size distributions for base case...	128
Table 7.4. Comparison between simulations with full and truncated size distribution	129
Table 7.5. Examined shapes of DEM particles.....	129
Table 7.6. Parameters for DEM - CFD simulations	133

Nomenclature

Roman symbols

A	: Cross sectional area
A_p	: Projected area of particle
A_{adh}	: Adhesion force between two bonded spherical bodies
C_d	: Drag coefficient
D	: Diameter of the cylinder (tube)
d_i	: Diameter of size fraction i
d_l	: Length mean diameter
d_s	: Surface mean diameter
d_v	: Volume mean diameter
d_{pi}	: Mean granule diameter for size fraction i
d_{sv}	: Diameter of a sphere of the same volume as particle
d_{cir}	: Diameter of the circumscribed sphere
d_{s_g}	: Sauter mean diameter after granulation
d_{s_exp}	: Experimental Sauter mean diameter
d_{s_feed}	: Sauter mean diameter before granulation
d_{s_pred}	: Predicted Sauter mean diameter
d_{32}/d_p	: Sauter mean diameter
e	: Base of the natural logarithm
E_0	: Energy of the intensity beam
$E_{kin,imp}$: Initial kinetic impact energy
$E_{kin,reb}$: Elastic energy released during the rebound of the particle
F	: Flow-rate of gas (air)
F^d	: Drag force applied by a single particle on the fluid phase
F_i	: Total force acting on the particle i
F_n	: Normal contact force
F_t	: Tangential contact force
F^T	: Momentum transfer between particles and fluid
F_{ci}	: Interactions between the environment and the particle i
f_{ad}	: Adhesion force fraction
$F_{n,adh}^t$: Normal adhesive contact force at the current time
g	: Gravitational acceleration

h	: Height above a flat surface before the release of the particle
H	: Height of the bed
h_{reb}	: Rebound height reached by the particle
I	: Transmitted intensity of the radiation beam
I_i	: Moment of inertia of the particle i
I_0	: Intensity of the incident beam
K	: Parameter that relates layer thickness to the mass of adhering particles
k	: Spring stiffness
k_a	: Adhesive coefficient
k_n	: Normal stiffness
k_t	: Tangential stiffness
k_1/k_2	: Ergun coefficients
L	: Length of the sample
m_i	: Mass fraction of size fraction i
m_{ij}	: Reduced mass of particles i and j
M_{ij}	: Mass of particles of size fraction i in granules of size fraction j
M_{tot}	: Total mass of the flask filled with kerosene and granules
M_{ker}	: Mass of the flask filled with 500 ml of kerosene
n	: Exponent
P	: Pressure drop
R	: Ratio of the adhering layer to nuclei that is independent of particle size
R_i	: Ratio of the adhering layer to nuclei for granules in size fraction i
Re_p	: Particle Reynolds number
$R_{L/f}$: Ratio of large to fine particles
r_i	: Position of the particle i
r_j	: Position of the particle j
s	: Surface of a sphere of the same volume as particle
S	: Surface of particle
T	: Thickness of the sample
T_i	: Torque acting on the particle i
u	: Velocity of particle
v_i	: Velocity of a particle i
V_m	: Volume of kerosene required to fill the flask up to the 1 litre mark
v_n	: Normal velocity of the particle
v_s	: Superficial velocity of gas (air)

V_t	: Tangential velocity of the particle
W	: Width of the sample
w_i	: Angular velocity of the particle i
w_{ik}	: Weight percent of feed component k in size fraction i .
W_{gi}	: Mass fraction of granule in size fraction i
X_f	: Mass percentages of fine particles
x_i	: Top size of particle (feed) size fraction i
x_{gi}	: Top size of granule size i
$x_{0.5}$: Particle size with a partition coefficient of 0.5
\bar{x}_i	: Geometric mean size of the size fraction i
Z	: Atomic number

Greek symbols

α_i	: Partition coefficient of particles of a given size i
α_f	: Fluid mass percentage,
α_s	: Mass percentage of particles
$\alpha(x)$: Partition coefficient function
β	: Dashpot ratio
δ	: Overlap between two particles in contact
δ_k	: Weight percent of component k in the feed
δ_n	: Normal overlap between two particles
δ_n^t	: Contact normal overlap value at the previous time
δ_n^{t-dt}	: Contact normal overlap value at the previous time
δ_{adh}	: Maximum overlap beyond which there is no adhesion between particles
δ_0	: Overlap when the adhesion force equals to 0
Δ_i	: Layer thickness around particle of size fraction i
$\Delta\delta_n$: Difference between the contact normal overlap values
ε	: Void fraction
ε_f	: Void fraction of the single sized particles
ε_L	: Void fractions of the single sized large particles
ε_r	: Coefficient of restitution
ε_{min}	: Minimum void fraction of the binary packing
ε_{mix}	: Void fraction in a binary packing

- η : Dashpot coefficient
- μ : Viscosity of gas (air)
- μ_s : Friction coefficient
- ρ_a : Apparent (skeleton) density
- ρ_b : Bulk density
- σ : Partition curve parameter
- φ : Sphericity or shape factor
- ϕ_i : Lumped parameter for each size fraction i

List of publications

Contribution to Journals

- A.M. Nyembwe, R.D. Cromarty, A.M. Garbers-Craig, Prediction of the granule size distribution of iron ore sinter feeds that contain concentrate and micropellets, *Powder Technology*, 295 (2016) 7 - 15.
- A.M. Nyembwe, R. Cromarty, A.M. Garbers-Craig, Effect of concentrate and micropellet additions on iron ore sinter bed permeability, *Mineral Processing and Extractive Metallurgy*, 125 (2016) 178 - 186.
- AM Nyembwe, R Cromarty and AM Garbers-Craig, Relationship between iron ore granulation mechanisms, granule shapes and sinter bed permeability, *Mineral Processing and Extractive Metallurgy Review*, Published online: 22 May 2017.
- AM Nyembwe, R Cromarty and AM Garbers-Craig, RockyDEM - CFD coupling for simulations of the pressure drop across randomly packed glass beads, under review, 2017.
- AM Nyembwe, R Cromarty and AM Garbers-Craig, Application of RockyDEM - CFD coupling to the measurement of the pressure drop across a packed bed of iron ore granules containing concentrate and micropellets, under review, 2017.

Contribution to conferences

- A.M. Nyembwe, R. Cromarty, A.M. Garbers-Craig, Effect of concentrate and micropellet additions on iron ore sinter bed permeability, In: *Proc. Iron Ore 2015 – Maximising Productivity*, 13-15 July 2015, Perth, Western Australia, 2015.

1. Introduction

1.1. Granulation for iron ore sinter

Granulation is the first stage in the agglomeration of iron ore for sinter production. Fine iron ores, fluxes, coke breeze and other fine materials (collected dusts, mill scale) are mixed together to form large and bigger agglomerates. The granulation process of iron ore is commonly performed in a tumbling drum and agglomerated material is loaded onto a permeable sinter strand grate. The top of the bed is then raised to a high temperature, using gas burners, while air is sucked through the permeable grate. After ignition, combustion zone is drawn downwards through the sinter bed. In the combustion zone the granules are heated to between 1250 °C and 1350 °C resulting in partial melting. On cooling the liquid phase bonds the grains resulting in the formation of a solid sinter. The final stage is the reduction of sinter into hot metal (Ball et al., 1973; Ellis et al., 2007; Ennis and Litster, 1997; Formoso et al., 2003; Khosa and Manuel, 2007; Litster and Waters, 1988; Loo et al., 1992; Voice et al., 1953). A schematic representation of the production of sinter is given in Figure 1.1.

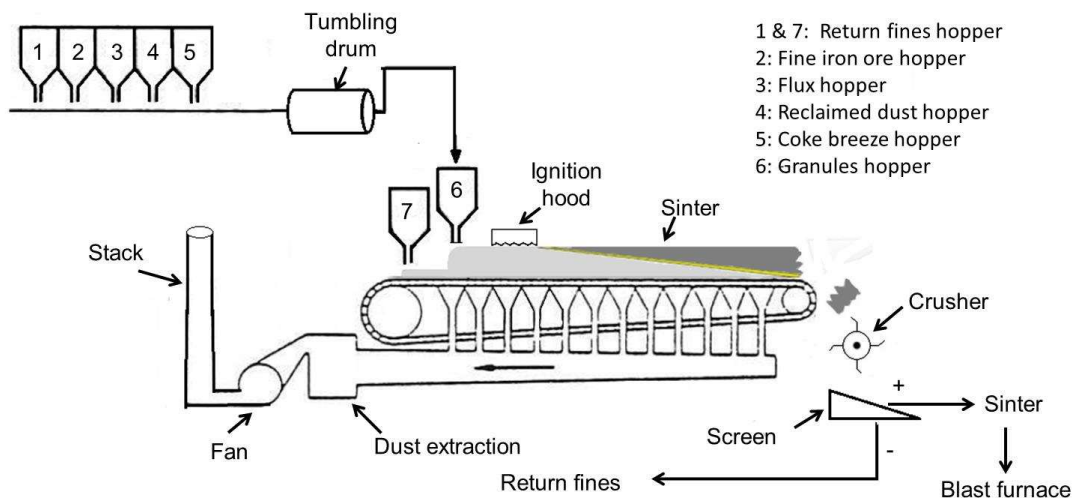


Figure 1.1. Flow scheme for a sinter plant (Hu and Rose, 1993)

The primary objective of the granulation process is to produce granules with a large mean size and narrow size distribution, which can form packed beds with improved permeability and higher gas flow. This promotes better gas-solid heat transfer and increase productivity of the sinter plant. Previous studies reported that the properties of granules (size and shape) can strongly influence the structure of the sinter bed, and consequently the bed permeability (Ellis et al., 2007; Formoso et al., 2003; Hinkley et al., 1994a; Khosa and Manuel, 2007; Litster and Waters, 1988). For instance, fine granules will likely form a sinter bed with lower bed permeability than that of coarse granules. It is therefore important to analyse and monitor the granule properties in order to improve the permeability of the sinter bed and productivity of the sinter plant.

1.2. Objectives of this study

Experiments have provided useful insights into the green bed permeability or pressure drop (Ball et al., 1973; Ellis et al., 2007; Ennis and Litster, 1997; Formoso et al., 2003; Khosa and Manuel, 2007; Litster et al., 1986; Litster and Waters, 1988; Loo et al., 1992; Voice et al., 1953; Waters et al., 1989). A broader particle size distribution of iron ore (0 – 8 mm particle size) promotes the formation of large granules by adherence of fines around coarse particles and this results in an increase in the voidage and permeability of the packed bed. Whilst it is well known that the particle size distribution of iron ore affects the granule size and bed permeability, the effect of concentrate and micropellet addition in the raw material mixture is still not well established.

The experimental tests used to measure the permeability of the sinter bed are usually non-repeatable due to a potential disintegration of moist granules (Ball et al., 1973; Hinkley et al., 1994a; Rankin et al., 1985; Voice et al., 1953). Ergun's equation is used to predict the permeability of the sinter bed even though its applicability is limited to spherical particles (Hinkley et al., 1994a; Rankin et al., 1985; Rankin and Roller, 1985). To mitigate the inherent errors in the prediction of the pressure drop, another approach is to conduct a limited number of experimental tests that can verify and validate numerical simulation models.

The scope of this research involves the applicability of Litster's model to raw material mixtures that contain concentrate and micropellets, and simulation of the pressure drop across a sinter bed using a well-developed discrete-continuum coupling algorithm (DEM - CFD). The DEM model is used to simulate a packed bed of granules, while a coupled DEM – CFD model is used to simulate the fluid-solid interactions (pressure drop). This study mainly focusses on:

- Effect of concentrate and micropellet addition on iron ore green bed permeability.
- Prediction of the granule size distribution of iron ore sinter feeds that contain concentrate and micropellets.
- Application of a coupled DEM – CFD model to the prediction of the pressure drop and/or permeability of granulated mixtures consisting of moist granules with randomly distributed irregular shapes and sizes. Packed beds of glass beds are used to validate the numerical simulation models. The effects of the granule size distribution, shape and interactions between granules are discussed in this study.

1.3. Outline of the Thesis

This thesis is organized as follows:

Chapter 2 summarises a literature review on topics related to the granulation process. Detail of iron ore granulation and experimental parameters are discussed. Theories on mechanisms of granulation are reviewed with an emphasis on the mechanism that occurs in iron ore granulation.

In Chapter 3, experimental work is described. Granulation was carried out in a bench-scale tumbling drum. The influence of partial replacement of fine iron ore by concentrate and micropellets on granule properties is discussed.

Chapter 4 contains the definitions and analyses for three-dimensional shapes of granules. X-ray microtomography was used for analysis of iron ore granules to obtain new information about the morphology, which includes microstructure and sphericity.

In Chapter 5, the application of the model of Litster is reviewed. Granule size was computed by extending the model of Litster to raw material mixtures that contain concentrate and micropellets.

Chapter 6 deals with the validation of coupling Rocky DEM with Ansys Fluent CFD using mono and bi-sized glass beads. The void fraction and pressure drop through glass beads with different sizes were calculated. Predicted values of pressure drop were further compared to those calculated by Ergun and MacDonald's equations.

In Chapter 7, two-way DEM – CFD coupling model is applied to the calculation of the pressure drop through granulated mixtures with addition of concentrate and micropellets. Effects of stiffness, adhesion force, angle of repose, size distribution and shape parameter of the granulated material were investigated. Simulation results were compared against experimental measurements.

Chapter 8 completes the thesis by drawing the main conclusions of this research.

Recommendations for further work are presented in Chapter 9.

2. Literature Review

The goal of this chapter is to review previous studies that are related to the granulation of iron ore. Experimental work performed and models developed on the prediction of the granule size distribution are also reviewed.

2.1. Granulation

Granulation is widely used in many industries such as pharmaceuticals, agriculture, mineral processing and sinter making. It is a technique of size enlargement for a mixture of fine particles to form larger, multiparticle entities called granules (Ball et al., 1973; Ellis et al., 2007; Ennis and Litster, 1997; Formoso et al., 2003; Khosa and Manuel, 2007; Litster and Waters, 1988; Loo et al., 1992; Voice et al., 1953). The particle size distribution is therefore described as the major parameter to assess the effectiveness of granulation (Ball et al., 1973; Ellis et al., 2007; Ennis and Litster, 1997; Formoso et al., 2003; Khosa and Manuel, 2007; Litster and Waters, 1988; Loo et al., 1992; Voice et al., 1953). In general the definition of the granulation is associated with a comparison between the size distributions of the granules before and after granulation (Figure 2.1). It can be seen that the granulation process results in the shift of granule size distribution to larger sizes of granules. Effective granulation also results in improved flow properties (permeability) and reduced dustiness of agglomerated material (Ball et al., 1973; Voice et al., 1953).

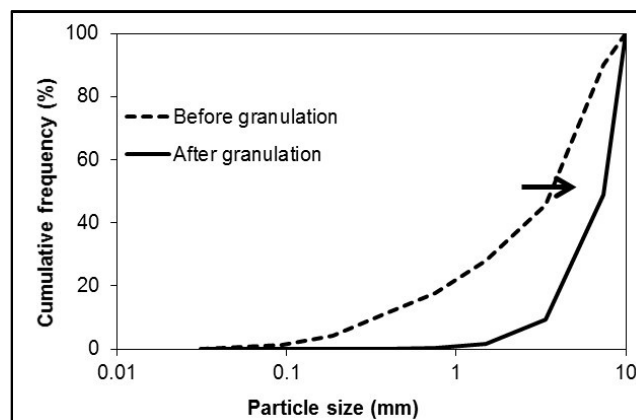


Figure 2.1. Particle size distribution before and after granulation (Ball et al., 1973; Voice et al., 1953)

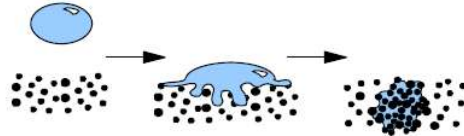
Granulation is often classified into dry granulation or wet granulation. In dry granulation, the granules can be formed by adhesion of particles that takes place because of applied pressure. This process may be used for materials that do not compress well after wet granulation, or those that are sensitive to moisture. Dry granulation first produces intermediate products that are broken and sieved to separate the desired size fraction as granules. Wet granulation is the technique most used in the production of granules. Particle adhesion can occur through the distribution of the granulating fluid into the feed by mechanical agitation created in the granulator. For economical and ecological reasons, water is preferably used as the granulating fluid in wet granulation (Ennis and Litster, 1997; Iveson and Litster, 1998; Litster and Ennis, 2004; Perry et al., 1997; Pietsch, 2002; Salman et al., 2007).

Numerous studies have reported that the understanding of the mechanism of granulation is crucial to model the changes in particle size distribution. Mechanisms where particle size distribution evolves were studied for granulation processes with narrow size distributions (Ennis and Litster, 1997; Iveson et al., 2001; Iveson and Litster, 1998; Litster and Ennis, 2004; Sastry and Fuerstenau, 1973). It was then found that the size enlargement is essentially controlled by the granule growth, which occurs either by collision and successful adherence between particles or by growth centred on nucleus particles.

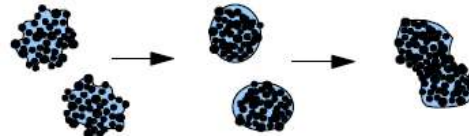
The formation of granules is a function of how narrow or wide the size distribution of primary particles is (Ennis and Litster, 1997; Iveson et al., 2001; Iveson and Litster, 1998; Litster and Ennis, 2004; Newitt and Conway-Jones, 1958; Rumpf, 1958; Sastry and Fuerstenau, 1973). For a narrow size distribution of primary particles, the formation of granules takes place through a three-step mechanism: wetting and nucleation - consolidation and coalescence - breakage and attrition (Figure 2.2). The first sub-mechanism is described as wetting and nucleation where the liquid is distributed throughout the fine material and nuclei (small granules) are formed for further agglomeration. Due to collisions with walls and other granules, air is forced out of the pores and binder (moisture) is forced out to the surface of the granules. This

step is described as consolidation. The presence of the binder layer increases the probability that two colliding granules will coalesce. Consolidation and coalescence occur simultaneously and are both the result of collisions. Breakage and attrition occurs when granules are too large or dry. This step can strongly affect the size distribution of the final product.

➤ Wetting and nucleation



➤ Consolidation and coalescence



➤ Breakage and attrition

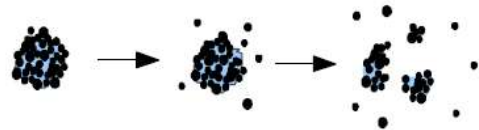


Figure 2.2. Images showing the mechanism of granulation (Newitt and Conway-Jones, 1958; Rumpf, 1958)

In granulation of iron ore for sinter, the primary particle sizes are widely distributed and range from 0 to 8 mm. This leads to another mechanism known as auto layering, where fine particles attach around the surface of the coarse particles to form granules (Kapur et al., 1993; Litster et al., 1986; Venkataramana et al., 1999; Waters et al., 1989).

2.2. Mechanisms of granulation for iron ore sinter

Sinter feed consists of particles with a wide size distribution (< 8 mm). Primary particles are often distinguished in two or three classes according to their relative roles in granulation. Furui et al. (1977) and Vidal et al. (1985) reported that the size distribution of the iron ore can be classified into nuclei (coarse particles), intermediate particles and adhering fines. During the granulation process, iron ore granules are formed by

the adherence of fine particles on the surface of coarse particles. The intermediate sized particles can act as either nuclei or adhering particles, or may not take part in granulation. Litster et al. (1986), Waters et al. (1989) and Rankin et al. (1983) defined a cut-off size where feed particles can act as nuclei or adhering fines, but they did not consider any particle size as intermediate.

Fundamental studies on mechanisms of granulation for iron ore sinter are scarce in the open literature. Litster et al. (1986) proposed that there are two types of auto layering processes: single and two - stage processes. The single auto layering refers to a process whereby finer material adheres onto coarse particles and forms a sticky adhering layer. Here the intermediate particles play no role during the granulation process. A schematic representation of the single auto layering is given in Figure 2.3a.

Litster et al. (1986) and Roller (1982) suggested that the size distribution of fines might promote the two-stage mechanism of the granulation process. Initially, finer material adheres onto nuclei (large) particles and forms a layer which embeds intermediate particles to form bigger granules (Figure 2.3b). Venkataramana et al. (1999) and Kapur et al. (1993) reported that granulation occurs through a two-stage mechanism where the intermediates will take part in granulation as long as there is a sufficient amount of adhering fines present in the system. Fines first adhere onto intermediate and coarse particles and intermediate size granules then start to attach onto coarse granules to produce bigger granules. Litster and Waters (1990) also proposed a two-stage growth mechanism under specific conditions. During the first stage, some intermediate particles change roles from nuclei to layering particles. The second stage is slow and can be enhanced by collisions before intermediate particles are incorporated into the adhering layer.

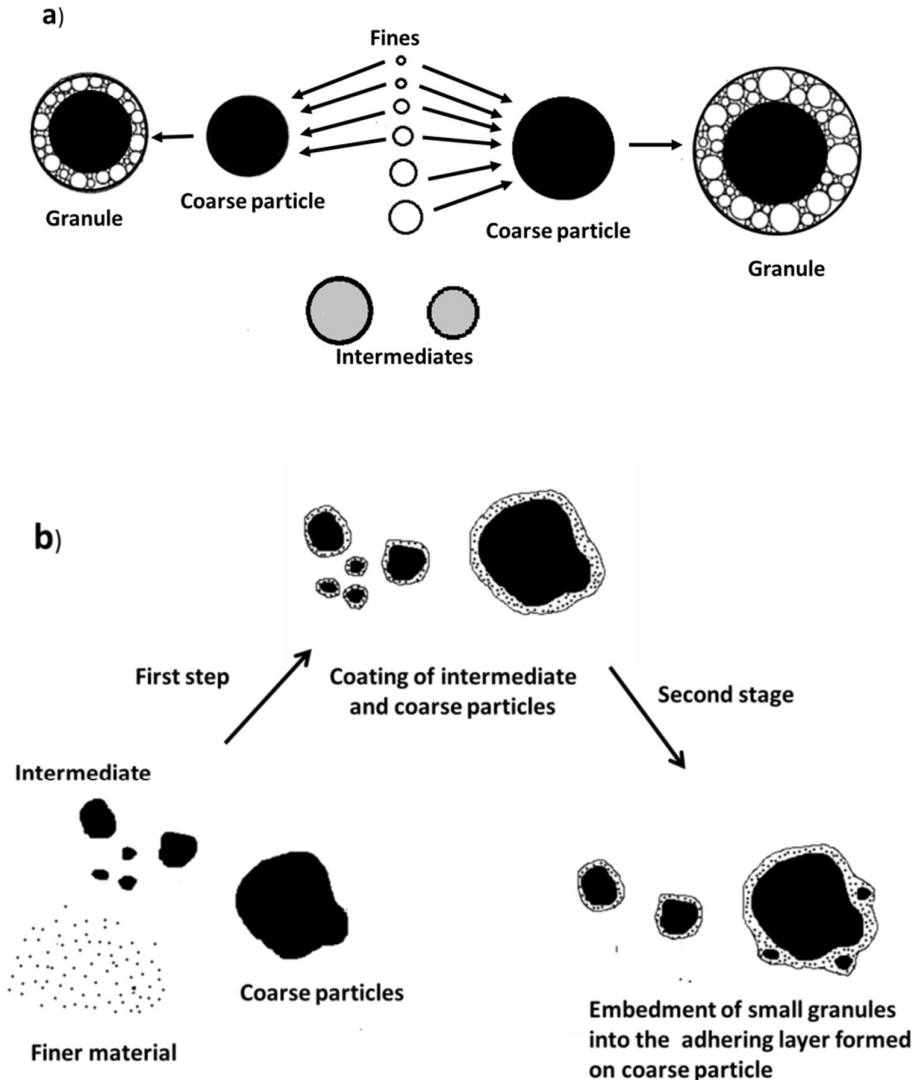


Figure 2.3. Schematic representation of granulation for iron ore sinter showing: a) exclusion of intermediates from the layering process; b) two-stage auto-layering

In granulation of fine iron ore, it was experimentally found that the mechanism that takes place in the formation of granules may deviate from a single elementary mechanism towards a multiple mechanism (Shatokha et al., 2009). This means that the overall mechanism can be a combination of two or more mechanisms. Shatokha et al. (2009) also reported that the addition of more concentrate into sinter feeds could result in two types of mechanisms. One fraction of concentrate can promote a coalescence process resulting in the formation of microgranules with a pellet-like

structure. The other fraction of concentrate can be involved in auto layering of fines onto coarse particles.

2.3. Parameters of granulation

The granulation for iron ore sinter is a complex process due to a large number of process variables and equipment parameters: feed size distribution, particle shape, particle porosity, moisture content and drum diameter. In the current study, the device parameters (drum diameter and filling fraction) were kept unchanged.

2.3.1. Properties of the primary particles

Granulation is principally influenced by the characteristics of the sinter feed such as size distribution, shape and porosity of the particles.

2.3.1.1. Feed particle size distribution

The size distribution of the primary particles has a determinant effect on the mechanisms of the granulation process. The granulation with narrow size distributions of the feed particles takes place in a three-step mechanism: wetting and nucleation – growth and consolidation – attrition and abrasion (Ennis and Litster, 1997; Iveson et al., 2001; Iveson and Litster, 1998; Litster and Ennis, 2004; Newitt and Conway-Jones, 1958; Rumpf, 1958; Sastry and Fuerstenau, 1973). However, a broader size distribution of the initial particles changes the growth mechanism from coalescence towards an auto layering process (Ennis and Litster, 1997; Kapur et al., 1993; Litster et al., 1986; Venkataramana et al., 1999; Waters et al., 1989).

The particle size distribution of iron ore is often classified in three size fractions. Fine particles (< 0.250 mm) adhere onto the surface of large particles (> 0.750 mm) and then form granules called quasi-particles or pseudo - particles. Intermediate particles (0.250 - 0.750 mm) are difficult to granulate and do not have a well-defined role (Formoso et al., 2003; Furui et al., 1977; Vidal et al., 1985). These particles can act

as either nuclei or adhering layer depending on the moisture content. An increase in water content of the ore mixture can cause the intermediate particles to act as adhering fines, which poorly adhere onto the coarse particles, and can detach during the drying stage. The intermediate particles can also act as nuclei and form quasi-particles with small size compared to those formed with coarser nuclei. This can sensibly reduce the permeability of the sinter bed as well as the productivity of the sintering process. Hence the amount of intermediate particles must be minimal to limit the formation of the granules that are either small in size or not strong enough to resist disintegration.

Shatokha et al. (2009) studied the influence of concentrate addition on the granulation mechanisms. The results show that the addition of fine concentrate into the sinter feed can lead to the formation of granules with a pellet-like structure. It was shown that distinct spherical lumps of fines, called “micro-granules”, can form and act as nuclei during the coalescence process. This mechanism of growth resulted in a build-up of fines centred on the surface of the micro-granules as the moisture is added. This means that concentrate can be shared between adhering fines around micro-granules and coarse particles. It was found that the amount of micro-granules is higher with more addition of concentrate. The overall mechanism becomes complex and can range from coalescence to auto layering. The addition of concentrate evidently decreases the ratio of fines to nuclei, resulting in a slow granule growth (Shatokha et al., 2009).

Similarly, Gan et al. (2015) showed the importance of the feed size distribution during the granulation process. The amount of adhering fines was found to be a determinant factor of growth of granules. An increase in fine size fraction can result in an increase in the average diameter of granules and shape factor. It was found that the granule size and sphericity reach a maximum at 40%-50% adhering fines content. Gan et al. (2015) reported that small amounts of adhering fines in the sinter feed can produce granules with a shape similar to that of coarse primary particles. Increasing the fraction of adhering fines can also lead to the formation of mini-pellets (micro-granules) without nucleus particles inside, delaying the granules to grow larger. The amount of adhering

finer particles must therefore be optimised in order to produce large granules, which can result in high bed permeability and high sinter productivity.

2.3.1.2. Shape of primary particles

Although particle size distribution is usually of basic importance in the granulation process, particle shape can have a dominant effect during the granule growth (Hinkley et al., 1994a; Khosa and Manuel, 2007; Litster and Waters, 1988). Particles with well-rounded shape have less probability to agglomerate than rough particles. In addition, primary particles with a high roughness and a low bluntness easily produce granules through the auto-layering process of fine particles around bigger ones.

Gan et al. (2015) found that the shape of the feed particles influences the granulation progress. Irregular and rough particles such as return fines and coke are good nuclei, compared to rounded particles with smooth surfaces.

2.3.1.3. Porosity of primary particles

Previous studies reported that the porosity of sinter feed particles can strongly affect the granulation process (Iveson et al., 2004, 2001; Newitt and Conway-Jones, 1958; Rumpf, 1958; Sastry and Fuerstenau, 1973). Porous material generally requires more added moisture for granulation to progress. It was established that the pores of nuclei particles must be filled with moisture before the adherence of fines onto nuclei begins. If the pores are not filled with water, the surface of the particles may remain dry due to a fast absorption of water into the particles. In practice, it is established that the higher the porosity of primary particles the higher the level of moisture that is required in the granulation process (Iveson et al., 2004, 2001).

2.3.2. Moisture content

The moisture content is a very important parameter in wet granulation since the water is used as binder to promote adhesion between particles. As shown in Figure 2.4,

there are three macroscopic liquid-solid stages in the formation of the granules: pendular, funicular and capillary states (Lv et al., 2010; Matsumura et al., 2009; Newitt and Conway-Jones, 1958; Rumpf, 1958; Sastry and Fuerstenau, 1973). When adding water to a powder mass, particles attach together through capillary pressure and surface tension of the liquid. This stage refers to the pendular state. In the funicular state, the liquid rings in the granules coalesce as the amount of water increases and tend to form a continuous network. The funicular state represents an intermediate stage between the pendular and capillary states. Further addition of water completely fills the void volume of the granules. This is described as the capillary state. Excessive water addition can destroy the liquid – solid bridges and form the droplet state.

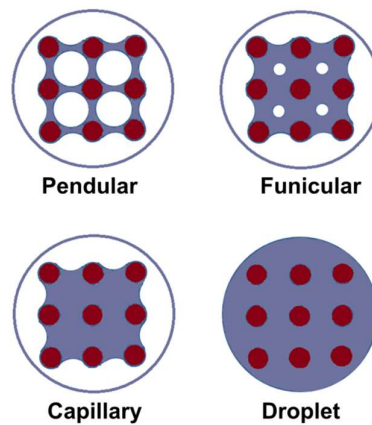


Figure 2.4. Schematic representation of different liquid bridge regimes in a wet particulate system (Newitt and Conway-Jones, 1958; Rumpf, 1958)

In iron ore granulation, it was found that the pendular regime is more likely to be the driving force for the adherence of particles on the surface of coarse ones (Litster et al., 1986; Litster and Waters, 1990). Different particles are then attached together by a liquid bridge. For a porous ore, the added moisture is mostly absorbed into the pores in the ore, reducing the amount of water available for the auto layering of fines (Iveson et al., 2004, 2001; Newitt and Conway-Jones, 1958; Rumpf, 1958; Sastry and Fuerstenau, 1973). This reduction in available moisture content increases the amount of water required for granulation. However, addition of excess added moisture can result in a large amount of free moisture. This completely fills the gaps between ore particles, causing the whole system to the capillary state comparable to a slurry.

The moisture content has a significant influence on determining the role of intermediate particles. Depending on moisture content, the particles of same size can act as either adhering fines or nuclei (Ellis et al., 2007; Khosa and Manuel, 2007; Litster et al., 1986; Litster and Waters, 1990; Rankin et al., 1983). With an increase in moisture content, the intermediate particles act as adhering fines and are poorly adhered to coarser nuclei. Hence, the granules are too weak. The intermediate particles can also act as coarse particles when the moisture content decreases. The amount of adhering fines becomes insufficient for the auto layering process and can only form small granules.

In practice, the moisture content is tuned to an optimum value, which is the least water content added into the mixture, and results in the formation of the granules of a suitable size distribution. This optimum value is of vital importance for sintering and yields a maximum pre-ignition permeability. Based on various experiments, it was established that the bed permeability increases with increasing moisture and reaches a maximum (Figure 2.5). Further addition of moisture decreases the bed permeability (Ball et al., 1973; Ellis et al., 2007; Voice et al., 1953).

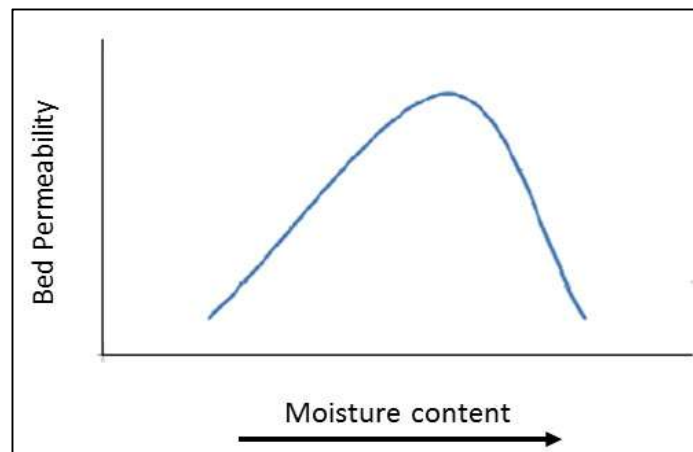


Figure 2.5. Bed permeability as the function of moisture content (Ball et al., 1973; Voice et al., 1953)

In addition, the shift of granule size distribution to larger sizes depends on the moisture content (Litster et al., 1986; Litster and Waters, 1990). For instance, the average granule size d_{50} (the granule diameter under which there are 50 wt% of granules) increases as the moisture content increases (Figure 2.6). This means that raw materials with high water content are much easier to stick together into larger granules.

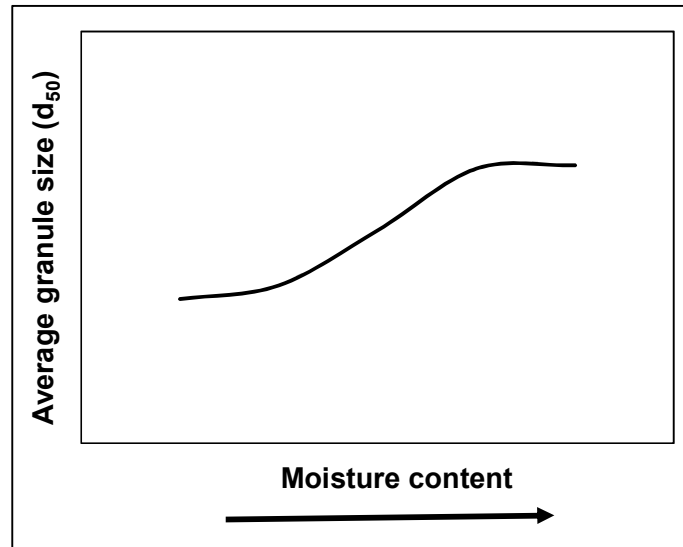


Figure 2.6. Effect of moisture content on granule size (Litster et al., 1986)

2.4. Granulator devices

The granulation process can be carried out in different devices: Shear granulator, pelletiser, mixer and tumbling drum (Brawn et al., 1950). The shear granulator, pelletiser and mixer are generally used for narrow size distributions where collisions between granules are important to produce large granules. In granulation for iron ore sinter, it was found that the tumbling drum is more convenient to promote successful adherence of fines around coarse particles (Perry et al., 1997; Pietsch, 2002; Salman et al., 2007; Sherrington and Oliver, 1981). A schematic representation of a tumbling drum is shown in Figure 2.7. It consists of a rotating cylinder, which is slightly inclined to the horizontal to facilitate the transportation of material through the drum. The drum is usually equipped with a dam ring to minimise back-spill of the inlet material. At the outlet of the drum, there is often another dam ring, which allows an increase in depth of the bed inside the drum. The solid material is normally wetted at or near the inlet of

the drum, usually by spraying moisture onto the bed of tumbling solids. Tumbling drums are fitted with a scraper bar that removes moist material from the drum walls, which would otherwise interfere with the rolling action and decrease the active volume of the drum.

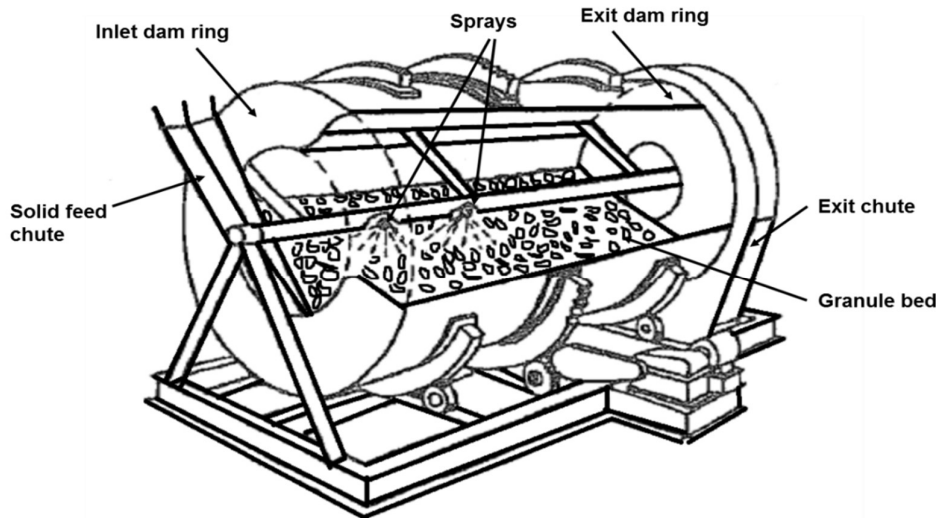


Figure 2.7. Schematic representation of a granulator (Sherrington and Oliver, 1981)

At laboratory and pilot plant scale, small drum granulators can be used for research purposes. The description of a small-scale drum granulator can be found in Chapter 3.

2.5. Permeability of the sinter bed

2.5.1. Introduction

The main goal of granulation is to produce suitable packed beds of granules with high permeability for the sintering process. Packed beds with a higher permeability provide more stable operation and good controllability of the sintering process. Ergun's equation is widely used to compute the pressure drop for flows through packed beds containing packed columns constituted of particles (Ergun, 1952). Equation 2.1 shows Ergun's equation:

$$\frac{\Delta P}{H} = k_1 \frac{\mu v_s (1 - \varepsilon)^2}{(\varphi d_p)^2 \varepsilon^3} + k_2 \frac{\rho v_s^2 (1 - \varepsilon)}{\varphi d_p \varepsilon^3} \quad \text{Eq. 2.1}$$

It can be seen that the pressure drop (ΔP) is not related to a single parameter, but rather a combination of numerous parameters: gas superficial velocity v_s , gas density ρ , gas viscosity μ , granule diameter d_p , shape factor φ , bed voidage ε and bed height H . Under constant experimental conditions, the pressure drop will be only dependent on packed bed properties such as granule size (distribution), voidage and granule shape. The constants k_1 and k_2 are purely empirical by nature. After analysis of numerous experimental data, the best fit of Ergun's equation was obtained with $k_1 = 150$ and $k_2 = 1.75$ (Ergun, 1952; Nemeč and Levec, 2005). These coefficients can vary for every packed bed and should be empirically determined for each case (Jin-Sui and Shang-Xian, 2009; Mitterlehner et al., 2004; Nemeč and Levec, 2005).

In the sintering process, the pressure drop through the sinter bed is often expressed in terms of permeability. This is conveniently used to predict the rate at which the process progresses and the productivity (performance) of the sinter plant. Many researchers reported that the permeability of the sinter bed is dependent on the porosity or voidage of the sinter bed (Ball et al., 1973; Ellis et al., 2007; Khosa and Manuel, 2007; Rankin et al., 1985, 1983; Voice et al., 1953). The higher the voidage, the higher the permeability of the sinter bed. However, there is no mathematical correlation between the bed permeability and voidage that has been established yet. In practice, the permeability of the sinter bed is determined by experimentally measuring the pressure drop of gas flowing across the bed, using Eq. 2.2 (Ball et al., 1973; Voice et al., 1953).

$$\text{Permeability} = \frac{F}{A} \left(\frac{H}{\Delta P} \right)^n \quad \text{Eq. 2.2}$$

where F , A , H and ΔP are flow-rate of gas, cross sectional area of the bed, height of the bed and pressure drop. The exponent n varies from 0.5 to 1. In this equation, the

units of different parameters are arbitrary and the permeability is measured either in British Permeability Units (BPU) or Japanese Permeability Units (Voice et al., 1953).

From experimental data, Voice et al. (1953) proposed that $n=0.6$ is more appropriate for permeability prediction during the pre-ignition stage of the sinter bed. Therefore bed permeability can be rewritten as follows:

$$\text{Permeability} = \frac{F}{A} \left(\frac{H}{\Delta P} \right)^{0.6} \quad \text{Eq. 2.3}$$

where F , A , H and ΔP are expressed in m^3/min , m^2 , mm and $\text{mm H}_2\text{O}$ respectively. In Equation 2.3, the permeability of the sinter is expressed in Japanese Permeability Units (JPU).

2.5.2. Factors affecting the bed permeability

During the permeability test, the structure of the packed bed is strongly influenced by particle properties such as particle size, particle shape and void fraction. Another parameter that characterises the behaviour of granular materials is the friction coefficient or angle of repose.

2.5.2.1. Size of granule

Granule size (distribution) is the most obvious descriptor in the granulation and sintering process. It determines the packing structure of the sinter bed, which in turn influences the bed permeability and airflow rate through the bed. In addition, the granule size distribution can affect the rate of descent of the flame front as well as the sintering reactions that take place in the sinter bed (Ball et al., 1973; Ellis et al., 2007; Ennis and Litster, 1997; Formoso et al., 2003; Khosa and Manuel, 2007; Litster and Waters, 1988; Voice et al., 1953). For instance, if the granules have a wider size distribution range, a closer packed bed will be formed and airflow will be reduced due

to obstruction of local voids by fine granules. Hence, the progress of the whole sintering process will be slow.

The structure of the packing is dependent on the size of particles. Previous studies reported that that fine particles tend to form close packing with low permeability whereas coarse particles likely form loose packing with high permeability (Haughey and Beveridge, 1969; Hausner, 1972; Hinkley et al., 1994a; Pahl, 1975; Rankin et al., 1985; White and Walton, 1937; Wooten, 1998; Yu and Standish, 1993). This justifies the need to increase the mean granule size and tighten the size distribution of granules through granulation prior to the sintering process.

Many researchers explored the possibility of replacing fine iron ore by ultrafine materials (concentrates, dust, iron ore wastes) in sinter making (Bartlett et al., 2009; Borges et al., 2004; Kasai et al., 1989; Pal et al., 2013; Rankin et al., 1985, 1983; Socalici et al., 2011). Unfortunately, a higher amount of ultrafine materials in the feedstock has an adverse influence on the sintering process. Concentrates drastically obstruct the passage of the flame front through the sinter bed, resulting in a lower permeability of the sinter bed and lower productivity of the sinter machine. To mitigate the negative effects of concentrates, these very fine particles can be transformed into micropellets so that they can be used as an alternative feed material in the granulation process (Bartlett et al., 2009; Borges et al., 2004; Pal et al., 2013; Rankin et al., 1985, 1983; Socalici et al., 2011).

Although the granule size plays an important role in determining the behaviour of the granular material (flow, packing and compaction), its definition is not exclusively expressed by one equation. For a large number of randomly orientated particles with different sizes, the particle size of a granular material is often defined in terms of weight – based size fractions obtained by sieving. Some typical definitions of particle size for granular material are given in Table 2.1 (Allen, 1990).

Table 2.1. Typical definitions of particle size (Allen, 1990)

Symbol	Name	Formula and/or definition
d_l	Arithmetic or length mean diameter	averaged diameter based on the number density function of the sample $d_l = \frac{\sum(m_i/d_i^2)}{\sum(m_i/d_i^3)}$ Eq. 2.4
d_s	Surface mean diameter or Sauter mean diameter	diameter of a hypothetical particle having the same averaged surface area as that of the given sample $d_s = \sqrt{\left(\frac{\sum(m_i/d_i)}{\sum(m_i/d_i^3)}\right)}$ Eq. 2.5
d_v	Volume mean diameter	diameter of a hypothetical particle having the same averaged volume as that of the given sample $d_v = \frac{1}{\sqrt[3]{\sum\left(\frac{m_i}{d_i^3}\right)}}$ Eq. 2.6
d_{32}	Sauter Mean diameter (SMD)	diameter of a hypothetical particle having the same averaged specific surface area per unit volume as that of the given sample $d_s = \frac{1}{\sum\left(\frac{m_i}{d_i}\right)}$ Eq. 2.7

* m_i and d_i are respectively mass fraction and diameter of size fraction i .

In granulation, the Sauter mean diameter is commonly used to represent the average size of granules where the active surface area and fluid dynamic aspect are important (Litster et al., 1986; Litster and Waters, 1990). In this research, the SMD is used by default when the mean average size is to be computed.

2.5.2.2. Shape of granules

Granulation of fine iron ore produces granules with irregular shape. This can significantly affect the structure and permeability of the green sinter bed. Hinkley et al. (1994a) predicted the effect of the particle shape on the structure of the packed bed. Rounded particles create less particle-to-particle interlock than angular particles and thus provide easier compaction. Irregular particles often tend to impede compaction resulting in an increase in permeability of the packed bed. Wooten (1998) reported that bed permeability increases the more the shape of particles deviates from the spherical shape.

Pahl (1975) studied the effect of orientation of cylindrical particles with different aspect ratios on the flow through packed beds. Particles packed in different manners. It is evident that irregular particles can orientate themselves at various angles, reducing the reproducibility in pressure drops after repacking the same bed. However the orientation of spheres does not influence the structure of the bed.

The incorporation of concentrates and micropellets into the ore mixture can affect the overall particle shape distribution of granules. Shatokha et al. (2009) reported that granules constituted from high mass percentages of concentrate are much more regular. Their rounded-shapes are quite similar to those of pellets. Their structure consists of a coarse ore particle as core, which is surrounded by adhering fines (concentrates). Shatokha et al. (2009) also found that distinct spherical lumps of fines might be formed in the coalescence process, which form the nuclei of iron ore granules.

2.5.2.3. Void fraction of the bed

The void fraction or porosity in a packed bed is often described as a determinant factor of the pressure drop and permeability. Rankin et al. (1985) reported that the pressure drop across a granulated mix is extremely sensitive to the void fraction of the packed bed. A small decrease in bed void fraction can cause a significant increase in the pressure drop through the packed bed under a given set of conditions. Hinkley et al.

(1994b) found that a variation in void fraction from 0.35 to 0.4 causes approximately a 40% drop in pressure loss across the sinter bed at a given fluid flow rate. Leva and Grummer (1947) also reported that a 1% decrease in the porosity of the bed produced approximately an 8% increase in the pressure drop. For this reason, the granules or particles and the bed as a whole must be resistant to degradation and compaction during the experimental tests, and maintain a constant void fraction.

In the sintering process, the void fraction (voidage) of the packed bed can be used to predict permeability and gas velocity during sintering (Benyahia and O'Neill, 2005; Hinkley et al., 1994a, 1994b; Rankin et al., 1985). The higher the bed void fraction the higher the airflow rate and the higher the permeability of the sinter bed. The velocity of the flame front is also dependent on the void fraction of the sinter bed. Previous studies reported that the void fraction depends on how the bed is packed, which is a function of particle size distribution and particle shape (Benyahia and O'Neill, 2005; Hinkley et al., 1994a, 1994b; Rankin et al., 1985).

In this study, the void fraction throughout the packed bed was considered to remain constant. The measurement of the void fraction through a packed bed of granules was performed by the displacement technique. Here the fluid used was kerosene since the iron ore granules contain moisture (Hinkley et al., 1994b).

2.5.2.4. Angle of repose

The structure of a packed bed is known to be influenced by particle size distribution and particle shape, which in turn influence the permeability and void fraction of the bed. In addition, another parameter that regulates the behaviour of granules is defined as the friction coefficient or angle of repose (Carstensen and Chan, 1976; Debroux and Cleary, 2001; Gallas and Sokolowski, 1993; Mead et al., 2012; Rankin et al., 1983; Rousé et al., 2008; Van Burkalow, 1945; Zhou et al., 1999). Friction prevents sliding. The non-spherical nature of real particles will result in multiple contact points between two contacting particles. Hence, there will be an effective transmission of moment between the particles, and rotations as well as sliding will be limited.

Rousé et al. (2008) found that a decrease in angle of repose is observed for a low deviation from roundness or sphericity. In addition, the angle of repose decreases with increasing particle size (Carstensen and Chan, 1976; Debroux and Cleary, 2001; Gallas and Sokolowski, 1993; Mead et al., 2012; Rankin et al., 1983; Rousé et al., 2008; Van Burkalow, 1945; Zhou et al., 1999). The number of contact points between large particles is small resulting in low friction and small angle of repose. Rankin et al. (1983) reported that liquid bridges between particles in a moist ore mixture can also affect the dynamics of granules. For instance, high moisture content can result in a reduction in friction between granules as well as angle of repose. This confirms the drop of the bed permeability after reaching the maximum value.

The angle of repose was experimentally found to increase with increasing deviation from sphericity, and decreases with increasing particle size (Carstensen and Chan, 1976; Van Burkalow, 1945; Zhou et al., 1999). However, a quantitative description of factors that influence angle of repose, which can be used generally in engineering practice, is not available.

3. Experimental work

The experimental work described in this chapter was carried out at Anglo American Kumba Iron Ore Pilot plant (Pretoria, South Africa), where a bench - scale tumbling drum and permeameter were respectively used to produce granules and measure the green bed permeability. In order to obtain optimum conditions, the moisture content was varied over a range of selected values, and the maximum permeability of the sinter bed was determined.

This experimental work was concerned with the variation of the green bed permeability and some parameters such as granule size distribution, void fraction and angle of repose. Granules were produced from granulation of base mixtures where fine iron ore was partially replaced by concentrate and micropellets. The effect of concentrate and micropellet addition on the green bed permeability was examined. These experiments were necessary to provide experimental data for X-ray microtomographic analysis of the granule shape and DEM – CFD simulations of the pressure drop.

3.1. Experimental

3.1.1. Raw materials

The raw materials used in this study consisted of fine iron ores, concentrate, micropellets, return fines, coke breeze, limestone and dolomite. The three iron ore bearing materials (fine iron ore, concentrate and micropellets) are shown in Figure 3.1. The chemical compositions of fine iron ores and concentrate are listed in Appendix A. Fine iron ores and concentrate are hematite-based materials with 90.80%, 90.30% and 92.60% Fe_2O_3 respectively. The total Fe varies in a narrow range (63.20% - 65.60% Fe_{tot}). The ferrous content between 0.10 and 4.00% can be considered as low if compared to the mass percentages of hematite content. The alkalis content is low. The addition of dolomite and limestone as fluxes provided MgO and CaO that contribute to the formation of slag with a low melting point and with a basicity of about 2 (Cores et al., 2010; Hsieh, 2005).

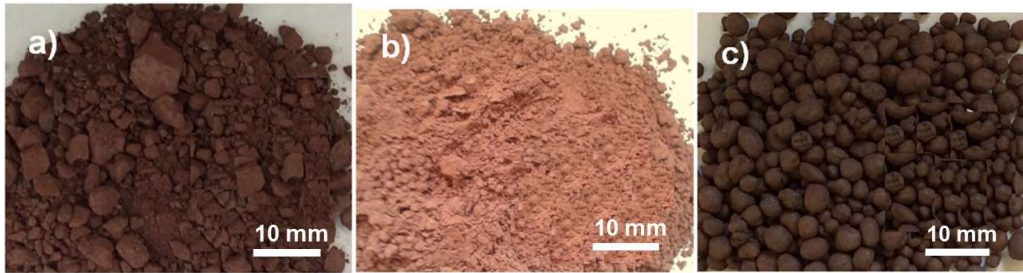


Figure 3.1. Images of raw materials a) fine iron ore (< 10 mm particle size); b) concentrate (< 100 μm particle size); c) micropellets (< 5 mm particle size)

Concentrate was produced through the beneficiation of lower-grade iron ore resources using techniques like crushing, milling and dense media separation to increase the concentration of the iron oxide and remove impurities.

Micropellets were produced by rolling moist concentrate together with 0.5% bentonite and 0.5% polyvinyl acetate as binders, on an inclined disc pelletiser. After sufficient rolling (20–25 min), the micropellets were discharged and subjected to natural drying in order to minimise the costs related to heat hardening. The micropellets had a rounded-shape and their size range was maintained between 1 mm and 4.75 mm. The measured porosity of the micropellets ranged between 60 and 70%. The strength of micropellets dropped from about 37.06 N to 4.34 N after soaking them in water. This can adversely affect the granule properties due to the degradation of micropellets during granulation.

The particle size distributions of different iron ore materials (iron ore, concentrate and micropellets) are given in Figure 3.2. The average particle size of fine iron ore ($d_{50} = 2.9$ mm and 4.2 mm) was bigger than that of concentrate ($d_{50} = 0.12$ mm). The mean particle size of micropellets (d_{50}) was about 3.3 mm. In addition, concentrate and micropellets had narrow size distributions whilst iron ore had a broader size distribution.

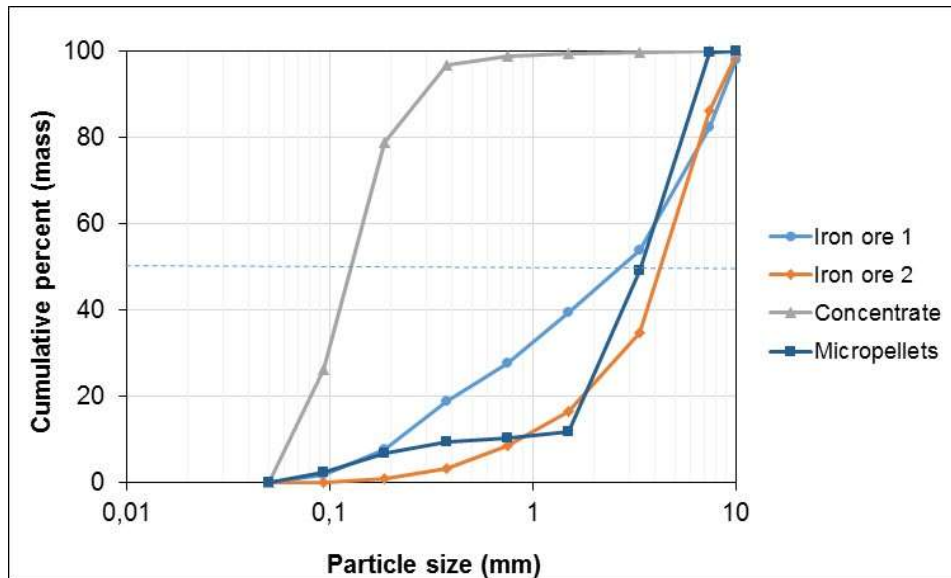


Figure 3.2. Particle size distribution of fine iron ore, concentrate and micropellets

3.1.2. Raw material mixtures before granulation

Sinter feeds were prepared by mixing different raw materials (fine iron ores, concentrate, micropellets, return fines, coke breeze, limestone and dolomite) in specific ratios. Three types of ore mixtures were considered: the conventional mixture (base mixture) and ore mixtures with the addition of 10 – 40% concentrate and micropellets (dry mixture base) respectively. Each ore mixture weighed 30 kg (dry mixture base) and was prepared according to the sinter specifications target of CaO/SiO_2 ratio = 1.95 and 1.81% MgO (Appendix A). Al_2O_3 content between 1.02 and 1.34% was considered as acceptable for the production of the sinter product with good quality (Cores et al., 2010; Hsieh, 2005). The compositions and particle size distributions of the investigated raw material mixtures are given in Table 3.1 and Table 3.2. The addition of concentrate and micropellets influenced the particle size distribution of the ore mixtures. The mass fraction of -0.125 mm (very fine particles) significantly increased from 5.91 up to 22.23% (dry mixture base), as the amount of concentrate increased from 0 to 40% (Table 3.2). Incorporation of concentrate and micropellets in the raw material mixtures decreased the mass fraction of $+4.75$ mm from 9.29 to 6.04% and 9.29 to 6.10% (dry mixture base) respectively.

Table 3.1. Compositions of the raw material mixtures

	Composition (mass %)							
	Iron ore 1	Iron ore 2	Concentrate	Micro pellets	Return fines	Coke	Lime	Dolomite
Base case	27.10	27.10	0.00	0.00	25.00	4.80	10.80	5.20
10%concentrate	24.53	24.53	5.47	0.00	25.00	4.80	10.43	5.23
20%concentrate	21.93	21.93	10.97	0.00	25.00	4.80	10.10	5.27
30%concentrate	19.30	19.30	16.57	0.00	25.00	4.80	9.70	5.33
40%concentrate	16.67	16.67	22.20	0.00	25.00	4.80	9.33	5.33
10%Micropellet	24.57	24.57	0.00	5.47	25.00	4.80	10.37	5.23
20%Micropellet	21.97	21.97	0.00	11.00	25.00	4.80	10.00	5.27
30%Micropellet	19.37	19.37	0.00	16.60	25.00	4.80	9.60	5.27
40%Micropellet	16.70	16.70	0.00	22.27	25.00	4.80	9.20	5.33

Table 3.2. Particle size distributions of the raw material mixtures

	Particle size distribution (mass %)							
	+4.75 mm	+2.00 mm	+1.00 mm	+0.50 mm	+0.25 mm	+0.125 mm	+0.063 mm	Pan
Base case	9.29	40.06	18.56	11.91	7.44	6.84	4.72	1.19
10%concentrate	8.50	37.97	17.64	11.41	7.18	7.40	7.35	2.55
20%concentrate	7.69	35.83	16.73	10.89	6.91	7.97	10.02	3.93
30%concentrate	6.86	33.67	15.81	10.37	6.64	8.56	12.75	5.33
40%concentrate	6.04	31.50	14.89	9.84	6.37	9.16	15.49	6.74
10%Micropellet	8.52	40.45	19.88	11.46	7.10	6.55	4.69	1.39
20%Micropellet	7.72	40.80	21.22	10.98	6.75	6.25	4.68	1.60
30%Micropellet	6.92	41.18	22.59	10.50	6.40	5.97	4.68	1.81
40%Micropellet	6.10	41.53	23.96	10.00	6.03	5.66	4.66	2.02

The changes in compositions of the raw material mixtures were expressed as ratios between two different mass size fractions (Table 3.3). The ratio between -0.25 mm and +1.00 mm size fraction significantly increased with addition of concentrate. The amount of coarse particles decreased, resulting in a potential reduction of granule size after granulation. Micropellet addition to ore mixtures resulted in a noticeable increase in the ratio of (-4.75 mm +1.00 mm) to +4.75 mm size fraction. As small particles have much higher surface area than large particles, micropellets offer more available surface on which the auto layering process can take place.

Table 3.3. Ratios between mass size fractions

	-4.75 mm+1.00mm / +4.75 mm	-0.25 mm / +1.00 mm	-0.25 mm / -4.75 mm +1.00 mm
Base case	6.25	0.19	0.22
10%concentrate	6.67	0.27	0.31
20%concentrate	6.67	0.36	0.42
30%concentrate	7.14	0.47	0.54
40%concentrate	7.69	0.60	0.68
10%Micropellet	7.14	0.18	0.21
20%Micropellet	8.33	0.18	0.20
30%Micropellet	9.09	0.18	0.20
40%Micropellet	11.11	0.17	0.19

3.1.3. Granulation

The main objective of granulation is to improve the permeability of the sinter bed and hence the productivity of the sinter plant. Fine iron ore together with other raw materials were mixed in a laboratory tumbling drum of diameter 0.5 m and length 0.4 m (Figure 3.3). The rotational speed was set at 20 rpm throughout the granulation tests. Water was sprinkled onto the ore mixture in the drum to promote the auto

layering of fines onto coarse particles. After two minutes, the granules were discharged and submitted for permeability, size distribution, void fraction and angle of repose measurements. The granules were produced with 4.50%, 5.00%, 5.50%, 6.00%, and 6.50% moisture contents (dry mixture base) respectively. For ore mixture with 40% of micropellet content, the added moisture was increased up to 7.00%. Micropellets are porous and require more moisture, which is first absorbed into the internal pore spaces, before the granulation effectively starts (Iveson et al., 2004, 2001; Newitt and Conway-Jones, 1958; Rumpf, 1958; Sastry and Fuerstenau, 1973). The moisture content was measured on a dry mass basis.



Figure 3.3. Image showing a bench - scale tumbling drum

3.1.4. Pressure drop measurement

Permeability tests were carried out using a laboratory permeameter (pot). The experiment set-up is schematically shown in Figure 3.4. For each test, iron ore granules were randomly poured into the permeameter (pot) to create a bed, 535 mm in length. A screen with a 1 mm diameter aperture supported the packing. A venturi system was securely sealed to the top of the pot. The bottom of the permeameter was connected to a centrifugal fan using a flexible rubber tube to avoid vibrations. A manual valve was used to control the pressure drop through the packed bed. Air was then

drawn through the packed bed. Pressure was measured in the venturi, above the bed and below the bed using water manometers. Airflow was adjusted to give a pressure drop across the packed bed of 1000 mmH₂O. The pressure in the venturi was then used to calculate the flow rate. The pressure drop across the granule bed was reported in JPU.

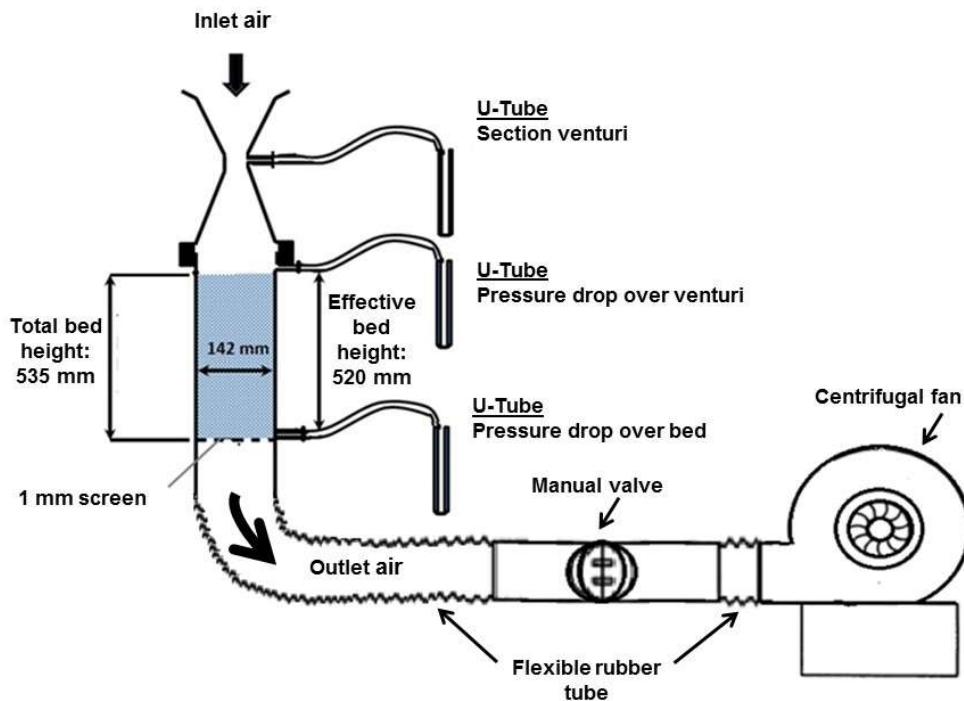


Figure 3.4. Schematic representation of the permeability/pressure drop test

3.1.5. Granule size distribution

Contrary to the technique where wet granules are frozen before screening, 500 g of wet granules were partially dried at 70 °C for 20 minutes. This avoided clustering of the granules due to freezing together. The effect of the partial drying on a potential detachment of small particles from coarse granules whereby particles are poorly attached to each other was not considered in this study. Dried granules were then screened manually, using five sieves with apertures of 4.75, 2, 1, 0.5, and 0.25 mm. The moisture loss during the drying process less than within 2.6% of the wet sample

mass while the mass loss during screening ranged between 3% and 5% (wet mixture base).

3.1.6. Void fraction of the granulated mixture

The granulated mixture consisted of moist and deformable granules that require cautious handling when measuring their void fraction. For each sample, the void fraction for each sample was calculated using Eq. 3.1:

$$\varepsilon = 1 - \frac{\rho_b}{\rho_a} \quad \text{Eq. 3.1}$$

where ε is the void fraction, ρ_b is the bulk density and ρ_a is the apparent density. The bulk density was measured by comparing the masses of the full and empty 1 litre flask.

Water could not be used to determine the apparent density of the granules that contain moisture. This could result in the breaking of the structure of the wet granules. The apparent density was however evaluated using the kerosene volume displacement technique, developed by Hinkley et al. (1994b). For moist granules, the apparent density was calculated according to Eq. 3.2 (Hinkley et al., 1994b).

$$\rho_a = \frac{M_{tot} - M_{ker}}{500ml - V_m} \quad \text{Eq. 3.2}$$

where M_{tot} is the total mass of the flask filled with kerosene and granules, M_{ker} is the mass of the flask filled with 500 ml of kerosene before pouring granules into the flask and V_m is the volume of kerosene required to fill the flask up to the 1 litre mark.

3.1.7. Measurement of the angle of repose

The angle of repose is described as the inclination of the free surface to the horizontal of a bulk pile of solid particles (Figure 3.5). It is a useful tool to characterise the flow behaviour of granular materials. A common test to study the influence of particle friction on the granular material flow is a slump test where material is loosely poured into a tube, which is then lifted to allow the material to flow out under the gravitational forces and form a heap on the horizontal plate. This is primarily used to examine the angle of repose. In this study, a similar method was used to measure the angle of repose for granulated mixtures where three levels of moisture were considered.



Figure 3.5. Angle of repose for granulated mixtures where granules are sticky

3.1.8. Stereo microscopy

Stereo microscopy is a technique that provides relevant information on the morphology of particles. This method is based on two-dimensional microscopic imaging of particles, which generally present themselves with their largest cross-sectional area perpendicular to the light. Granules for this study were analysed using the Olympus SZX7 stereo microscope attached to a CCD (charge-coupled-device) camera.

3.2. Results and discussion

For each sample, the mean granule diameter was calculated from the size distribution of the granulated mix by the relation:

$$d_p = \frac{100}{\sum_i \frac{m_i}{d_{pi}}} \quad \text{Eq. 3.3}$$

where d_{pi} is the mean granule diameter for size fraction i and m_i is the mass percent (wet basis) of granules of size fraction i .

The permeability values for all granulated mixtures are shown in Table 3.4. The corresponding mean granule size and voidage are also listed in Table 3.4. The angle of repose was measured only for three levels of moisture, with emphasis on the optimum moisture content. It can be seen that the permeability of the granulated mix significantly depends on the moisture content. The addition of concentrate and micropellets to mixtures influences the green bed permeability, granule size, voidage as well as the angle of repose.

Table 3.4. Permeability and voidage of granulated mixtures

Sample	Moisture content (%)	Permeability index (JPU)	Mean granule size (Sauter mean diameter) (mm)	Voidage (%)	Angle of repose (°)
Base case	4.5%	20.86	3.32	37.28	53
	5.0%	22.13	3.38	37.55	-
	5.5%*	26.08	3.78	37.65	45
	6.0%	24.13	4.62	37.08	-
	6.5%	20.86	4.96	36.43	38
10% concentrate	4.5%	19.51	3.18	36.24	49
	5.0%	20.86	3.23	36.48	-
	5.5%*	23.32	3.44	36.77	40
	6.0%	23.32	3.59	36.44	-
20% concentrate	4.5%	19.51	4.29	34.56	32
	4.5%	18.07	2.29	35.41	45
	5.0%	19.51	2.81	35.47	-
	5.5%*	23.32	2.75	35.46	42

	6.0%	22.13	3.48	34.81	-
	6.5%	18.07	3.42	34.01	35
30%	4.5%	18.07	2.35	34.46	44
concentrate	5.0%	18.80	2.49	34.69	-
	5.5%*	20.86	2.66	34.33	40
	6.0%	19.51	2.80	34.21	-
	6.5%	18.07	3.32	32.42	34
40%	4.5%	14.75	2.31	33.35	42
concentrate	5.0%	19.51	2.48	33.80	-
	5.5%*	19.51	2.48	33.75	38
	6.0%	17.30	2.53	32.81	-
	6.5%	16.49	3.17	31.10	29
10%	4.5%	19.51	2.41	36.01	42
micropellets	5.0%	21.50	2.51	36.41	-
	5.5%*	23.32	2.61	36.58	39
	6.0%	23.32	3.12	36.58	-
	6.5%	20.86	3.18	35.87	32
20%	4.5%	19.51	2.33	35.67	42
micropellets	5.0%	20.86	2.41	36.23	-
	5.5%	22.13	2.47	36.45	-
	6.0%*	23.32	2.41	36.97	40
	6.5%	19.51	2.82	36.27	35
30%	4.5%	16.49	2.30	34.72	45
micropellets	5.0%	19.51	2.36	35.68	-
	5.5%	22.13	2.18	36.26	-
	6.0%*	23.90	2.51	36.68	39
	6.5%	19.51	3.67	35.56	34
40%	4.5%	14.75	2.27	35.27	40
micropellets	5.0%	16.49	2.27	35.54	-
	5.5%	19.51	2.46	36.56	36
	6.0%	22.13	3.12	36.75	-
	6.5%*	23.32	3.13	36.82	32
	7.0%	16.49	3.44	34.72	5

* optimum moisture corresponding to maximum permeability of the granule bed

Granules containing concentrate and micropellets respectively were subjected to optical microscopy imaging. To obtain a comparison between granule structures, three granule samples consisting of the base mixture, 20% concentrates and 20% micropellets were analysed. These granules were selected from the granulated mixtures obtained at optimum moisture (5.5% moisture – dry mixture base) (Table 3.4). Images of the granules were taken using a stereo microscope as shown in Figure 3.6. Three arrows were drawn to indicate granules with similar structures (finer material onto coarse particles – pellet-like structure – finer material around micropellets). The overall shape of the granules in the base mixture sample is very angular, and this may give the sample a high permeability value. Angular particles are characterised by more particle-to-particle friction than spherical granules and might generate packed beds with high voidages (Gallas and Sokolowski, 1993; Hinkley et al., 1994b). For the ore mixtures containing concentrate and micropellets, the granules are spherical. The corresponding green beds are expected to present lower interactions between particles as well as lower voidage (Gallas and Sokolowski, 1993; Hinkley et al., 1994b).

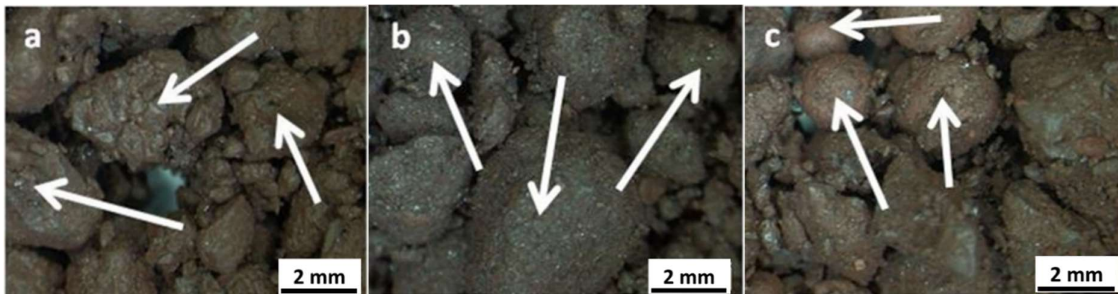


Figure 3.6. Stereo microscopic images of produced granules (5.5% moisture content): a) base case; b) with concentrate addition; c) with micropellet addition

3.2.1. Permeability – moisture correlations

For each sample, the permeability was plotted against the moisture content (Figure 3.7). Permeability–moisture curves are parabolically shaped, passing through a maximum at the point where the moisture content is considered as optimum. The permeability of the sinter bed first increased as the moisture content increased. This is due to increasing adherence of fines onto coarse particles, which is accompanied

by an increase in granule diameter. The maximum permeability is reached before high moisture contents that cause flooding, deformation and collapse of the granule coating with a subsequent loss in permeability. As the moisture content increased, a point was therefore reached where too high moisture contents resulted in weak granules and lower permeability (Figure 3.7). According to Rankin et al. (1983), the friction between the granules is reduced at higher moisture contents, which may cause the green granules to slump and form a compactly packed bed.

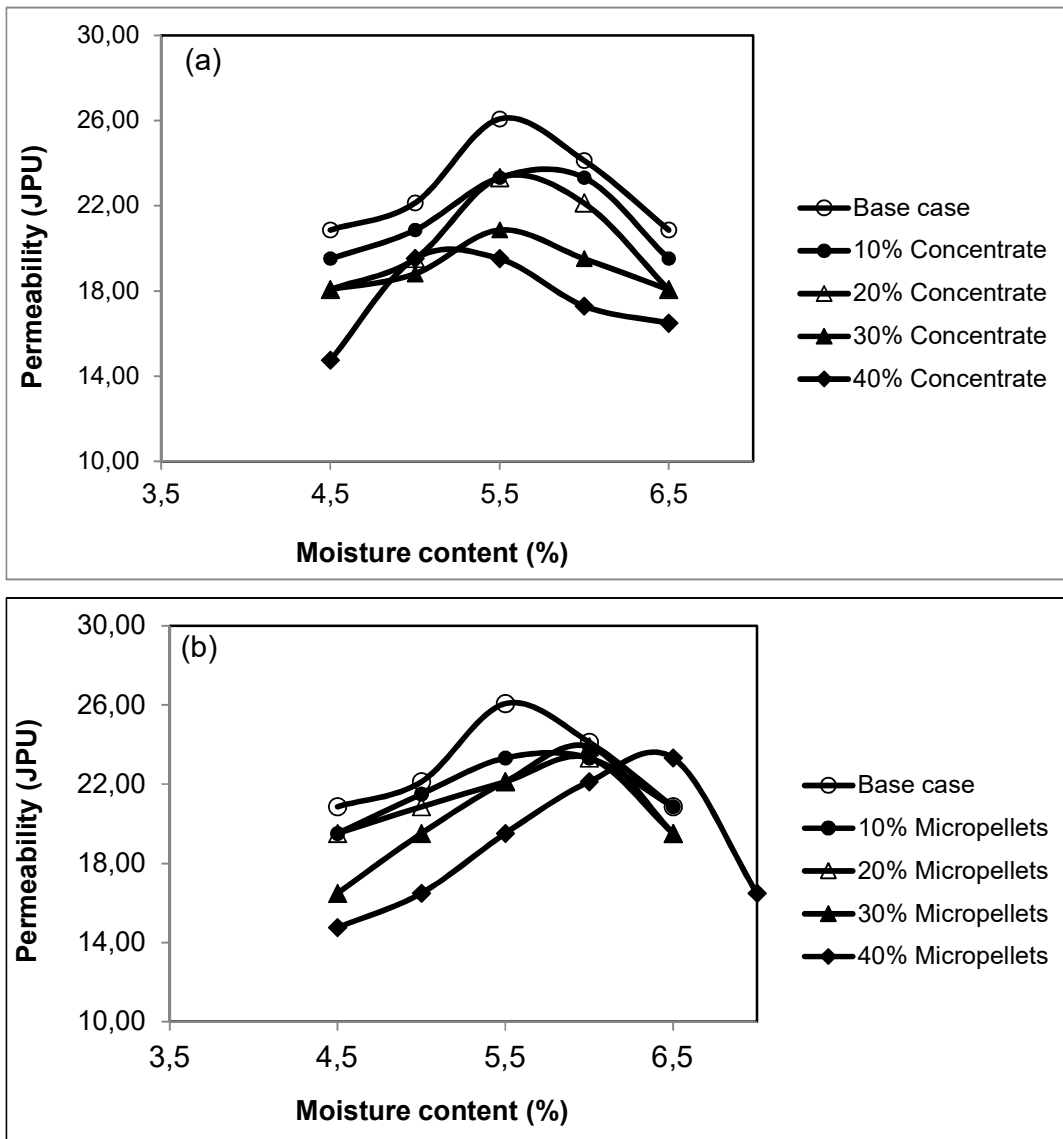


Figure 3.7. Effect of (a) concentrate and (b) micropellet addition on green bed permeability

In the iron sinter plant, the maximum permeability is an important parameter, which affects the productivity of the sintering process (Ellis et al., 2007; Formoso et al., 2003; Kapur et al., 1993; Khosa and Manuel, 2007; Litster and Waters, 1988; Loo et al., 1992; Venkataramana et al., 1999; Waters et al., 1989). The variation of the permeability of the sinter bed with addition of concentrate and micropellets was therefore examined by considering the results obtained at optimum moisture content (Figure 3.8). It can be seen that the green bed permeability decreases as the mass fraction of concentrate and micropellets increases (3.2.2 and 3.2.3).

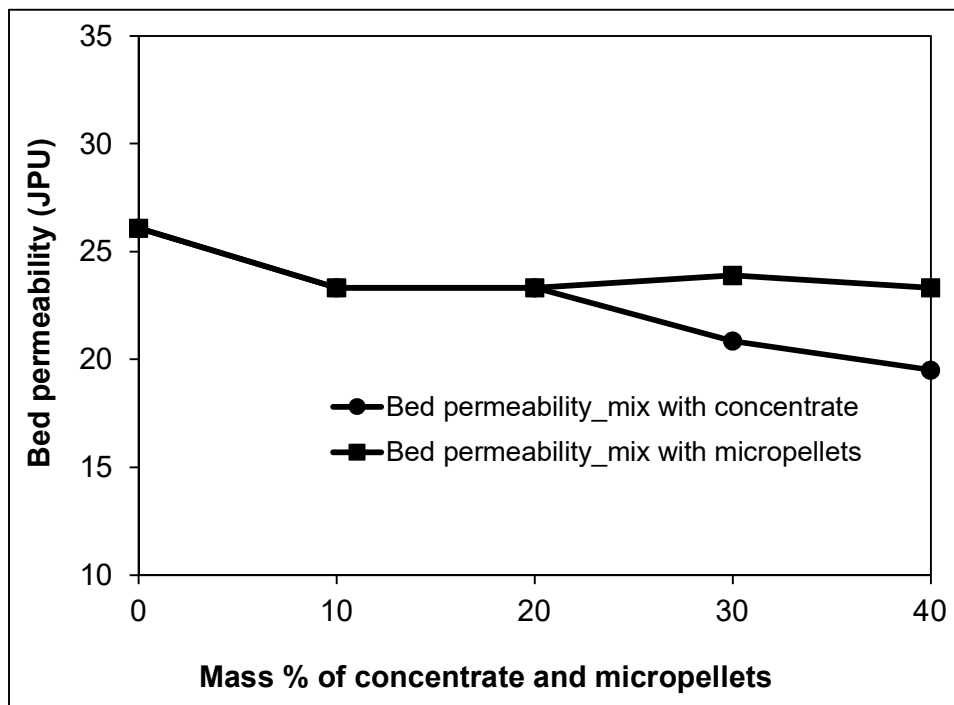


Figure 3.8. Variation of the maximum permeability with concentrate and micropellet addition

3.2.2. Effect of concentrate addition on green bed permeability

The addition of concentrate to the ore mixture resulted in a decrease in the maximum permeability as the mass percentage of concentrate increased (Figure 3.8). The presence of concentrate in the mixture resulted in a complex granulation mechanism. The adhering fines participated in the formation of microgranules as well as the layering of coarse particles. For mixtures with 10 and 20% concentrate, less adhering fines were available to promote the coating of coarse particles, which can act as nuclei.

This deficiency brought about the production of granules with low mean granule size, resulting in lower permeability of the sinter bed. In mixtures with 30 and 40%, adhering fines was sufficient to produce granules with thick adhering layer but in small number due to a decrease in coarse particles (Table 3.2 and Table 3.3). This resulted in a significant decrease in the bed permeability of granules with 30% and 40% concentrate due to their potential deformation (Hinkley et al., 1994a, 1994b). Additionally the formation of microgranules and reduction of larger nuclei particles (+2.00 mm size fraction) may contribute to the production of granules with smaller average diameter for mixtures with 30% and 40% concentrate.

Shatokha et al. (2009) reported similar results, where the granule size is affected by the concentrate-iron ore ratios. For low ratio (less than 0.5), the amount of fines available in the layering process was not enough to adhere onto coarse particles. The granules produced were smaller. However an increase in concentrate fraction (more than 0.5) resulted in the formation of granules with thick layers of adhering fines.

Incorporating concentrate in the mixture resulted in the formation of more spherical granules. The particle-to-particle interlocking is less for spherical particles, which form compact packed beds (Hinkley et al., 1994b; Rankin et al., 1983; Rankin and Roller, 1985).

3.2.3. Effect of micropellet addition on green bed permeability

Replacement of fine iron ore by micropellets resulted in a decrease in the mass percentage of adhering fines. The very fine fraction was not enough to promote the adhering of fines onto coarse particles. The granules that were formed in such a system were more spherical but had small diameters. These features caused the maximum permeability of the granule bed to be lower than that of the base case (Figure 3.8).

As the mass percentage of micropellets in the mix increased, an increased amount of moisture was required to reach maximum permeability. This was due to pores in the micropellets that were first filled with moisture before the granulation process started. For a mix with 40% micropellets, the maximum permeability was reached at 6.5% moisture content. This confirmed that when using porous micropellets in a mixture, more moisture was required to improve the permeability of the sinter bed.

3.2.4. Factors affecting the green bed permeability

The permeability of the green granule bed is sensitive to changes in parameters such as moisture content and ore characteristics through their impact on size, strength, morphology and flow characteristics of granules (Carstensen and Chan, 1976; Debroux and Cleary, 2001; Ergun, 1952; Gallas and Sokolowski, 1993; Hinkley et al., 1994b; Mead et al., 2012; Rankin et al., 1983; Rankin and Roller, 1985; Van Burkalow, 1945; Zhou et al., 1999). In this section, the focus is on the effects of concentrate and micropellet addition on the granule size, voidage and angle of repose of sinter beds. The variation of these parameters was examined at the corresponding optimum moisture contents.

3.2.4.1. Mean granule size

The variation of mean granule size with addition of concentrate and micropellets is shown in Figure 3.9. The granules in the base mixture were bigger than those with addition of concentrate and micropellets. For mixtures with concentrate addition, very fine particles produced microgranules by binding particles of intermediate size. This mechanism deviated from adherence of fines onto coarse particles towards a more complex mechanism (Shatokha et al., 2009). The sharing of finer material between autolayering and coalescence mechanisms caused the growth of granules to be limited. The addition of concentrate decreased the mass percentages of large nuclei particles (> 2 mm size fraction) (Table 3.2 and Table 3.3). It is evident that a limited granule growth and decrease in coarse nuclei fraction may contribute to a decrease in average granule size as the mass percentage of concentrate increases.

The incorporation of micropellets in the ore mixture increased the mass percentage of small nuclei particles (-4.75 mm +1.00 mm) while the mass percentage of +4.75 mm size fraction (large nuclei) decreased. (Table 3.2 and Table 3.3). More granules with small nuclei as core were then formed, resulting in a reduction of the mean granule size. Additionally the decrease in the mass percentage of fines contributed to a limited granule growth and thus a decrease in granule size. For the mixture containing 40% micropellets, the granule size showed a slight increase due to the adherence of small granules onto large ones as described by Kapur et al. (1993) and Venkataramana et al. (1999). Micropellets investigated in this study behaved as intermediate particles and started to adhere onto large granules. This process produced large granules.

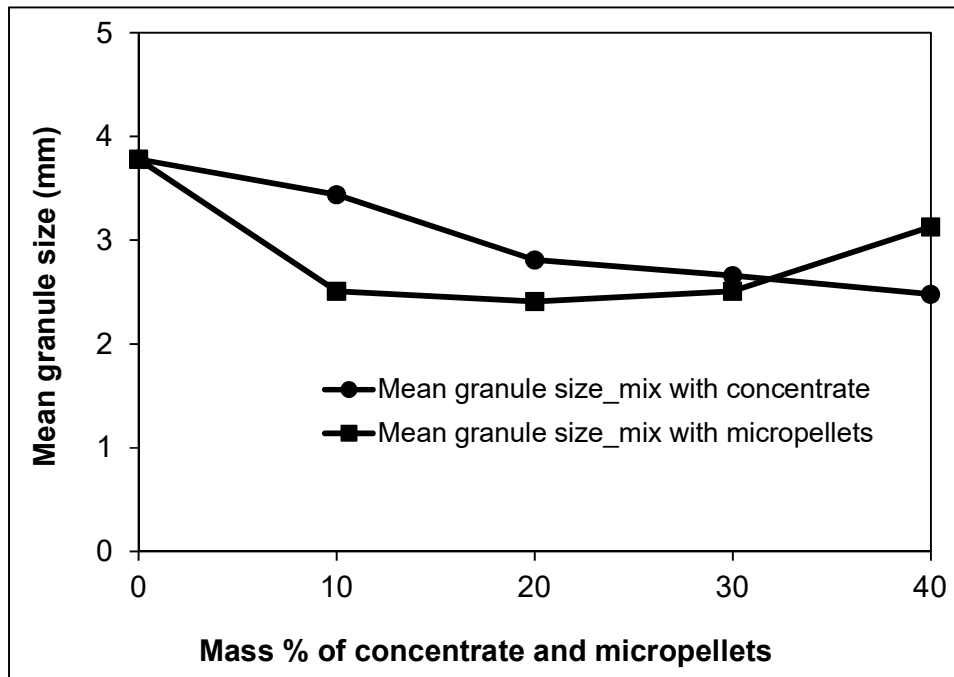


Figure 3.9. Variation of mean granule size with concentrate and micropellet addition at optimum moisture content

3.2.4.2. Voidage

The voidage of the granulated mix was measured using the kerosene displacement technique. For each sinter bed, the voidage increased and passed through a maximum as the moisture content increased (Table 3.4). At low moisture content (4.5–5.5%), an

increase in granule size was associated with an increase in the bed voidage. This led to an improvement of the bed permeability. Further addition of moisture produces deformable granules, which caused the bed voidage and permeability to decrease significantly (Ellis et al., 2007; Hinkley et al., 1994b; Rankin et al., 1983; Rankin and Roller, 1985).

The effect of the addition of concentrate and micropellets on the voidage of granulated iron ore was examined at optimum moisture content (Figure 3.10). The addition of concentrate to mixtures decreased the voidage of the corresponding green beds. This effect can be explained by the formation of granules that may deform during their packing (Hinkley et al., 1994a, 1994b). For sinter beds containing micropellets, the change in the voidage was not significant although the resulting granules were smaller. Micropellets formed strong granules that resist deformation when poured into a permeameter. It can be also seen that a decrease in the bed voidage resulted in a decrease in the permeability of the green bed. A decrease in voidage contributed to more resistance to airflow through the bed. Smaller granule sizes also produced beds that were more compactly packed, resulting in a decrease in permeability.

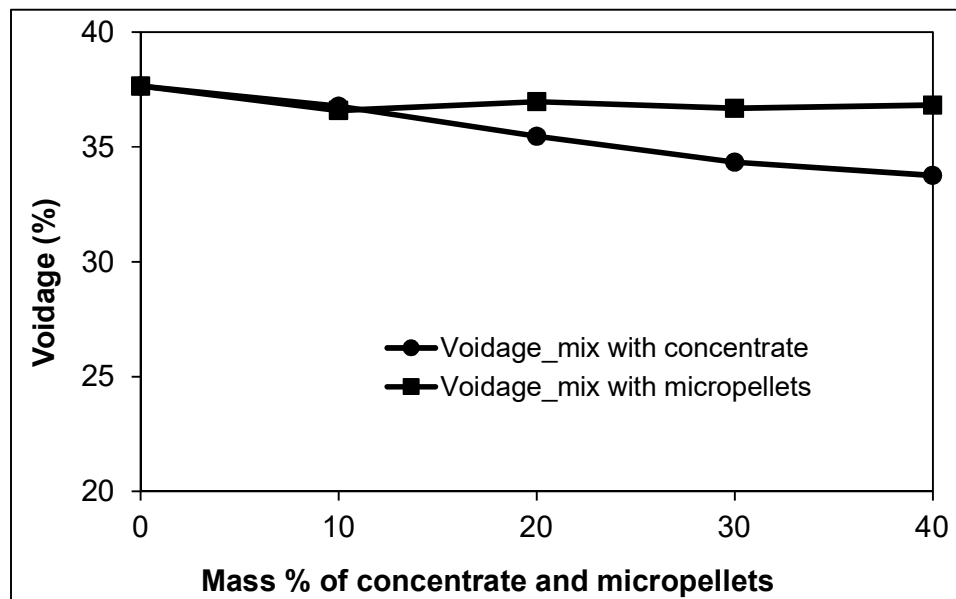


Figure 3.10. Variation of voidage with concentrate and micropellet addition

3.2.4.3. Angle of repose

Three levels of moisture content were considered when the variation of angle of repose of the sinter beds with addition of concentrate and micropellets was evaluated (Table 3.4). Clearly, the angle of repose depended on the moisture content. Increasing the moisture content in different mixtures decreased the angle of repose. This information is important to understand the behaviour of iron ore granules during packing. Contrary to fine powders where the angle of repose increased with addition of moisture, the angle of repose for iron ore granules decreases with moisture content. The interaction forces, which bind fine particles, did not play a dominant role with increasing the size of the granules.

The addition of concentrate and micropellets to the ore mixtures obtained at optimum moisture decreases the angle of repose (Figure 3.11). The resulting granules were more spherical compared to those of the base case sinter as shown in Figure 3.6. Spherical particles easily flow and have low angles of repose. This is in agreement with previous researchers who reported an increase in the angle of repose as the particle shape deviates from spherical (Carstensen and Chan, 1976; Debroux and Cleary, 2001; Gallas and Sokolowski, 1993; Mead et al., 2012). Incorporating micropellets into the mixtures produced sinter beds with lower angles of repose. The resulting granules were strong and could easily flow compared to the deformable granules produced from the mixtures which contained concentrate.

The angle of repose expresses the friction between particles, which prevents sliding. Less spherical granules (produced from base mixture) have multiple contacts between two contacting granules. This leads to an effective transmission of moment between different particles, resulting in limited rotation and sliding. The addition of concentrate and micropellets to the base mixture, however, resulted in the formation of more spherical granules, with low angles of repose and therefore less friction between the granules.

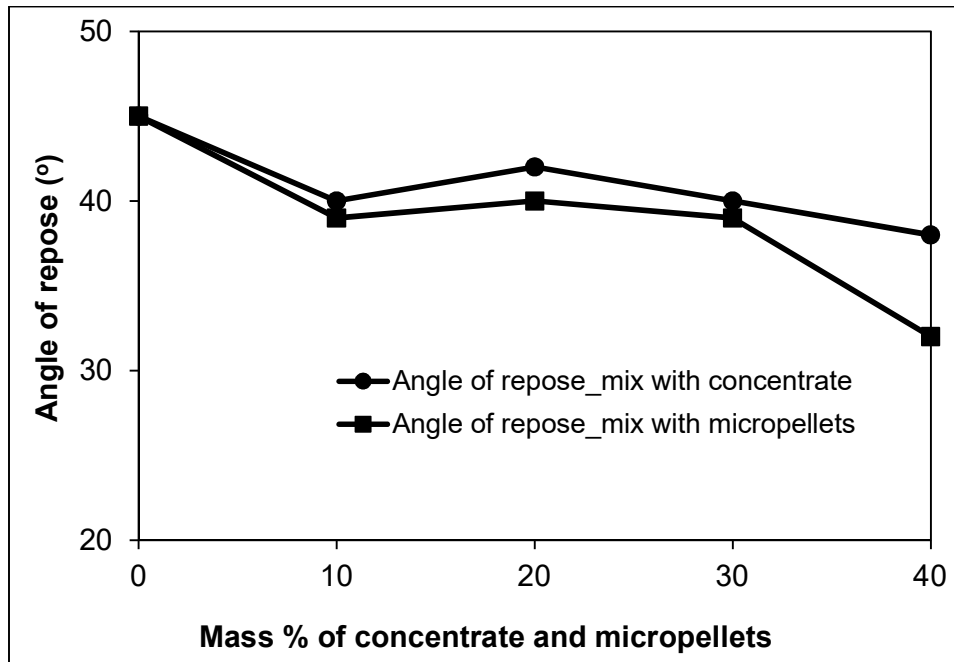


Figure 3.11. Variation of angle of repose with (a) concentrate and (b) micropellet addition

3.3. Conclusions

The experimental investigation on how concentrate and micropellet additions to the sinter feed affect green bed permeability led to the following conclusions:

- Addition of concentrate and micropellets to the raw material mix decreases the permeability of the sinter bed. High amounts of concentrate (30% and 40%) in the ore mixture result in a substantial decrease in the maximum bed permeability compared to micropellet addition. More deformable granules were formed. The maximum permeability of granulated mixtures that contain concentrate is approximately reached at a constant moisture. For mixtures containing micropellets which are porous, additional water is required to obtain maximum permeability.
- Based on optimal moisture content, no single parameter could fully explain the variation of the green bed permeability with addition of concentrate and micropellets. The granule size, voidage and angle of repose were individually

considered in an attempt to explain the effect of concentrate and micropellet addition on the permeability of the sinter bed.

- Ore mixtures containing concentrate and micropellets produced granules with small mean size due to a limited growth and sharing of adhering fines between different granulation mechanisms. A decrease in mass percentages of coarse nuclei particles (as core) contributed to a decrease in average granule size. The variation of voidage is significant for mixtures that contain concentrate, as the resulting granules can easily deform and form compact sinter beds with lower voidage (mixtures with 30% and 40% concentrate). Incorporating concentrate and micropellets in the ore mixture decreases the angle of repose. The granules become more spherical and form sinter beds with lower angles of repose.

4. Study of structure and shape of granules produced during granulation of mixtures with addition of concentrate and micropellets

4.1. Introduction

The structure and shape of granules have been considered important parameters that can be used to explain the mechanism of the granulation process (Kapur et al., 1993; Litster et al., 1986; Venkataramana et al., 1999) and predict the green bed permeability (Hinkley et al., 1994a; Mora and Kwan, 2000; Rousé et al., 2008; Santamarina and Cho, 2004; Shinohara et al., 2000; Witt and Brauns, 1983; Wooten, 1998). The analysis of the shape and structure of irregular granules is still a challenge in the engineering field. Optical and scanning electron microscopy is commonly used to investigate the internal structure and the morphology of granules. However, the data obtained are two-dimensional and the thickness of the particle is often ignored, hereby compromising the accuracy by which the shape factor of the real-world particles is determined. The problem is pronounced when investigating wet and deformable granules, which must be mounted and polished to reveal their structure.

In this study, X-ray microtomography was used to analyse the granule structure and shape. From 3D images obtained by X-ray microtomography, the effect of concentrate and micropellet addition on the geometrical structure and shape of the granules could be studied.

The analysis of the shape and structure of irregular granules has attracted a significant amount of attention from many researchers. Garboczi (2002) used X-ray microtomography to study the morphological aspects of aggregates, which completely characterize concrete aggregate particles. Fu (2005) extensively studied the behaviour of granular material with irregular particle configurations using X-ray microtomography. Using the data, it was possible to simulate particle kinematics, stress distributions and strain distributions of granular materials. Bhuiyan (2011) used

X-ray microtomography to characterise the morphology of green iron ore pellets and then perform a quantitative image analysis of the cavities that were caused by the entrapped air bubbles in iron ore green pellets. Shatokha et al. (2009) described two mechanisms of iron ore granulation (coalescence and autolayering) based on the 2D X-ray microtomographic images of granules containing concentrate. Erdoğ an and Fowler (2005) extensively used X-ray microtomography to capture the true shape of particles of concrete aggregates. They found that the shapes of aggregate particles influence the rheological properties of concrete mixtures.

4.2. X-ray microtomography

X-ray microtomography is a relatively new technique applied in granulation and sintering processes. The main goal of the technique is to reveal internal features and obtain 3-D geometries of granules without destroying them. This technique is derived from the greek word “*tomos*” (meaning sections) and consists of digitally slicing a sample using X-rays, and whereby the internal structure can be visualized (Ketcham and Carlson, 2001; Maire et al., 2001).

The basic principle of X-ray microtomography is similar to the medical computed tomography scan and based on Beer – Lambert law (Ketcham and Carlson, 2001). Attenuation of X-rays penetrating through a sample depends on the thickness and density of the sample. For instance pores in the sample appear as regions with a very low attenuation coefficient. X-ray attenuation is dependent on the energy of the incoming X-rays and the density and atomic number of the material the rays pass through. When X-rays pass through a homogenous sample of thickness T , the transmitted intensity I of the radiation beam can be expressed as:

$$I = I_0 e^{-\mu_p(\rho, Z, E_0)T} \quad \text{Eq. 4.1}$$

where I_0 and E_0 are the intensity and energy of the incident beam while μ_p is the linear attenuation coefficient of the photons. The properties of the material are represented by the density (ρ) and atomic number (Z).

For a non homogeneous sample, the intensity between successive blocks of different materials in the sample can be expressed using Eq. 4.2:

$$I = I_0 e^{-\int \mu_p(\rho, Z, E_0) dT} \quad \text{Eq. 4.2}$$

X-ray microtomography has a high penetration ability (~5–20 mm) and provides a reasonable level of resolution (~ 3 - 5 μm voxel size). The reconstruction of the final image is done by a 3D map of the local X-ray attenuation coefficient through the sample by applying the Beer–Lambert law using a filtered back projection algorithm.

4.3. Analysis of three-dimensional particle shape

Packing behavior of a granular system is highly affected by the arrangement of the particles which in turn is determined by the level of the irregularity of the particles. The particle shape is considered an important parameter to describe irregular or non-spherical particles. Despite the importance of the particle shape, the determination of the shape parameters of non-spherical particles remains a challenge.

In this section, different ways to describe the shape of irregular particles are discussed. A common way of characterising the particle shape is based on three scale measurements (Barksdale et al., 1991; Barrett, 1980; Blott and Pye, 2008; Garboczi, 2002; Krumbein, 1941; Powers, 1953; Wadell, 1934, 1933, 1932; Zingg, 1935). The macro scale measurement is defined as sphericity, which refers to the overall particle form and how the particle approaches a spherical shape. The micro scale measurement, roundness, represents the curvature of corners of the particle. The surface texture is the smallest scale but it can strongly affect the shape of the granule. The surface area of the granule tends to increase with an increase in irregularity of granules of the same volume. In practice, each parameter can affect the behaviour of the granulated material to such an extent that it is difficult to isolate the effects of one

from the other. A schematic diagram illustrating the three aggregate shape properties is shown in Figure 4.1 (Barrett, 1980).

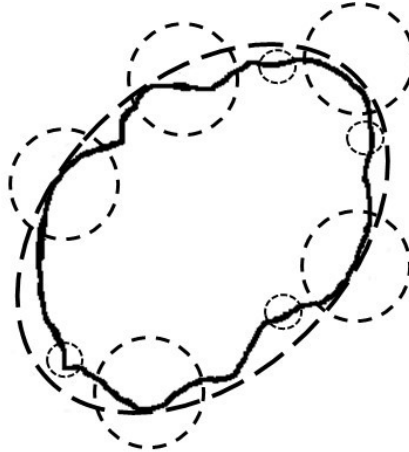


Figure 4.1. Shape description of aggregate: form (dashed ellipse), roundness (dashed circle), and texture (short dashed circles) (Barrett, 1980)

Most researchers agree that sphericity is the major parameter that characterises the shape of a granule on a large scale (Barksdale et al., 1991; Barrett, 1980; Blott and Pye, 2008; Garboczi, 2002; Krumbein, 1941; Krumbein and Sloss, 1963; Powers, 1953; Wadell, 1934, 1933, 1932; Zingg, 1935). The analysis of roundness is more subjective, resulting in inherent errors during image analysis. For instance, Krumbein (1941) established a chart where the roundness can be estimated by just visual observations (Figure 4.2). This method can quantify the roundness from 0.1 to 0.9 by comparing the examined shapes to the predefined ones. Furthermore, Powers (1953) proposed a chart based on a qualitative classification that includes the sphericity and roundness, as shown in Figure 4.3. This classification was able to relate six roundness series (very angular, angular, sub-angular, sub-rounded, rounded and well rounded) with two sphericity ranges (high and low sphericity).

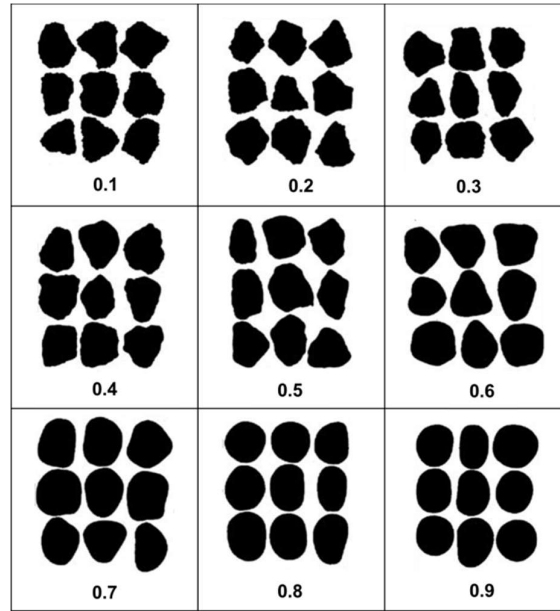


Figure 4.2. Chart for visual evaluation of roundness (Krumbein, 1941)

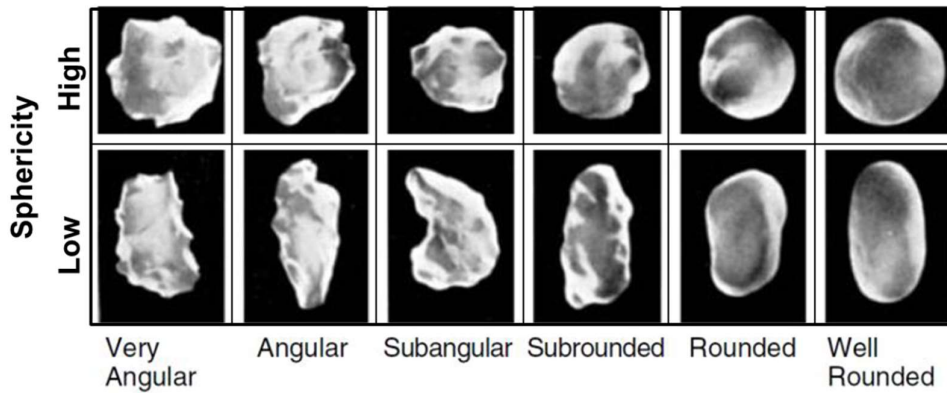


Figure 4.3. Granule shape based upon morphological observations (Powers, 1953)

Although visual observations are often useful to define the granule shape, quantitative measurements are recommended in order to reduce the errors due to subjectivity. Previous authors have shown that granule shape can be defined by mathematical relations in which different geometrical characteristics of a granule can be included (Blott and Pye, 2008; Corey, 1949; Janke, 1966; Krumbein, 1941; Wadell, 1934, 1933, 1932). In this study, the shape description focussed more on the sphericity of the granule than its roundness or texture.

There are numerous approaches for characterisation of the shape of non-spherical particles. Wadell (1932) reported that the sphericity of a granule can be described by the ratio of the surface of a sphere having the same volume as the particle to the actual surface area of the particle. Due to the difficulty to measure the surface area of irregular solids, Wadell (1933) proposed an operational sphericity which is described as the ratio between the diameter of a sphere having the same volume and the diameter of the smallest sphere that circumscribes the particle. Other shape factors that describe the morphology of a particle were defined on the basis of measurements of the three axes (width, thickness and length) of the particle (Corey, 1949; Janke, 1966; Krumbein, 1941). The terms width, thickness and length refer to the dimensions of a rectangular cuboid that circumscribe the particle (Figure 4.4). To avoid inherent errors in sphericity calculation, this cuboid is assumed to be of minimum volume. Krumbein (1941), Corey (1949) and Janke (1966) respectively quantified the sphericity and shape factor of a particle by establishing the expressions given in Table 4.1.

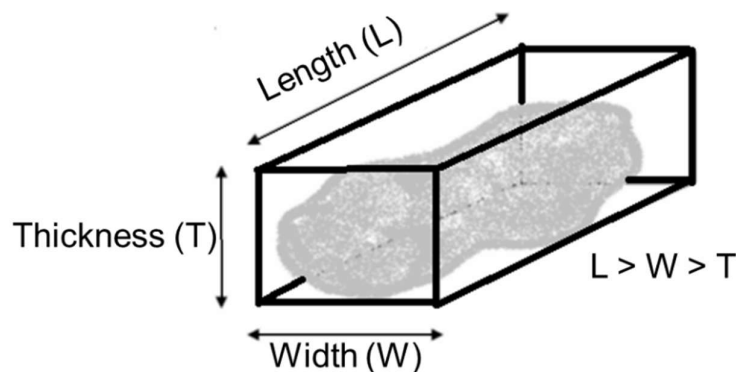


Figure 4.4. The principal dimensions of an aggregate particle (Erdoğan, 2003)

Table 4.1. Correlation of Shape factor of 3D particle shape (Corey, 1949; Janke, 1966; Krumbein, 1941; Wadell, 1933, 1932)

Models	Equations	Parameters
Wadell (1932)	$\varphi = \frac{s}{S}$	φ is the true sphericity, s is the surface of a sphere of the same volume as particle and S is the particle surface.
Wadell (1933)	$\varphi = \frac{d_{sv}}{d_{cir}}$	φ is defined as the operational sphericity, d_{sv} is the diameter of a sphere of the same volume as particle and d_{cir} is the diameter of the circumscribed sphere.
Krumbein (1941)	$\varphi = \sqrt[3]{\frac{WT}{L^2}}$	φ is sphericity, L is the length, W is the width and T is the thickness
Corey (1949)	$\varphi = \frac{T}{\sqrt{LW}}$	φ is the shape factor.
Janke (1966)	$\varphi = \frac{T}{\sqrt{\frac{L^2 + W^2 + T^2}{3}}}$	φ is the Janke form factor.

Zingg (1935) classified different particle shapes into four base classes as mentioned in Table 4.2 and Figure 4.5a. A disc and blade are described by two long axes and one short one. The ratio of width to length is smaller than 2/3 for a blade and bigger than 2/3 for a disc. A roller has two short axis and one long one. Its ratio of width to length is smaller than 2/3. For a spherical particle, the three axes are almost equal and the ratios of width to length and thickness to width are bigger than 2/3. Krumbein and Sloss (1963) plotted the iso-sphericity curves in the Zingg's diagram (Figure 4.5b). The combination of these two diagrams can simultaneously classify the shape of a particle and quantify its sphericity.

Table 4.2. Classification based on ratios W/L and T/W (Zingg, 1935)

Class	W/L	T/W	Shape
I	$> 2/3$	$< 2/3$	Disc
II	$> 2/3$	$> 2/3$	spherical
III	$< 2/3$	$> 2/3$	Roller
IV	$< 2/3$	$< 2/3$	Blade

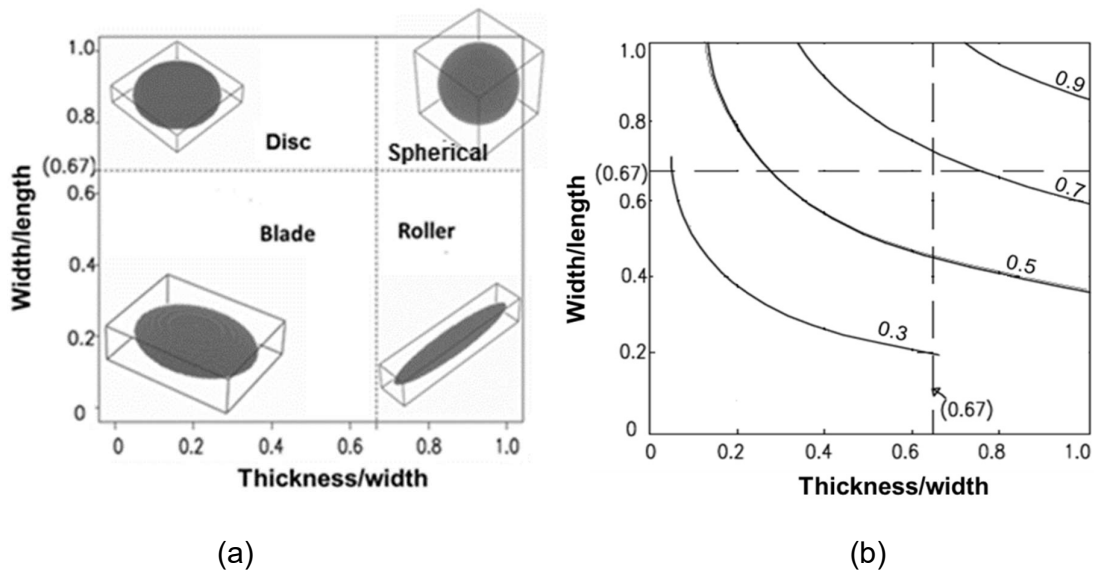


Figure 4.5. Description (a) particle forms using the Zingg diagram (Zingg, 1935) and (b) iso- sphericity curves defined by Krumbein and Sloss (1963)

4.4. Experimental

4.4.1. Iron ore granules

The production of iron ore granules was carried out in a bench - scale tumbling drum (Figure 3.3). Ore mixtures were prepared by mixing different raw materials in specific fractions (Table 3.1 and Table 3.2). Three types of ore mixtures were considered: a base mixture (no addition of concentrate and micropellets), ore mixtures with the addition of 10 – 40% concentrate and ore mixtures with the addition of 10 – 40%

micropellets. From each mixture sample, granules of +1 mm size fraction were randomly picked for X-ray microtomography analysis.

4.4.2. X-ray microtomography analysis of granules

The measurement of the granule shape was determined by X-ray microtomography analysis at the MIXRAD facility at the Nuclear Energy Cooperation of South African (NECSA). The instrument used was a Nikon XTH/225-ST Microfocus X-Ray Microtomography system (Figure 4.6). All the scans were performed at 150 kV and 80 μ A using a 1.0 mm copper pre-filter to reduce the effect of beam hardening or low-energy rays. Data were acquired from 1000 projections within 360 degrees. The acquisition time was approximately 1 hour. Only granules obtained at optimum moisture were analysed. Representative samples were obtained by coning and quartering granules from the +1mm size fraction until a small enough sample size was obtained. The sample size was limited to about 12 – 18 granules due to the restricted exposure space available on the rotary stage. Granules from +1 mm fraction size were selected because of the substantial thickness of the adhering layer.



Figure 4.6. Nikon XTH/225-ST Microfocus X-ray microtomography system

Samples were then scanned using a radiation beam of X-rays and the intensity of the transmitted X-rays were measured using a CCD (charge-coupled-device) detector as shown in Figure 4.7. A scintillator screen is used to convert the pattern of X-ray intensity transmitted by the sample to a visible light image, which is magnified onto the surface of the CCD detector. By rotating the sample, sufficient data were obtained and the two-dimensional images were stacked together to generate a complete three-dimensional map. The CCD detector could provide a resolution of up to 3 microns. Images were processed using VG-StudioMax 2.2 software to obtain dimensional information about the sample such as volume, surface and linear dimensions of granules. 2-D slice images were used to investigate the internal structure of the granules.

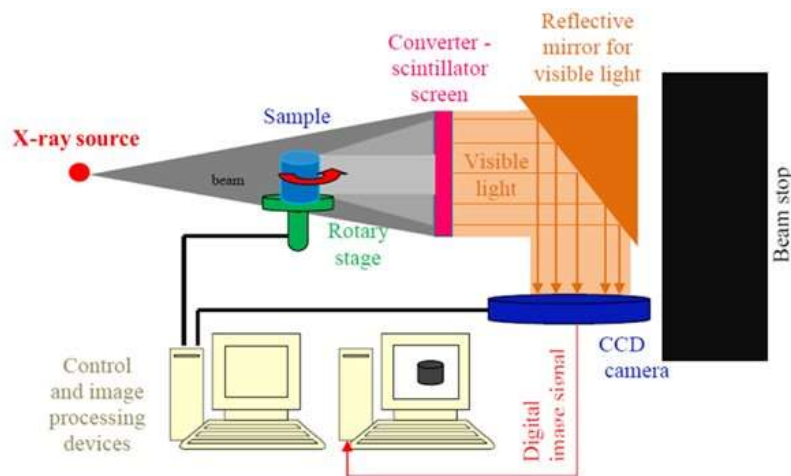


Figure 4.7. Schematic experimental setup of the X-ray microtomography (De Beer, 2005)

4.5. Results and discussion

4.5.1. Structures of granules

The structures of the granules were investigated as 2-D images to reveal the internal structures as well as the mechanism of granulation. Different types of structures could be identified in the analysed granules (Figure 4.8). Finer particles appeared as blurry regions due to the limited resolution (3 – 5 microns) and were difficult to distinguish,

while medium and large particles in the granules were big enough to be detected and had a wide range of shapes. Most granules from the base case sample consisted of a core (nuclei particles) surrounded by a layer of fines, whereas the addition of concentrate and micropellets resulted in complex structures. To easily differentiate between different structures, the granules were classified into four groups (Gr. I, II, III and IV).

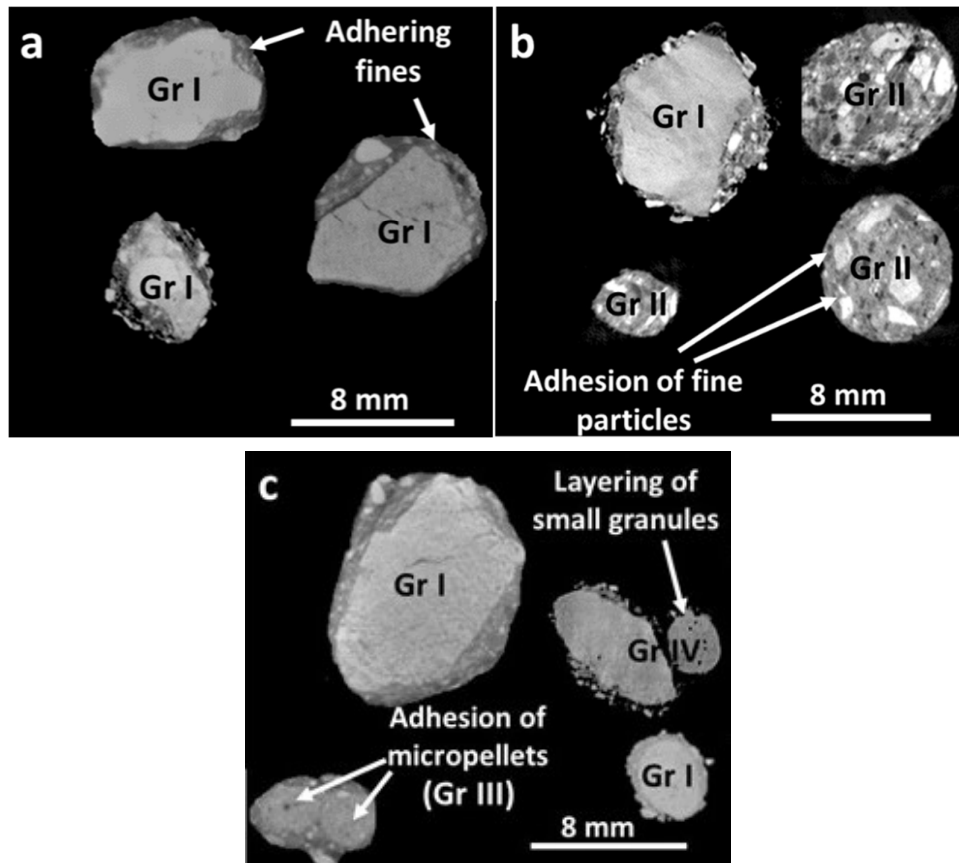
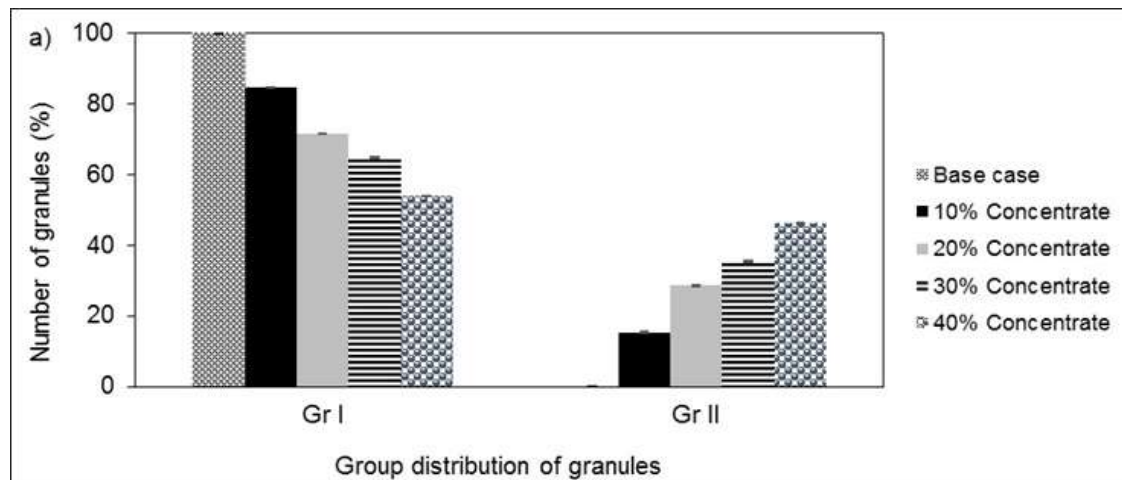


Figure 4.8. X-ray microtomographs of granules a) base case; b) with concentrate addition; c) with micropellet addition

The principal structure was obtained by the common process where the finer fraction of the sinter feed (-0.25 mm) adhered onto coarse particles, as shown in Figure 4.8. This structure is represented by granules of Group I (Gr I). The addition of concentrate resulted in the formation of granules with a pellet-like structure (Gr II). It is clear that the mechanism involved in the formation of these granules was the coalescence

process. The incorporation of micropellets in the ore mixtures produced granules of groups I, III and IV. Granules of Group III (Gr III) were obtained by adhesion of micropellets and those of Group IV (Gr IV) were formed by a two-stage layering process. Granules of Group I consisting of micropellets exhibited a thinner adhering layer compared to those of coarse particles.

The granules from the base case sample were only from Gr I, as they consisted of a core (coarse nuclei particles) surrounded by a layer of fines (Figure 4.9). The addition of concentrate and micropellets resulted in the complex structures associated with Groups II–IV. The population of granules from Group I decreased with the addition of concentrate while that of granules with a pellet-like structure (Gr II, Figure 4.8b) increased (Figure 4.9). When micropellets formed the cores of granules from Group I, they were covered with a thinner layer of fines, compared to Group I granules, which had cores from coarse ore particles. Addition of micropellets decreased the population of granules from Group I (coarse particles as cores) while that of Group I (micropellets as cores) and Group III did not change significantly (Figure 4.9). Granules from Group IV were only formed in sinter mixtures with 40% micropellets.



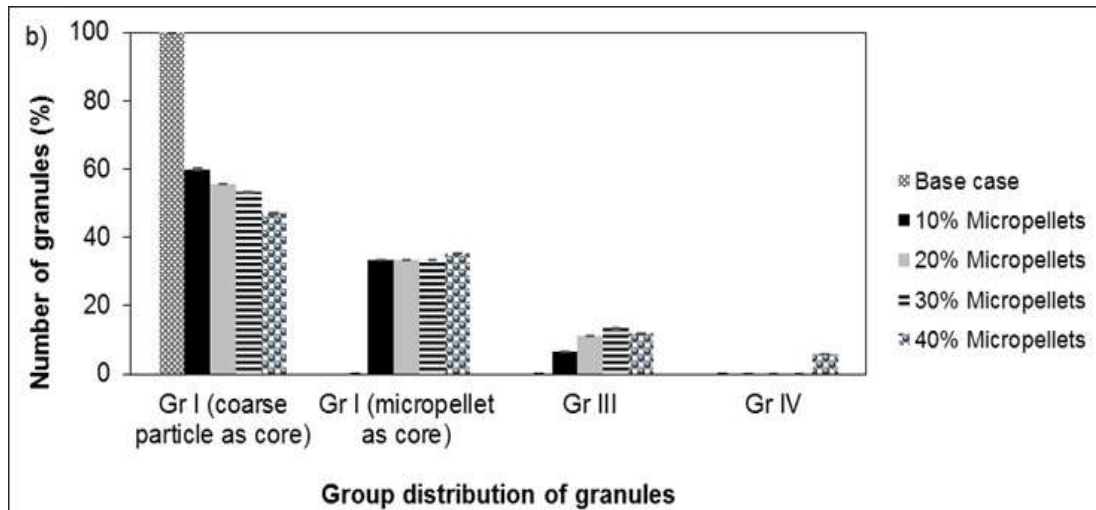


Figure 4.9. Group distribution of granules from ore mixtures with addition of (a) concentrate and (b) micropellets.

4.5.2. Three-dimensional shape of granules

4.5.2.1. Evaluation of the sphericity of each granule

Real granules are not regular particles, but have random shapes. To be able to characterise the shapes of granules, a set of parameters (particle volume, surface, length, width and thickness) was determined using X-ray microtomography. These parameters were extracted from the 3D images of randomly selected granules, as shown in Figure 4.10 and given in Table 4.3. The granules are quite angular and similar to crushed rocks. The finer particles are attached to the external surface of the granules (Gr. I), resulting in the formation of a rough surface of the granules and increase in their surface area.

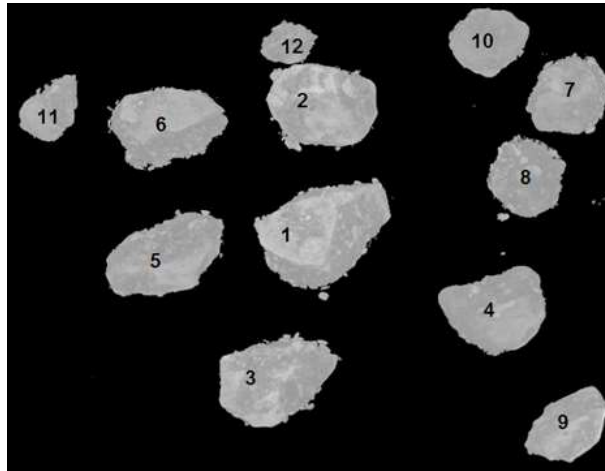


Figure 4.10. Images of granules (base case) captured by X-ray microtomography

Table 4.3. Geometric characteristics of granules from the base case sample

Granule number	Volume (mm ³)	Surface (mm ²)	Length (mm)	Width (mm)	Thickness (mm)
1	324.69	687.12	12.74	9.22	7.03
2	249.92	805.26	11.64	9.87	5.86
3	169.24	535.47	10.47	10.05	4.88
4	145.80	409.56	9.22	6.65	5.37
5	125.02	393.95	8.77	8.13	4.69
6	116.75	328.67	8.69	8.54	4.12
7	99.90	429.60	7.90	5.97	5.67
8	94.64	223.26	7.56	7.56	3.97
9	42.89	163.12	6.50	4.91	3.52
10	37.44	134.26	5.37	4.91	3.63
11	34.57	123.81	7.03	5.29	3.02
12	23.67	122.86	5.41	4.38	3.02

Data from Table 4.3 were subsequently used to calculate different types of sphericity and shape factors of granules (Table 4.4). These results show that the true sphericity values are consistently lower than the operational sphericity, Krumbein sphericity, Corey shape factor and Janke form factor. Considering the equation of Wadell (1932), the true sphericity is inversely proportional to the real surface of the granule. This means that the more irregular the surface of the granule, the bigger the external area and the smaller the true sphericity for the same volume of the granule (Rankin et al., 1985, 1983). The operational sphericity, Krumbein sphericity, Corey shape factor and Janke form factor account for the edges of granules to construct a circumscribed rectangular cuboid. The surface area of the real granules is not considered.

Table 4.4. Sphericity and shape factors of the selected granules from base case

Granule number	True sphericity	Operational sphericity	Krumbein sphericity	Corey shape factor	Janke form factor
1	0.33	0.67	0.74	0.65	0.71
2	0.24	0.67	0.75	0.55	0.62
3	0.28	0.66	0.76	0.48	0.55
4	0.33	0.71	0.75	0.69	0.74
5	0.31	0.71	0.81	0.53	0.61
6	0.35	0.70	0.78	0.48	0.55
7	0.24	0.73	0.82	0.83	0.86
8	0.45	0.75	0.81	0.53	0.60
9	0.36	0.67	0.74	0.62	0.69
10	0.40	0.77	0.85	0.71	0.77
11	0.41	0.57	0.69	0.50	0.56
12	0.32	0.66	0.77	0.62	0.69

4.5.2.2. Mean value of each shape parameter for the granulated mixture

The mean of shape factor for each granulated mixture (aggregate of different granules) was expressed as an arithmetic mean of each shape parameter (sphericity or shape factor) of the granules selected from the granulated mix sample (Eq. 4.3).

$$\text{Mean of shape factor} = \frac{1}{n} \sum_{i=1}^n \text{shape parameter of granule } i \quad \text{Eq. 4.3}$$

where n is the number of the examined granules from each granulated mix sample. The number of the selected granules from each mixtures are listed in Table 4.5.

Table 4.5. Number of the selected granules

	Base mixture	Mixture with concentrate				Mixture with micropellets			
		10%	20%	30%	40%	10%	20%	30%	40%
Number of granules	12	13	14	17	13	14	18	15	15

The mean values of each shape parameter (true sphericity, operational sphericity, Krumbein sphericity, Corey shape factor and Janke form factor) are shown in Figure 4.11. The mean values of the true sphericity are the smallest among the averaged values of different sphericity and shape factors. The granules that were produced by adherence of fines to large particles had a rough external surface, which results in an increase in their surface area and decrease in true sphericity (Rankin et al., 1985, 1983).

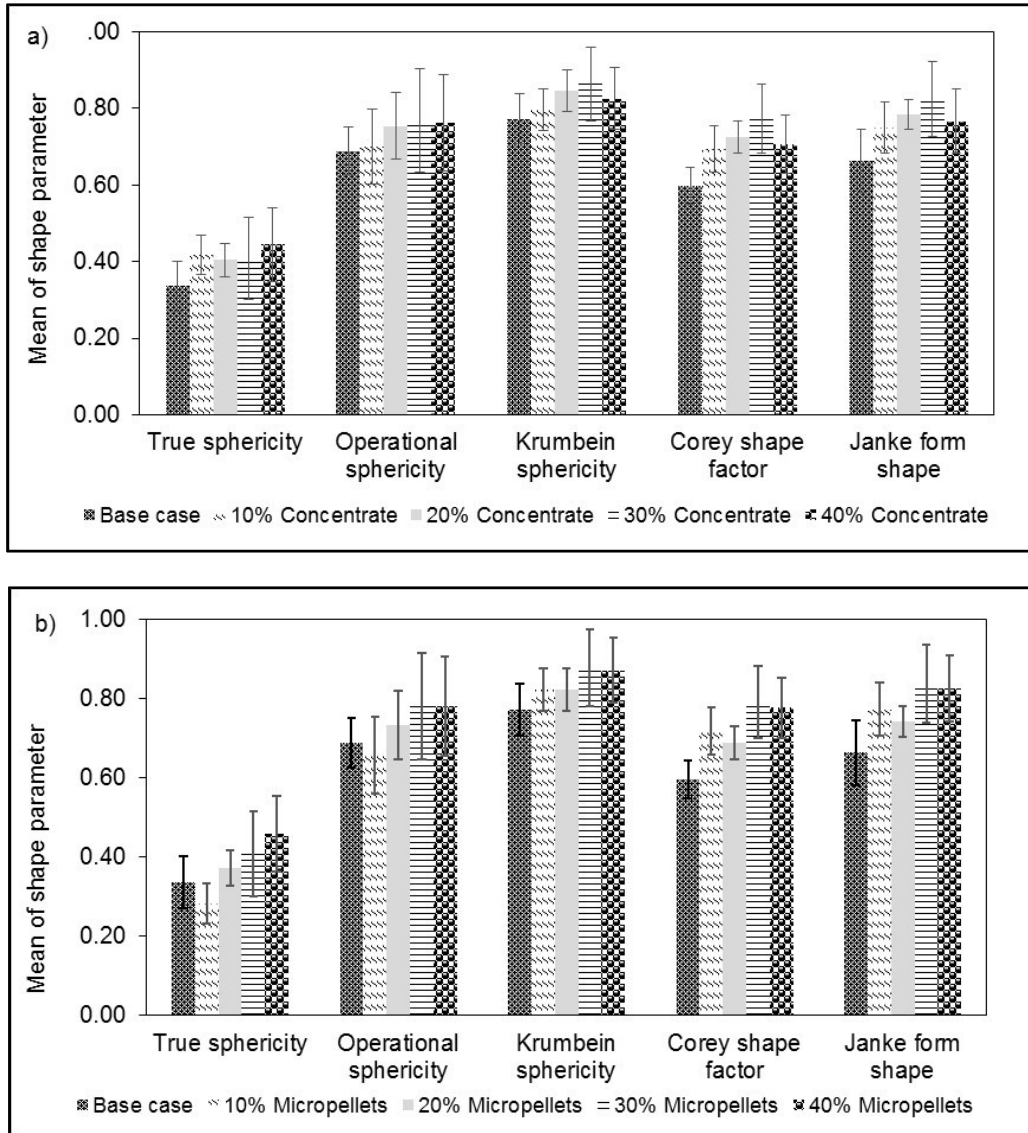


Figure 4.11. Mean values of true sphericity, operational sphericity, Krumbein sphericity, Corey shape factor and Janke form factor for granules with a) concentrate and b) micropellets

There is an increase in each shape parameter with addition of concentrate and micropellets to the ore mixtures (Figure 4.11). This was caused by the formation of granules of Group I (with micropellets as core), Group II (coalescence of microgranules) and Group III (adhesion of micropellets) (Figure 4.9). For mixtures with 40% concentrate and 40% micropellets, the deformation of granules from Group II (coalescence of microgranules) and the formation of granules from Group IV (two-layering process) respectively caused the shape parameters to slightly decrease.

4.5.3. Effect of the granule shape on the green bed permeability

For the purpose of correlating the granule shape with the bed permeability, an overall sphericity of each granule sample was defined as a mean sphericity, which is the arithmetic average of the mean values of the five shape parameters (operational sphericity, Krumbein sphericity, Corey shape factor and Janke form factor). The mean sphericity values of the nine granulated mixtures are shown in Figure 4.12. These values are widely spread between 0.61 and 0.74.

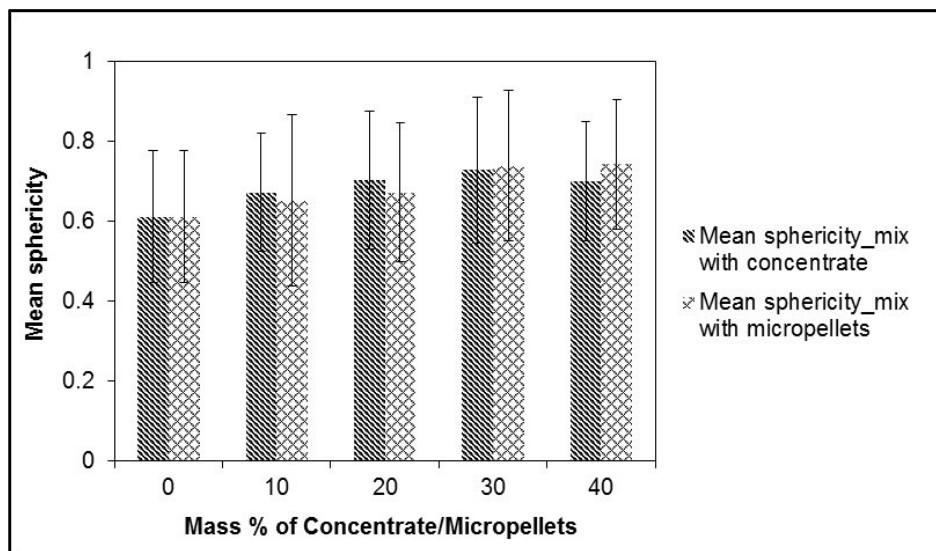


Figure 4.12. Mean sphericity of the granulated mixtures with concentrate and micropellets

The variation of the mean sphericity to that of the maximum bed permeability as the mass percent of concentrate and micropellets increased, is compared in Figure 4.13. The mean sphericity increases and reaches a maximum at 30% of concentrate and 40% of micropellet addition. Further addition of concentrate resulted in granules of Group II that could easily deform and deviate from the spherical shape. In granule sample with more micropellets (40%), granules of Group III and IV started to form. They are less spherical due to micropellet – micropellet and micropellet – granule adhesion. These mechanisms could hinder the mean sphericity to increase even though more spherical particles (micropellets) were added to the base mixture.

The bed permeability however decreased with addition of concentrate and micropellets to the base mixture (Figure 4.13). Concentrate was involved in the coalescence mechanism, resulting in the formation of granules of Group II. These granules were spherical and likely had less particle-to-particle interlock which could result in the formation of compact beds with low permeability (Hinkley et al., 1994a; Rankin et al., 1985, 1983). These granules could also be deformable and reduce the voidage as well as the bed permeability (Hinkley et al., 1994b). Replacement of fine iron ore by micropellets resulted in granules of Group I, III and IV. The granules of Group I that had micropellets as cores were more spherical and smaller than those from the base case. In Group III, the granules were spherical while the granules from Group IV could disintegrate into their constituents (Kapur et al., 1993; Venkataramana et al., 1999). It was evident that the sinter bed with micropellet addition was formed of different types of granules: small (Gr. I), spherical (Gr. III) and breakable (Gr. IV). This could explain the observed decrease in bed permeability as the mass fraction of micropellets increased.

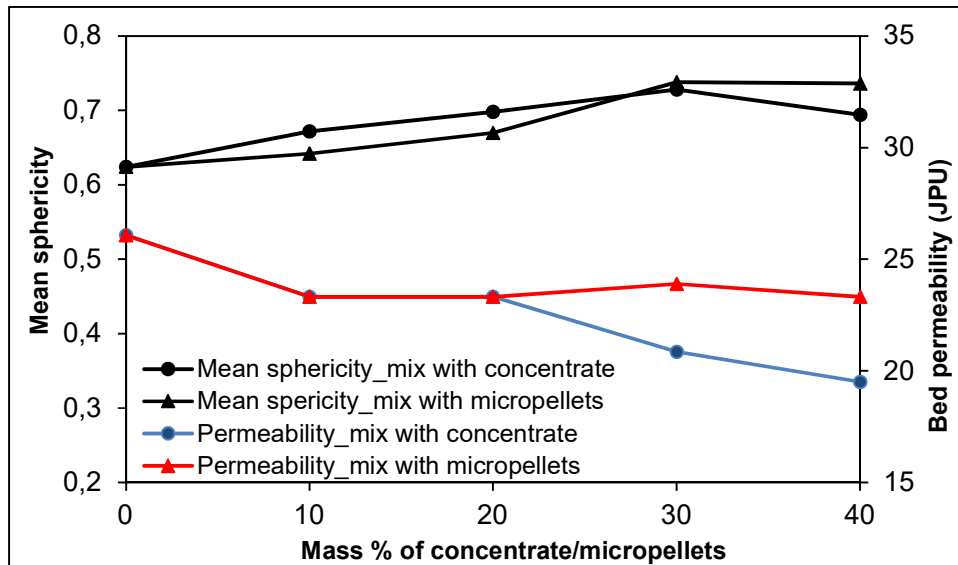
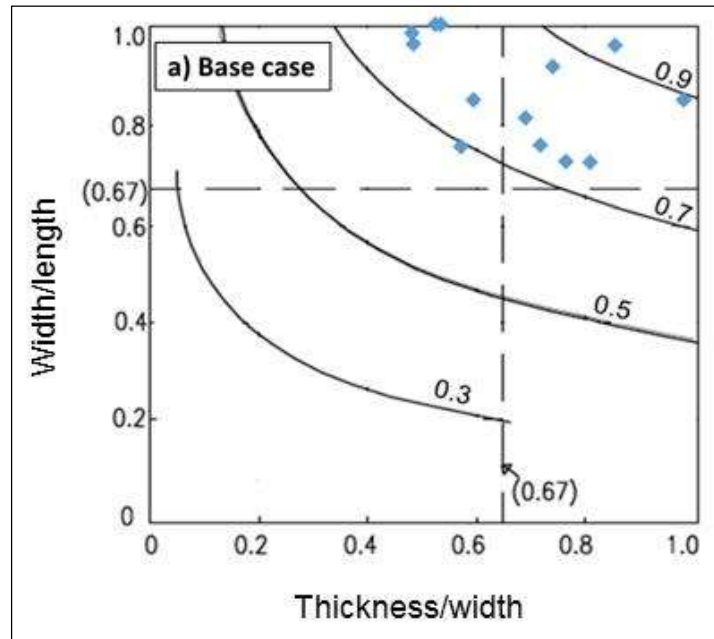


Figure 4.13. Effect of concentrate and micropellet addition on the mean sphericity and bed permeability

4.5.4. Sphericity distribution using the Zingg diagram

The classification of granule shape using the Zingg diagram is often used as a complementary tool in the determination of granule/particle shape. This method is quick and can easily classify any particle based on its three linear dimensions (length, width and thickness). The sphericity distribution for different granules was compared with the predefined shapes as shown in Figure 4.14. It can be seen that most sphericity values fall into the spherical region where the ratio of the smaller over the bigger dimension is larger than $2/3$. The granule sphericity for the base mixture varies between 0.7 and 1. The addition of concentrate and micropellets to the base mixture moves the clusters of data towards the upper right-hand corner of the diagram. This can be confirmed by plotting the population of granules against the range of Krumbain-Sloss sphericity (Figure 4.15). Most granules (90%) from the base case had a sphericity that falls between 0.7 and 0.9. Granule samples with concentrate consisted of 77% and 20% of granules with sphericity range of 0.7 – 0.9 and 0.9 – 1 respectively. The percentage of the granules in 0.7 – 0.9 and 0.9 – 1 were respectively 53% and 42% for granules that contain micropellets.



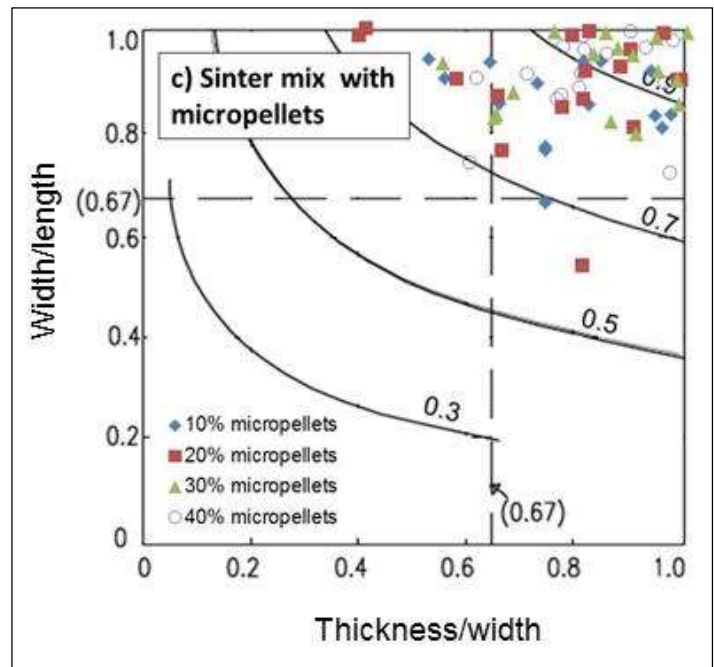
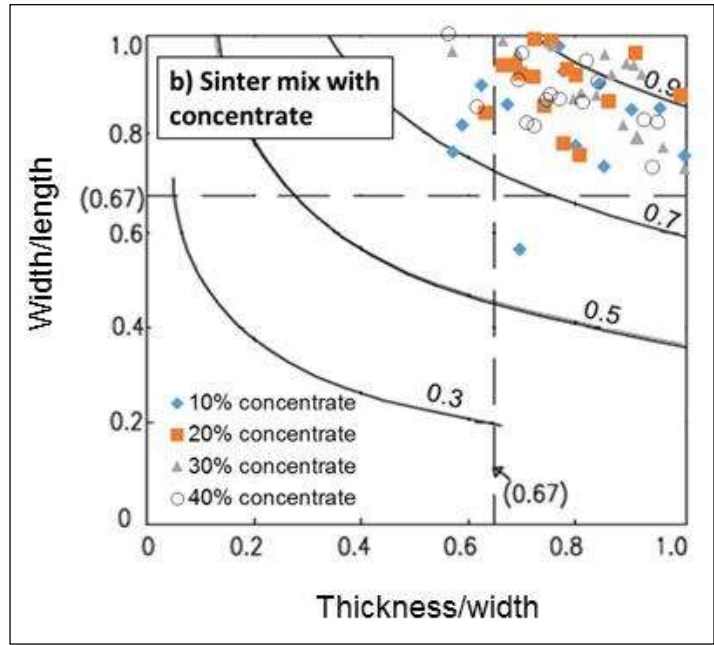


Figure 4.14. Variation of granule shape using Zingg's diagram

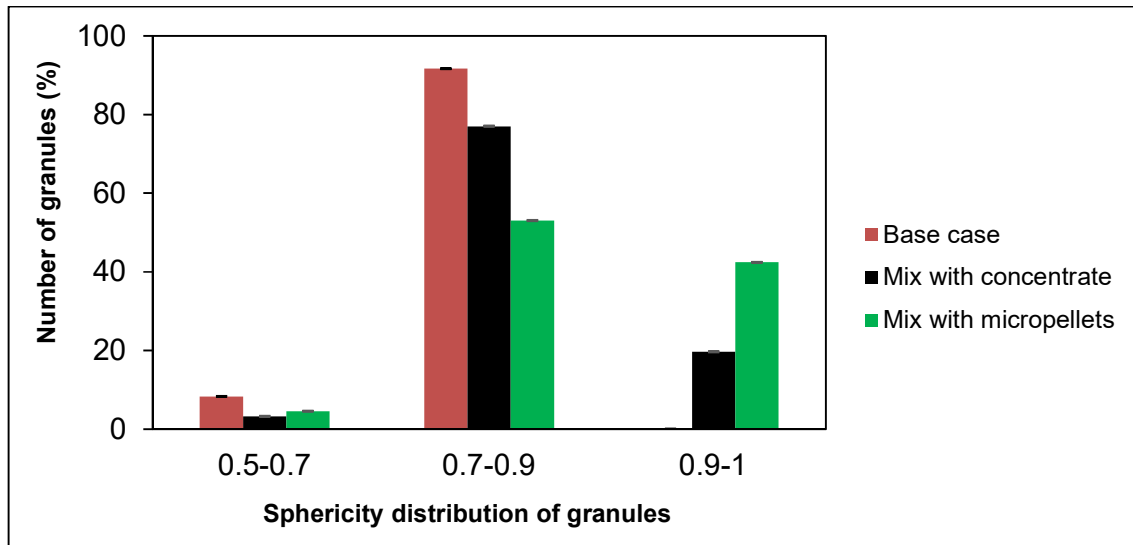


Figure 4.15. Sphericity distribution of the population of the granules from base mixture and mixtures with concentrate and micropellet addition

4.6. Conclusion

Qualitative and quantitative information about the geometry and microstructure of iron ore granules in mixtures with concentrate and micropellets were obtained, using X-ray microtomography. The following conclusions can be drawn:

- Four mechanisms governed the formation of granules in mixtures that contain iron ore fines, concentrate and micropellets. Auto layering was the main mechanism. With the addition of concentrate, coalescence became a minor mechanism, while with the addition of micropellets, adhesion between micropellets and between granules and micropellets became a minor mechanism.
- The average values of five shape parameters were used to characterise the shapes of the produced granules. The addition of concentrate and micropellets increased the average sphericity of the granules. Increased addition of concentrate resulted in a slight decrease in the mean sphericity, due to the production of granules that can easily deform and deviate from the spherical shape.

- The increase in mean sphericity with the addition of concentrate and micropellets in the granulated mixtures may have contributed to the formation of sinter beds with lower bed permeability. This result was confirmed by the sphericity distribution from Zingg diagram. The distribution of granule sphericity showed that the bed permeability decreased with an increase in the population of granules in the 0.9-1 sphericity range.
- The variation of the permeability of the sinter beds containing concentrate and micropellets could not be exclusively explained by a single parameter but rather by a combined effect of mean sphericity, mean size, sphericity distribution, structure and deformation of granules.

5. Prediction of the granule size distribution of iron ore sinter feeds that contain concentrate and micropellets

5.1. Introduction

Granulation of fine iron ore remains more an art than a science and, consequently the granule size distribution is still determined experimentally. Extensive laboratory and pilot scale tests are commonly carried out due to the importance of granulation in the production of pig iron. To predict the granulation behaviour and granule size distribution, researchers have proposed the population balance equations (Adetayo et al., 1995; Ball et al., 1973; Ennis and Litster, 1997).

Population balance equations consist of modelling the averaged properties of the whole population (granule size) rather than the behaviour of each individual particle (Adetayo et al., 1995; Ball et al., 1973; Ennis and Litster, 1997). These equations are concerned with a narrow size distribution of particle feed. In addition, the granule size distribution is conveniently predicted by one-dimensional population balances for processes where only particle size controls the growth behaviour (Iveson, 2002). Similarly, population balance equations have been developed to predict the size distribution of the agglomerates in the granulation of iron ore with a broader size distribution (Kapur et al., 1993; Litster et al., 1986; Litster and Waters, 1986; Venkataramana et al., 1999; Waters et al., 1989). These models are however scarce in the open literature due to the complexity of mechanisms involved during the process and the huge number of parameters.

Modelling of iron ore granulation requires an understanding of the process, which will determine the mechanisms of particle size enlargement. Based on the X-ray microtomographic analysis of granules (Chapter 4), it was concluded that the principal mechanism of iron ore granulation is based on the auto layering process. This mechanism was confirmed by microscopically analysing granules, which mostly showed a core (large primary particle and micropellet) surrounded by a layer of fines (Nyembwe et al., 2016a, 2016b).

In laboratory-scale batch granulation, the model of Litster is often used to predict the size distribution of granules produced through the adherence of fines onto large particles (Litster et al., 1986; Litster and Waters, 1986). This model was initially validated for predicting the granule size distribution in granulated mixtures for single sinter feeds. For a broader range of sinter feeds, its validity was verified by the work of Waters et al. (1989) and Litster and Waters (1990). Good agreement was reached between the predicted and experimental values of the Sauter mean diameter.

This chapter presents the validation of Litster's model for iron sinter feeds containing concentrate and micropellets. Model predictions of granule size were compared to the experimental Sauter mean diameter by evaluating the mean absolute percentage error (MAPE). Granule growth was also investigated to identify the influence of concentrate and micropellet addition on the granulation process.

5.2. Background to Litster's model

Population balance equations are crucial in the granulation process because they provide a framework for size distribution (Adetayo et al., 1995; Ball et al., 1973; Ennis and Litster, 1997; Litster et al., 1986; Litster and Waters, 1986; Waters et al., 1989). The model of Litster consists of a population balance based on the auto layering of finer material onto nuclei particles (Litster et al., 1986; Litster and Waters, 1986). This model does not take into account the kinetic aspects of the process and predicts the final granule size distribution by relating the masses of particles in the feed to the final mass of the granules.

Litster et al. (1986) primarily defined a partition coefficient that represents the probability for particles of a certain size fraction (x) to act as nuclei or seeds. In general, particles that exclusively act as nuclei have a partition coefficient of 1, while those with no probability of being used as nuclei have a partition coefficient of 0. Particles with a partition coefficient of 0 therefore report only to the adhering layer.

For any ore mixture, Litster et al. (1986) described the partition coefficient as a lognormal distribution function:

$$\alpha(x) = \frac{1}{\sigma\sqrt{2\pi}} \int_{-\infty}^{\ln(x)} \exp\left[-\frac{(t - \ln(x_{0.5}))^2}{2\sigma^2}\right] dt \quad \text{Eq. 5.1}$$

where σ is the partition curve parameter and represents the spread of size range of intermediate particles and $x_{0.5}$ is the particle size with a partition coefficient of 0.5.

From a mathematical point of view, the population balance equations can determine how changes to input conditions affect the size distribution of the granulated material. To develop the model, the following assumptions were considered (Litster et al., 1986; Litster and Waters, 1986; Rankin et al., 1983; Waters et al., 1989):

- (1) Granulation merely occurs by auto layering of fines onto the surface of larger nuclei particles and the extent of coalescence is minimal.
- (2) For each size fraction i , the fraction of particles that act as nuclei can be represented by a partition coefficient.
- (3) The effects of the particle shape, density, and chemical composition are assumed to be secondary.
- (4) The adhering fine to nuclei ratio (R) is independent of the size of the nuclei particle.
- (5) The absorption of moisture by particles is independent of particle size and size distribution.

Litster et al. (1986) suggested that primary particles which act as nuclei will appear in granules of the same size fraction, or the next larger size fraction due to an increase in size and adherence of fines onto the nuclei particles. It was experimentally

established that the partition coefficient or the proportion of particles of a given size i that act as nuclei can be expressed using Eq. 5.2.

$$\alpha_i = \frac{M_{ii} + M_{ii+1}}{\sum_{j=1}^n M_{ij}} \quad \text{Eq. 5.2}$$

where M_{ij} is the mass of particles of size fraction i which are found in granules of size fraction j .

Waters et al. (1989) extended the model of Litster to a multicomponent system that is used in real granulation processes. Based on a one-dimensional population balance equation, the granule size of each size fraction was related to the corresponding particle size of sinter feed and the thickness of adhering fines. For a given size fraction i , the corresponding granule size can be expressed by:

$$x_{gi} = x_i + 2 \Delta_i \quad \text{Eq. 5.3}$$

where x_{gi} , x_i and Δ_i are the top size of granule size i , the top size of particle size fraction i , and the layer thickness respectively.

The thickness of the adhering layer is related to the mean size and mass ratio of adhering fines to nuclei particles.

$$2\Delta_i = \frac{R_i \bar{x}_i}{K} \phi_i \quad \text{Eq. 5.4}$$

where R_i is the mass ratio of the adhering layer to nuclei for granules in size fraction i . \bar{x}_i is the geometric mean size of the size fraction i . ϕ_i is a lumped parameter depending on the density of each component in the feed. K is a parameter that relates layer

thickness to the mass of adhering particles. An average value of $K = 4$ is accepted for single and multicomponent systems (Litster et al., 1986; Litster and Waters, 1986; Waters et al., 1989).

According to the assumptions of the model, R is independent of nuclei particle size and can be calculated as follows (Litster et al., 1986; Litster and Waters, 1986; Waters et al., 1989):

$$R_i = R = \frac{\sum_{i=1}^n \sum_{k=1}^m (1 - \alpha_i) \delta_k w_{ik}}{\sum_{i=1}^n \sum_{k=1}^m \alpha_i \delta_k w_{ik}} \quad \text{Eq. 5.5}$$

where δ_k is the weight percent of component k in the feed and w_{ik} is the weight percent of feed component k in size fraction i .

The parameter ϕ_i is related to the thickness of the adhering layer and the density of the feed component (Eq. 5.6):

$$\phi_i = \frac{\sum_{k=1}^m \delta_k w_{ik} \frac{\sum_{i=1}^n \sum_{k=1}^m (1 - \alpha_i) \delta_k w_{ik}}{\rho_k}}{\sum_{k=1}^m \frac{\delta_k w_{ik}}{\rho_k} \sum_{i=1}^n \sum_{k=1}^m (1 - \alpha_i) \delta_k w_{ik}} \quad \text{Eq. 5.6}$$

For a single system, ϕ_i is assumed to be 1. Similarly the value of 1 was used in the case of a multicomponent system without introducing major errors (Litster et al., 1986; Litster and Waters, 1986; Waters et al., 1989).

Assuming that the top size is comparable to the geometric mean size for each size fraction, Eq. 5.3 can be rewritten as:

$$x_{gi} = x_i \left(1 + \frac{R}{K}\right) \quad \text{Eq. 5.7}$$

While the full derivation of the model is given by Waters et al. (1989), the model is able to predict the mass fraction of granule (w_{gi}) in size fraction i:

$$w_{gi} = \alpha_i(1 + R) \sum_{k=1}^m (\delta_k w_{ik}) \quad \text{Eq. 5.8}$$

5.3. Materials and methods

5.3.1. Raw materials and mixtures before granulation

The compositions and particle size distributions of the nine ore mixtures investigated are specified in Table 3.1 and Table 3.2. The Sauter mean diameters (SMD) of mixtures before granulation are given in Table 5.1. The addition of concentrate decreases the SMD of the mixtures from 0.49 mm to 0.20 mm. Whilst there is no significant change in the SMD of mixtures with addition of micropellets. All tested mixtures were those obtained at optimum moisture.

Table 5.1. Sauter mean diameter (SMD) for examined mixtures before granulation

Mixtures	Sauter mean diameter (mm)	Mixtures	Sauter mean diameter (mm)
0% concentrate	0.49	0% micropellets	0.49
10% concentrate	0.36	10% micropellets	0.48
20% concentrate	0.29	20% micropellets	0.48
30% concentrate	0.23	30% micropellets	0.47
40% concentrate	0.20	40% micropellets	0.46

5.3.2. Partitioning of each particle size to different granule size fractions

Partitioning tests were performed in order to experimentally determine the contribution of different primary particle fractions to the different granule size fractions. The method used in this study was not first freezing of wet granules before screening, because granules adhered to each other and formed hard blocks, which were difficult to screen. The green granules were therefore slightly dried in a laboratory oven at 70°C for 20 min. The dried granules were then gently screened into the following size fractions: – 0.250, +0.250 –0.50, +0.50 –1.00, +1.00 –2.00, +2.00 –4.75, +4.75 –10 mm. Each granule size fraction was weighed and dried at 115°C for 24 hours. After drying each granule size fraction was manually broken down so that the breakage of the primary particle could be minimised. The particles derived from each granule size fraction were then screened into different size fractions using sieves of 4.75, 2.00, 1.00, 0.50, 0.250, 0.125 and 0.063 mm.

5.3.3. Structural analysis of granules

Stereo microscopy and X-ray microtomography techniques were used to analyse the structures of the granules (sections 3.1.8 and 4.4).

5.4. Results and discussion

5.4.1. Particle partition distribution

The partitioning of particles for each particular size into the various granule size fractions was determined for samples that were first dried and manually screened. All granules were selected from mixture samples obtained at optimum moisture. Particle partition distributions for the base case at 5.5% moisture content are shown in Table 5.2.

Table 5.2. Particle partition distribution of the base case sample at 5.5% moisture

Granule size distribution	Particle size distribution (mass %)							
	+4.75 mm	+2.00 mm	+1.00 mm	+0.50 mm	+0.25 mm	+0.125 mm	+0.063 mm	-0.063 mm
+4.75 mm	100.00	57.54	17.28	30.23	47.85	65.97	66.55	46.01
+2.00 mm		42.46	64.53	37.92	38.60	22.11	25.01	33.83
+1.00 mm			18.19	25.04	9.57	8.34	5.81	16.24
+0.50 mm				6.80	2.55	2.54	1.34	2.71
+0.25 mm					1.44	0.69	0.98	1.08
- 0.25 mm						0.36	0.31	0.14

From the particle partition distributions, the partition coefficient of each particle size fraction was determined by using Eq. 5.2. For each mixture, the partition coefficients (α_i) related to a particle size fraction (i) is shown in Table 5.3. In addition, the partition curve parameter (σ) was experimentally determined. It represents the spread of the size range of intermediate particles. The partition curve parameter ranged from 0.61 to 0.72 and 0.54 to 0.65 for mixtures with addition of concentrate and micropellets, respectively (Table 5.3). It is clear that the mixture with no addition of concentrate or micropellets has a small size range of intermediate particles ($\sigma=0.52$), and is likely to have higher granulation effectiveness than mixtures with concentrate and micropellets. The partition curve parameter (as size distribution spread) increases from 0.52 to 0.72 as the concentrate content increases. While the incorporation of micropellets into the base case does not increase the partition curve parameter at the same level as that of mixtures with concentrate addition. This might contribute to the high permeability of mixtures with 30% and 40% micropellet content than that of mixtures with 30% and 40% concentrate.

Table 5.3. Partition coefficient of particle size fraction

Mixtures	Partition coefficient, α_i						partition curve parameter (σ)
	+4.75 mm	+2.00 mm	+1.00 mm	+0.50 mm	+0.25 mm	- 0.25 mm	
Base case	1.00	1.00	0.83	0.32	0.04	0.01	0.52
10% Concentrate	1.00	1.00	0.85	0.51	0.07	0.01	0.61
20% Concentrate	1.00	1.00	0.90	0.56	0.18	0.03	0.65
30% Concentrate	1.00	1.00	0.91	0.74	0.22	0.04	0.69
40% Concentrate	1.00	1.00	0.92	0.68	0.32	0.06	0.72
10% Micropellets	1.00	1.00	0.95	0.69	0.14	0.03	0.54
20% Micropellets	1.00	1.00	0.93	0.71	0.22	0.04	0.61
30% Micropellets	1.00	1.00	0.92	0.71	0.16	0.04	0.62
40% Micropellets	1.00	1.00	0.92	0.67	0.07	0.01	0.65

5.4.2. Comparison of Litster's model to measured data

The applicability of the Litster model was evaluated by comparing the measured and predicted granule size distribution or granule size for the tested mixtures. To completely define the model, two parameters were used. The lumped parameter $K=4$ was used as experimentally determined by Litster et al. (1986) and Litster and Waters (1986). The second parameter was the ratio (R) of adhering fines to nuclei, which was calculated using Eq. 5.5. For tested mixtures, corresponding values of R are plotted in Figure 5.1.

It can be seen that concentrate addition increases the ratio of adhering fines to coarse particles as expected (Figure 5.1). The ratio of the - 0.25 mm to +1.00 mm size fraction varied from 0.19 to 0.60 when the mass fraction of concentrate changes from 0% to 40% (Table 3.3). Incorporating micropellets in the base mixture shows a decrease in

ratio R. The ratio of - 0.25 mm to +1.00 mm size fraction decreased from 0.19 to 0.17 with addition of micropellets from 0% to 40%. The deficiency of finer material resulted in the production of granules where micropellets are surrounded with a smaller adhering layer (Figure 4.8c).

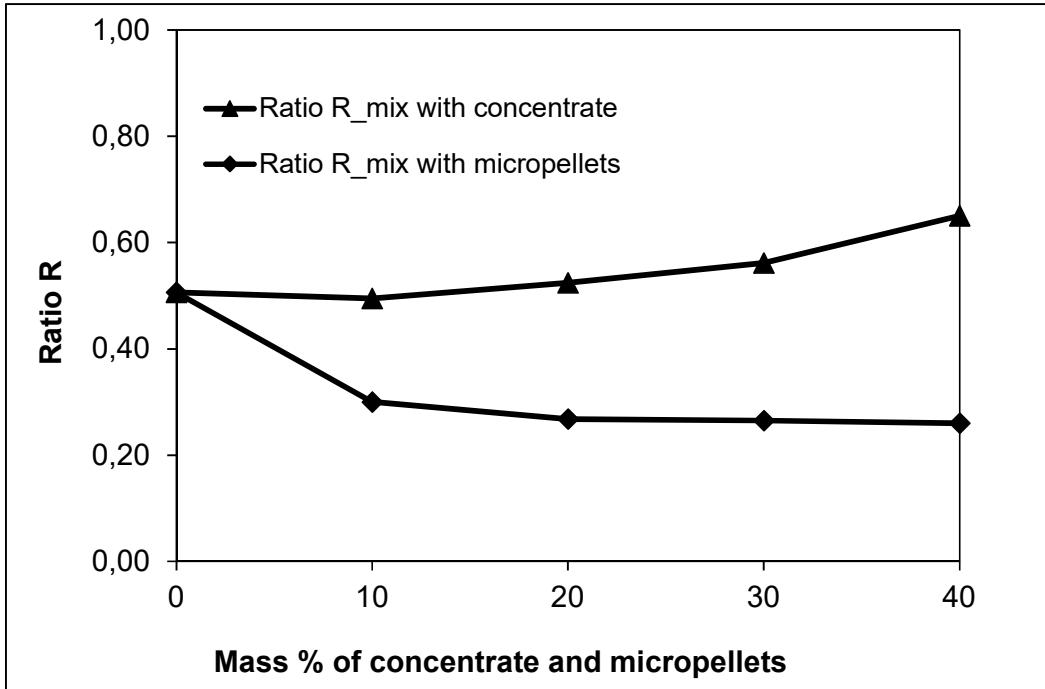
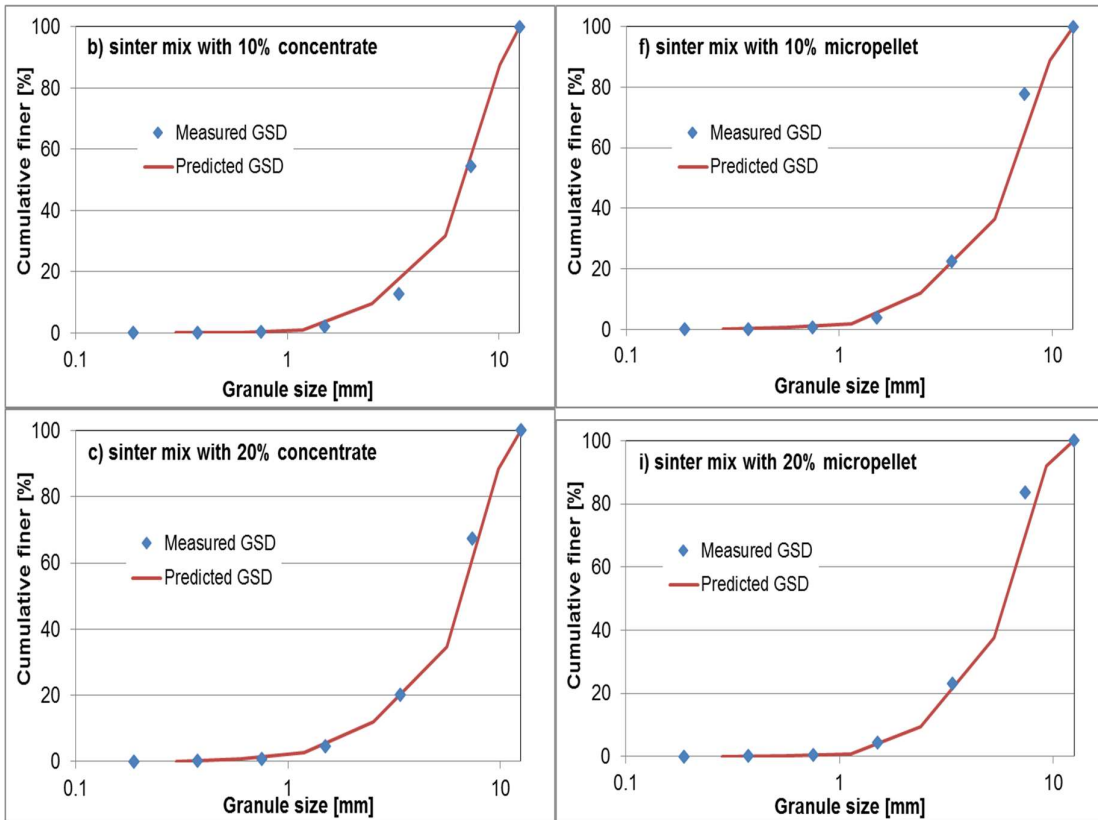
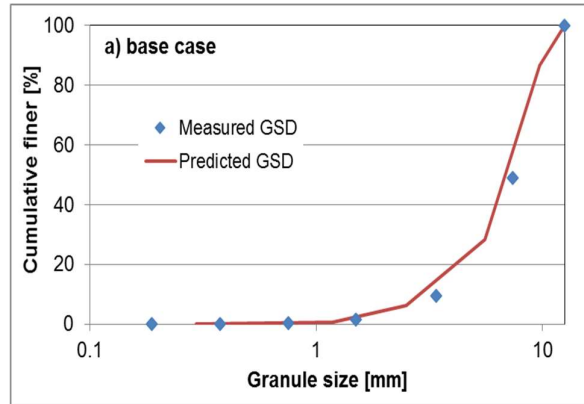


Figure 5.1. Variation of the ratio R with concentrate and micropellet addition at optimum moisture content

The predicted and measured granule size distributions are plotted in Figure 5.2(a - j). Comparative results were obtained for the base case and sinter feeds containing concentrate and micropellets. It was also established that other mechanisms such as coalescence, adhesion of micropellets and two-stage auto layering have a minor effect on the layering process.



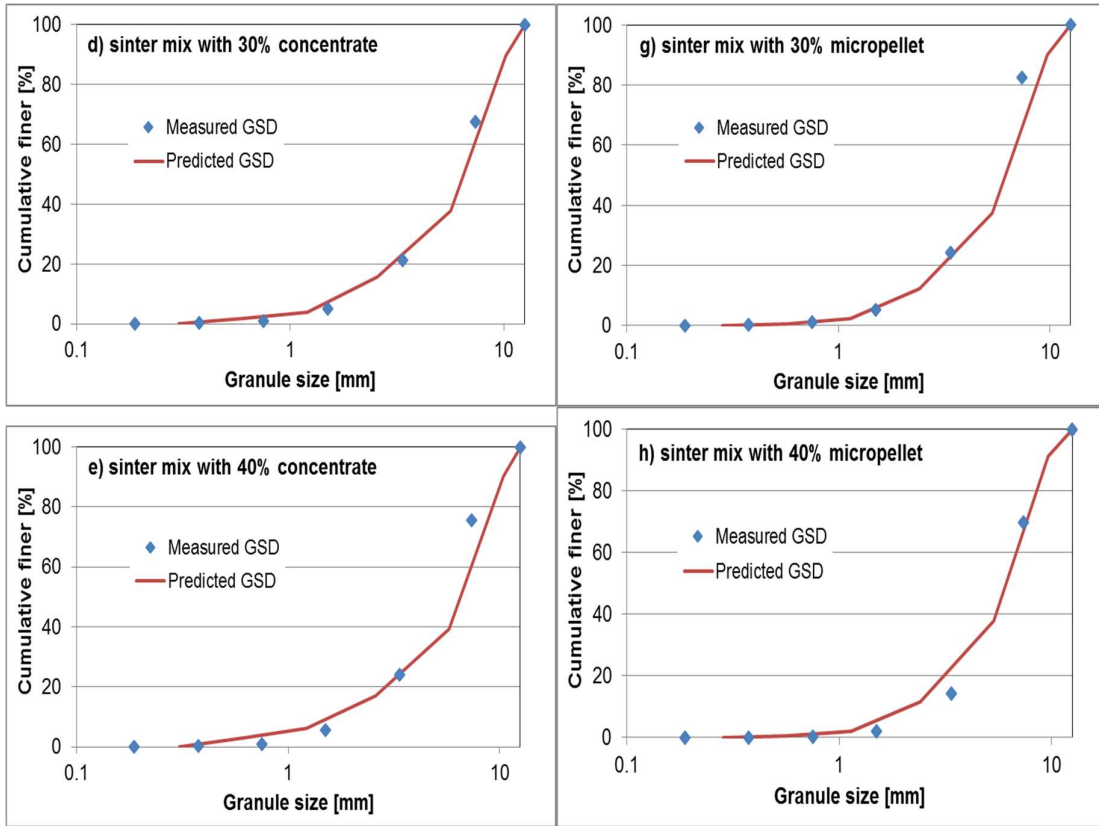


Figure 5.2. Comparison of model predicted and experimental granule size distributions for the different mixtures: (a): base case; (b) to (e): 10% - 40% concentrate; (f) to (i): 10% - 40% micropellets.

The validation of Litster's model was also achieved by calculation of the mean absolute percentage error (*MAPE*) between experimental Sauter mean diameter of granules and the predicted ones. The mean absolute percentage is defined as the percentage of the average of the absolute errors and determines how close predictions are to the experimental values. In general, a *MAPE* less than 10% indicates a very good agreement between experimental and predicted data. The *MAPE* can be computed from Eq. 5.9 (Makridakis and Wheelwright, 1989):

$$MAPE (\%) = 100 * \left[\frac{\sum_n |d_{s_exp} - d_{s_pred}|}{\sum_n d_{s_exp}} \right] \quad \text{Eq. 5.9}$$

where d_{s_exp} and d_{s_pred} are respectively the experimental and predicted Sauter mean diameters. The number of tests is represented by n .

The values of mean average percentage error (MAPE) for tested mixtures at optimum moisture content are shown in Figure 5.3.

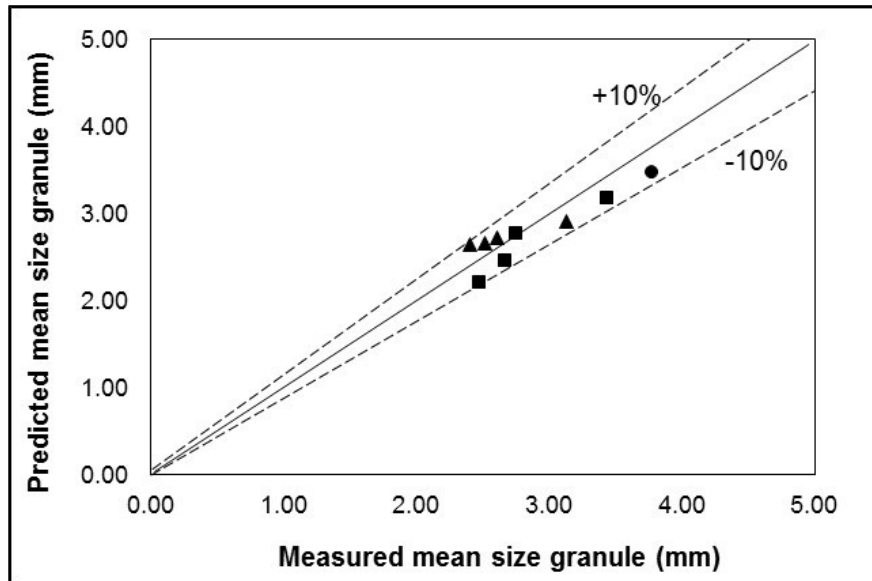


Figure 5.3. Comparison of model predicted and experimental granule sizes for the different mixtures. ●: base case; ■: concentrate; ▲: micropellet.

From Figure 5.3, it can be seen that the predicted and measured mean granule sizes for mixtures with concentrate and micropellet additions are very similar. The MAPE values for all mixtures with concentrate and micropellet additions are less than 10%, which is acceptable for the accuracy of the Litster’s model (Litster et al., 1986; Litster and Waters, 1986). Hence, the addition of concentrate and micropellets did not significantly alter the mechanism of granulation.

5.4.3. Variation of partition coefficient parameter $x_{0.5}$ and granule growth with addition of concentrate and micropellets

According to the model of Litster, the particle coefficient parameter $x_{0.5}$ is an important parameter to completely define the partition coefficient function (Litster et al., 1986; Litster and Waters, 1986). The variation of the particle coefficient parameter with

concentrate and micropellet addition is given in Figure 5.4. It is clear that the particle size decreases with the addition of concentrate and micropellets. This is due to the partial replacement of iron ore by finer/fine material such as concentrate (< 100 microns) and micropellets (2.31 mm mean size).

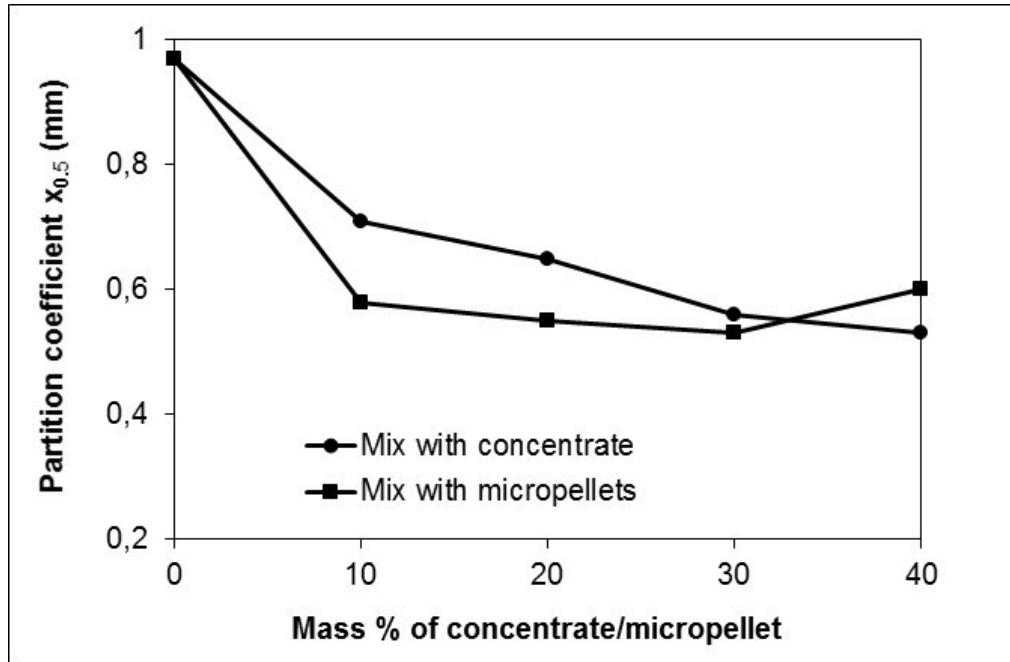


Figure 5.4. Effect of concentrate and micropellet addition on the partition coefficient parameter $x_{0.5}$

In granulation for iron ore sinter production where a layer of fines is formed around large particles, the granule growth becomes a vital parameter to assess the effectiveness of the process (Iveson et al., 2001; Silva and Rocha, 2002). In this study, the overall granule growth was defined by comparing the particle size before granulation with the granule size after granulation. The granule growth can be defined by the relation:

$$Growth (\%) = \frac{(d_{s_g} - d_{s_{feed}})}{d_{s_g}} * 100 \quad \text{Eq. 5.10}$$

where d_{s_g} and $d_{s_{feed}}$ are the Sauter mean diameter (SMD) after and before granulation respectively.

The granule growth in different mixtures is plotted in Figure 5.5. It can be seen that the variation of the granule growth slightly increases as the mass fraction of concentrate increases, whereas the particle coefficient parameter or granule size decreases. Additionally an increase in adhering fines promoted the layering of adhering fines around nuclei as well as the formation of microgranules (with pellet-like structure). The coalescence process hindered the growth of granules. The large nuclei particles that were likely to form big granules decreased. Consequently, the average granule size decreased as the amounts of concentrate increased. This was in contradiction with the “normal autolayering process”, whereby the addition of more concentrate (finer material) is supposed to produce granules with large mean size (Litster and Ennis, 2004; Litster and Waters, 1990, 1988; Wildeboer et al., 2005).

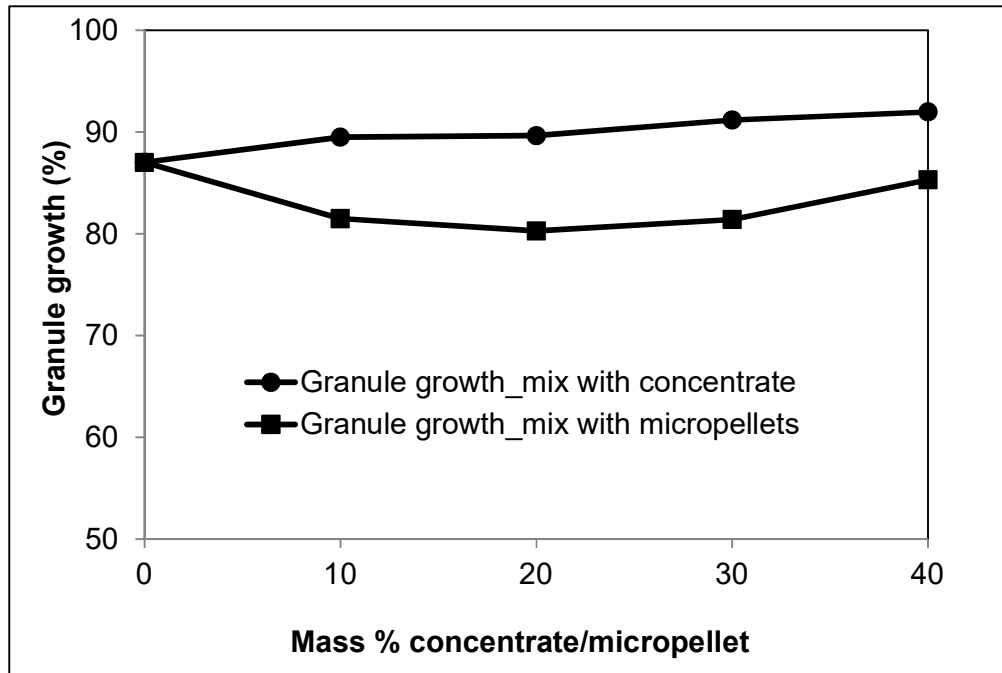


Figure 5.5. Variation of the granule growth with addition of concentrate and micropellets

In mixtures that contain micropellets, the granule growth decreases when the fraction of micropellets increases from 0% to 40%. The replacement of iron ore fines by micropellets decreased the ratio of adhering fines to coarse particles. The auto layering process was limited and produced smaller size fractions of granules than in

the mixture with no addition of micropellets (base case). In addition, the amounts of coarse nuclei particles (+4.75 mm) decreased from 9% to 6% while the mass percentages of small nuclei particle (-4.75mm +2.00 mm) increased as more micropellets were added to ore mixtures (Table 3.2).

5.5. Conclusions

Comparison of the Litster model and experimental results demonstrates the applicability of the Litster model in the prediction of the granule size for mixtures containing concentrate and micropellets. The main findings were:

- The ratio (R) predict the ratio of adhering fines to nuclei. For mixtures with concentrate, the fraction of adhering fines increased with addition of concentrate resulting in the formation of granules of Gr I and II. The addition of micropellets to mixtures created a deficiency of adhering fines. Small granules of Gr I started adhering together or to large granules of same group to form granules of III and IV.
- Good agreement was obtained between Litster's model and experiment results on the tested mixtures. The mean absolute percentage error was less than 10% throughout. This confirms that the adherence of fines onto coarse particles is still the major mechanism of granulation for the tested mixtures.
- The granule growth showed a strong correlation with the ratio of adhering fines to nuclei. The granule growth increased with an increase in concentrate content and ratio of adhering fines to nuclei. More adhering fines were available for the autolayering and coalescence mechanisms to take place. In mixtures with micropellet addition, the granule growth decreased with an increase in content up to 20%. This was driven by a decrease in the ratio of adhering fines to nuclei. Further addition of micropellets to mixtures (30% and 40%), the granule growth slightly increased due to the two additional mechanisms of granulation: adhesion of micropellets and two-stage autolayering.

6. Numerical validation of the pressure drop across glass bead beds using Rocky DEM – Fluent CFD coupling

6.1. Introduction

Flow through porous media is fundamental to many fields of engineering and science. In the sinter plant, a granulated mixture consisting of iron ore, return fines, fluxes and coke is loaded onto a moving grate and forms a bed of granules. The strand can vary from small to large machines with the area and height of the bed compatible with the auxiliary equipments used for suction of the outlet gas. The top of the bed is ignited and air is drawn through the bed causing the flame front to move down through the bed. Sintering occurs due to the high temperatures generated by the combustion of coke. The productivity of the sinter strand depends on the airflow/pressure drop through the bed, which in turn depends upon the bed voidage and the suction under grate. (Ellis et al., 2007; Hinkley et al., 1994a; Litster and Waters, 1988). At present the prediction of the pressure drop across the granulated sinter bed is performed by conducting experimental tests using a laboratory scale permeameter (sample pot). This approach is time consuming. It is also difficult to pack the bed in a repeatable manner, when repacking the same mixture.

Although the coupling of Discrete Element Method (DEM) with Computational Fluid Dynamics (CFD) has been extensively used in the prediction of flow characteristics through packed beds, a numerical model that predicts the pressure drop across the granulated mix in a permeameter has not been reported so far. Some studies reported the application of the DEM – CFD coupling in the modelling of the packed bed reactors and achieved good agreement between the predictions with the measured pressure drop (Bai et al., 2009, 2004; Eppinger et al., 2011). Eppinger et al. (2011) developed a numerical model of fixed bed reactors with small tube to particle diameter ratios. DEM-code was used to simulate the packing in a fixed bed consisting of randomly packed spherical particles. The fluid domain was meshed and solved with the commercial CFD-code STAR-CCM+. The predicted porosity and pressure drop was in agreement with measured data in the literature. Bai et al. (2009) developed a DEM-CFD model for the simulation of the flow field and pressure drop in fixed bed reactors

with randomly packed catalyst particles. The predicted pressure drop compared satisfactorily with the experimental measurements with errors of less than 10%, which is acceptable for industrial packed bed reactors (Bai et al., 2009, 2004).

In this study, one-way coupling of Rocky DEM and Fluent CFD was used to predict bed void fraction and pressure drop across packed beds. This chapter focuses on validation of the method using randomly packed spherical glass beads poured into a permeameter. Packed beds containing mono- and bi-sized glass beads were used to compare the measured pressure drops to the results predicted by the DEM-CFD model and the well-established correlations with the Ergun and MacDonald equations.

6.2. Background

The prediction of the void fraction and the pressure drop through packed beds has been a great challenge for researchers. Previous studies reported that the pressure drop through porous media or packed beds is highly dependent on the void fraction or porosity of the porous media. Rankin et al. (1985) reported that the pressure drop across a granulated mix is extremely sensitive to the void fraction of the packed bed. A small decrease in bed void fraction can cause a significant increase in the pressure drop through the packed bed under a given set of conditions. Hinkley et al. (1994b) found that a variation in void fraction from 0.35 to 0.4 causes approximately a 40% drop in pressure loss across the sinter bed at a given fluid flow rate. Leva and Grummer (1947) also reported that a 1% decrease in the porosity of the bed produced approximately an 8% increase in the pressure drop. For this reason, the granules or particles and the bed as a whole must be resistant to degradation and compaction during the experimental tests, and maintain a constant void fraction. To mitigate the inherent errors in the prediction of the void fraction and pressure drop across the packed bed, mathematical and numerical models were developed.

6.2.1. Mathematical approach

6.2.1.1. Void fraction

The most significant studies on void fraction prediction was performed by Dixon (1988) and Furnas (1931), where empirical equations were developed to determine the void fractions of packed beds. Dixon (1988) and Furnas (1931) conducted a series of experiments to determine the void fraction of the packed bed consisting of glass beads. They generated a huge number of experimental data using packed beds with different characteristics such as tube to particle diameter ratios, and fitted them into equations:

- Dixon's equation

$$\varepsilon = 0.4 + 0.05 (d_p/D) + 0.412 (d_p/D)^2 \text{ with } d_p/D \leq 0.5 \quad \text{Eq. 6.1}$$

- Furnas' equation

$$\varepsilon = 0.37 + 0.34 (d_p/D) \quad \text{Eq. 6.2}$$

where ε is the void fraction, d_p is the diameter of the particle and D is the diameter of the cylinder (tube).

For binary packed beds, Furnas (1931, 1929) developed mathematical equations to calculate the void fraction. The void fraction in a binary packing decreased to a minimum and then increased again with increasing mass percentage of large particles (Figure 6.1). It can be seen that the minimum value of the void fraction increases with increasing porosity of single particle size beds (fine or large particles only). Furnas (1931, 1929) also defined an optimal of large particles X_L at which a minimum void fraction of the binary mixture is achieved. X_L is often reached at a mass percentage of 70% large particles (Abe et al., 1979; Cumberland and Crawford, 1987; Fraser, 1935; Furnas, 1931, 1929, Mueller, 1997, 1991; Westman, 1936; Yu and Standish, 1988).

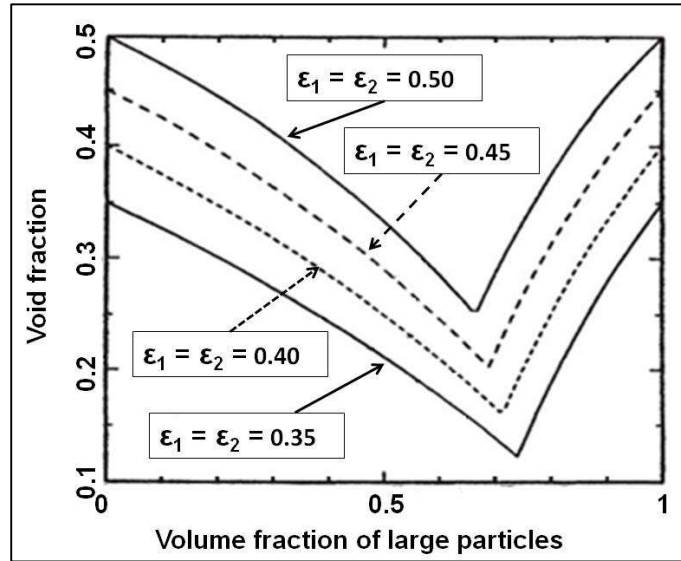


Figure 6.1. Void fractions of bi-sized packed beds. ϵ_1 and ϵ_2 are void fractions of mono sized packing (Furnas, 1929)

The mathematical model developed by Furnas was used to determine the minimum void fraction of binary mixtures as well as the optimal mass percentage of large particles (Eq. 6.3 and 6.4).

$$\epsilon_{min} = \epsilon_f \cdot \epsilon_L \quad \text{Eq. 6.3}$$

$$X_L = \frac{1 - \epsilon_L}{1 - \epsilon_{min}} \quad \text{Eq. 6.4}$$

where ϵ_{min} is the minimum void fraction of the binary packing while, ϵ_f and ϵ_L are the void fractions of the single sized fine and large particles respectively. For binary mixtures consisting of glass beads 3 and 6 mm in diameter, the values of minimum void fraction and optimal mass percentage of large particles are respectively 0.16 and 0.73 for $\epsilon_f = 0.38$ and $\epsilon_L = 0.41$. This is in agreement with the results found by Furnas, where the void fractions of the single size beds are close to 0.40 (Figure 6.1).

The Furnas model for binary mixtures assumes an ideal packing where fine particles are distributed into the interstices of large packed particles, without disturbing the packing of the large particles (Furnas, 1931, 1929). However, this type of model does not take into account the effects of interactions between particles on packing. The application of this model is therefore limited to relatively simple systems (Cumberland and Crawford, 1987; Fraser, 1935; Furnas, 1931, 1929, Mueller, 1997, 1991; Westman, 1936; Yu and Standish, 1988). For instance, fine particles cannot be accommodated in voids between large particles when a binary packing of beads with diameters of 3 and 6 mm is established. The ratio of big particle size to small size is small and this results in two types of interaction effects, depending on the mass percentages of the fine and large particles. An isolated fine and coarse particle in the packing can disturb the matrix of respectively large and fine particles, resulting in the formation of new structures of packed beds as well as deviations from the ideal packing model (Cumberland and Crawford, 1987; Fraser, 1935; Furnas, 1931, 1929, Mueller, 1997, 1991; Westman, 1936; Yu and Standish, 1988).

Zheng, Carlson and Reed (1995) developed an empirical equation, which takes into account the particle size ratio, the mass percentage of fine and large particles, and their initial void fractions (Eq. 6.5). The proposed equation was validated against experimental data, and predicted the void fraction (packing density) of binary mixtures more accurately:

$$\varepsilon_{mix} = \varepsilon_L - (1 - \varepsilon_f)\varepsilon_L \left| e \cdot X_f \ln X_f \right|^{\frac{5}{4(1-\varepsilon_L)}} \exp\left(-\frac{4}{R_{L/f}}\right) \quad \text{Eq. 6.5}$$

where ε_{mix} is the void fraction in a binary packing of different mass percentages of fine particles (X_f), ε_L and ε_f are the void fractions of single particle size beds (fine and large particles respectively), e and $R_{L/f}$ are respectively the base of the natural logarithm and the size ratio of large to fine particles.

6.2.1.2. Pressure drop calculation

The Ergun equation is the most commonly used model amongst empirical correlations that describes the pressure drop through a packed bed (Ergun, 1952). Ergun's equation for the pressure loss during the flow through a packed bed is represented by the sum of inertial and viscous energy losses. The viscous effects are described by linear and the inertial effects by quadratic dependence on the fluid superficial velocity. (Eq. 6.6):

$$\frac{\Delta P}{H} = k_1 \frac{\mu v (1 - \varepsilon)^2}{d_p^2 \varepsilon^3} + k_2 \frac{\rho v^2 (1 - \varepsilon)}{d_p \varepsilon^3} \quad \text{Eq. 6.6}$$

where ΔP is the pressure drop across the bed, L is the bed height, μ is the fluid viscosity, v is the superficial velocity, ε is the dimensionless void fraction defined as the volume of void space over the total volume of the packed bed, d_p is the particle diameter, and ρ is the fluid density. For mono-spherical particles, d_p is simply the diameter of the particles while for multisized mixtures, d_p is described as the average diameter of the particles (Eq. 6.7).

$$d_p = \frac{100}{\sum_i \frac{m_i}{d_{pi}}} \quad \text{Eq. 6.7}$$

where d_{pi} is the mean granule diameter for size fraction i and m_i is the mass percent (wet basis) of granules of size fraction i .

After analysis of a large quantity of experimental data, Ergun concluded that their best fit could be obtained with $k_1 = 150$ and $k_2 = 1.75$. The applicability of the Ergun equation was reviewed by Macdonald et al. (1979) who tuned the two constants respectively to 180 and 1.8 for smooth spherical particles. For rough particles, the constant k_2 could range from 1.8 – 4. However, no roughness criterion was defined. This shows that the

constants k_1 and k_2 can be considered as “tuning factors” to achieve good agreement with measured pressure drops over packed beds.

6.2.2. Numerical approach

An alternative method to reduce the errors in the prediction of void fraction and pressure drop through packed beds is to simulate the structure of a packed bed using DEM. The bed structure is then exported into CFD packages to calculate the pressure drop across the bed (Bai et al., 2009, 2004; Eppinger et al., 2011). This approach involves both a discrete phase (particles) and a continuum phase (air), and is made possible because of the improvement in computational resources through optimization of the hardware and the software and parallelisation of computers using High Performance Clusters (HPC) or Graphics Processing Unit (GPU) (Marigo and Stitt, 2015; Thakur et al., 2016).

The simulation of fluid flow in porous media has shown disagreement regarding the transition to turbulent flow regimes (Chauveteau and Thirriot, 1967; Dudgeon, 1966; Dybbs and Edwards, 1984; Schneebeli, 1955; Wright, 1968). The Reynolds number is commonly used to indicate the transition from laminar to turbulent flow. It indicates the relative importance between the inertia forces acting on a fluid and viscous forces. For porous media, the Reynolds number (Re_p) can be expressed by Eq. 6.8:

$$Re_p = \frac{\rho v d_p}{\mu} \quad \text{Eq. 6.8}$$

where ρ is the fluid density, v is the superficial velocity, d_p is the particle diameter and μ is the fluid viscosity.

Most researchers have agreed that the transition to turbulence in porous media takes place at Reynolds numbers much lower than in pipes (Chauveteau and Thirriot, 1967; Dudgeon, 1966; Dybbs and Edwards, 1984; Schneebeli, 1955; Wright, 1968). At low Reynolds number ($Re_p < 2$), the streamlines are fixed and the fluid flow is described

by a laminar regime where Darcy's law is applicable. Dybbs and Edwards (1984) established that a highly unsteady and chaotic flow regime appears for Reynolds numbers more than 300. Chauveteau and Thirriot (1967) found the turbulence starts appearing in porous media at Re_p of 75. The turbulence can fully cover the flow when Re_p reaches 180. Wright (1968), Dudgeon (1966) and Schneebeli (1955) reported that the onset of turbulence can be observed at Re_p ranging between 60 and 150. It is clear that the distinction between laminar, transitional and turbulent regimes is still a challenge in porous media and packed beds.

6.2.2.1. Discrete Element Method (DEM)

DEM simulation is described as an important tool for the study of the behaviour of granular matter. It was originally developed for analysis of problems in rock and soil mechanics (Cundall, 1987, 1971; Cundall and Strack, 1979). The philosophy behind the DEM simulation is to construct a realistic 3D representation of the complicated internal structure of the granular packing. DEM is an explicit numerical scheme, which numerically computes the dynamic and static behaviour of an assembly of discrete particles based on interactions with surrounding particles and boundaries (Cundall, 1987, 1971; Cundall and Strack, 1979). In general, the discrete element can be of various shapes and size distributions that require to be considered into the model. Rocky DEM was used in the simulation of the packed bed, whereby more groups of particles (with different properties) could be implemented into the model, however, only spherical particles (mono and bi-sized) were considered for validation purpose of the model.

The application of DEM in particulate systems usually focuses on tracking the motion of each particle and contact forces between impacting particles. These forces are calculated based on the interaction between particles and the physical properties of the entities, including the hardness of particles (represented by a spring) and the particle energy dissipation (expressed as a dampener or dashpot). The hardness of the particle is proportional to the Young's modulus, while the dashpot is related to the coefficient of restitution. The friction between entities is defined with a Coulombic type of friction and implemented with a friction factor (Cundall, 1987, 1971; Cundall and

Strack, 1979). In DEM simulations, the most important particle forces that can be modelled are recoil, gravity and friction. The motion of each particle can then be incremented by integrating the Newton equations (Eq. 6.9 and Eq. 6.10) for translational and rotational motion over the duration of a time step.

- Translational motion

$$m_i \frac{dv_i}{dt} = F_i = F_{ci} + m_i g \quad \text{Eq. 6.9}$$

where m_i and v_i represent the mass and the velocity of a particle i respectively. F_i is the total force acting on the particle, and composed of contact forces (F_{ci}) due to the interactions with its environment (other particles and walls) and the gravitational force ($m_i g$).

- Rotational motion

$$I_i \frac{dw_i}{dt} = T_i \quad \text{Eq. 6.10}$$

where I_i and w_i are the moment of inertia and the angular velocity of the particle i . T_i is the torque arising from the tangential components of the contact forces.

6.2.2.2. Computational Fluid Dynamics (CFD)

Computational fluid dynamics is a computer-aided simulation that uses numerical methods and algorithms to solve and analyse problems related to fluid flows (Ansys, 2012; Bear, 1972; Patankar, 1980). The application of CFD has recently increased and has proven to be an alternative to empirical and experimental methods to analyse complex geometry involving fluid flow (Baker and Tabor, 2010; Hekkala et al., 2004; Nijemeisland and Dixon, 2004, 2001; Zhao and Shan, 2013).

The pressure profiles through porous media are often obtained from the solution of the conservation of laws, namely the continuity equation (conservation of mass) and Navier–Stokes equations (conservation of momentum). In this study, the effective

volume occupied by the discrete phase is introduced into the Navier-Stokes equations as the effective volumetric source term to account for momentum exchange with particles. Furthermore, all locally volume-averaged quantities over a characteristic volume can be selected at least an order of magnitude larger than the particle volume (Anderson and Jackson, 1967; Pepiot and Desjardins, 2012). For an incompressible flow through porous media, the governing equations include the porosity and are given by Eq. 6.11 and Eq. 6.12:

Conservation of momentum:

$$\rho \left(\frac{\partial v}{\varepsilon \partial t} + \frac{1}{\varepsilon^2} (v \cdot \nabla v) \right) = -\nabla p + \mu \nabla^2 v + \rho g + F^T \quad \text{Eq. 6.11}$$

where ρ is the fluid density, ε is the void fraction, v is the superficial velocity, p is the fluid pressure, μ is the fluid viscosity and g is the gravitational acceleration. F^T is the interphase momentum transfer term between the particles and the fluid. It represents model-dependent source terms such as particle momentum terms and fluid-particle interaction forces.

Conservation of mass:

$$\frac{\partial(\rho\varepsilon)}{\partial t} + (\nabla \cdot \rho\varepsilon v) = 0 \quad \text{Eq. 6.12}$$

where ρ is the fluid density, ε is the void fraction and v is the superficial velocity.

DEM-CFD coupling is achieved through the momentum transfer between particles and fluid phase. The interaction forces between the two phases may either be of hydrostatic source (buoyancy) or of hydrodynamic source (drag force, the virtual mass force and the lift force) (Di Felice, 1994; Gidaspow, 1994; Gidaspow et al., 1992; Ricklick and Baran, 2014; Rocky DEM, 2016a). In this study, the drag force F^d was considered as the dominant interaction forces. The drag exerted by a single particle on the fluid phase is given by Eq. 6.13:

$$F^d = \frac{1}{2} \rho C_d A_p |v - u|(v - u) \quad \text{Eq. 6.13}$$

where ρ is the fluid density, C_d is the drag coefficient, A_p , is projected area of particle, v is velocity of fluid and u is velocity of particle. For densely distributed solid particles, Gidaspow et al. (1992) proposed a correlation for C_d calculations (Eq. 6.14). It represents a single drag law that is a connection between (Wen and Yu, 1966) and (Ergun, 1952) correlations. This law can be apply over a broader range of solids volume fraction. Additionally, the drag coefficient is available to the user as a built in field function in DEM-CFD model (Rocky DEM, 2016a).

$$C_d = \begin{cases} \frac{24}{\alpha_f Re_p} \left[1 + 0.15 (\alpha_f Re_p)^{0.687} \right] \alpha_f^{-1.65} & \alpha_f Re_p < 1000; \alpha_f > 0.8 \\ 0.44 \alpha_f^{-1.65} & \alpha_f Re_p \geq 1000; \alpha_f > 0.8 \\ 200 \frac{\alpha_s}{\alpha_f \varphi^2 Re_p} + \frac{7}{3\varphi} & \alpha_f \leq 0.8 \end{cases} \quad \text{Eq. 6.14}$$

where α_f is fluid mass percentage, α_s is the particles mass percentage, φ is the particle sphericity and Re_p is the Reynolds number of the particle.

In this study, a one-way DEM-CFD coupling was used to calculate the pressure drop through a packed bed. Because of the relatively large number of particles, one-way coupling was suitable for particles affecting airflow, but airflow not affecting the particles. Rocky DEM 2.39 was used for simulation of particles, while ANSYS Fluent CFD 14.5 was used for the airflow simulations. The first step was to prepare a Fluent mesh before DEM simulation. The file was imported in DEM via boundaries import. Once the boundaries were imported, the particles (glass beads) were dropped into a column until a steady state was reached. For simulation of airflow (pressure drop), the imported values of bed porosity were used directly in the Fluent porous media model.

The values of cell averaged sizes were used to generate exchange momentum source UDFs that allows the coupling (Rocky DEM, 2012).

6.3. Experimental procedure

6.3.1. Characterisation of glass beads

Glass beads with diameters of 3, 4 and 6 mm (Promak Chemicals) were used in this study. The diameter of 30 beads of each group was measured with a digital calliper. The average diameters for each group of glass beads are listed in Table 6.1. The bulk densities of the glass beads were measured by randomly filling a cylindrical flask (60 mm diameter) with a specific mass of glass beads and measuring the volume. The skeleton density was measured using a helium pycnometer (Model-AccuPyc II 1340 Micromeritics). The void fraction of the glass beads was then calculated by the following equation (Eq. 6.15):

$$\text{Bed void fraction} = 1 - \frac{\text{bulk density}}{\text{skeleton density}} \quad \text{Eq. 6.15}$$

Table 6.1. Measured properties of glass beads of different sizes

Bead size (mm)	Diameter ratio (D/d _p)*	Bulk density (kgm ⁻³)	Apparent density (kgm ⁻³)	Diameter (mm)		Bed void fraction	
				Average	Standard deviation	Average	Standard deviation
3	20	1.54	2.53	3.00	0.03	0.392	0.004
4	15	1.52	2.56	3.94	0.05	0.406	0.004
6	10	1.51	2.56	5.94	0.09	0.410	0.002

* D: Diameter of the cylindrical flask

* d_p: Particle (glass bead) diameter

The coefficient of static friction is also important to characterize the flow behaviour of glass beads. This coefficient was experimentally determined by forming granular piles where glass beads were loosely poured into a tube and lifted to allow the granular material to a pile under gravitational forces. The angle of repose is described as the angle that the accumulated material forms with the horizontal (Figure 6.2). The tangent of the angle of repose has been found to be equal to internal (static) friction of the granular material. The experimental static friction coefficients are listed in Table 6.2. It can be observed that the measured angle of repose decreases with the size of glass beads.



Figure 6.2. Experimental test of pile formation
(3 mm diameter glass beads, 150 mm diameter of the plate)

Table 6.2. Measured angles of repose and coefficients of static friction of different glass bead sizes

Glass bead size (mm)	Angle of repose ($^{\circ}$)		Static friction (-)	
	Average	Standard Deviation	Average	Standard Deviation
3	21.40	0.58	0.39	0.01
4	18.20	0.58	0.33	0.01
6	16.00	1.16	0.29	0.02

Additionally, the flow characteristics of the glass beads are affected by the coefficient of restitution (*COR*), which is generally a measure of energy loss during a collision.

This coefficient varies between 0 and 1. The two end conditions correspond to perfectly plastic ($COR = 0$) and perfectly elastic impact ($COR = 1$) respectively. The restitution coefficient can be expressed as the square root of the ratio of elastic energy $E_{kin,reb}$ released during the rebound of the particle to the initial kinetic impact energy $E_{kin,imp}$ (Eq. 6.16) (Aryaei et al., 2010; Meriam and Kraige, 2002). The measurement of the restitution coefficient is then reduced to a drop test. A particle is held at a determined height (h) above a flat surface and released with zero initial velocity and rotation. After its impact with the surface, the particle reaches a rebound height (h_{reb}).

$$COR = \sqrt{\frac{E_{kin,reb}}{E_{kin,imp}}} \approx \sqrt{\frac{2gh_{reb}}{2gh}} = \sqrt{\frac{h_{reb}}{h}} \quad \text{Eq. 6.16}$$

In this study, the restitution drop test for each glass bead size was repeated 10 times and average values were used in DEM simulation (Table 6.3). The height before the drop was set at 82 mm. The impact surface was a steel flat block with 30 mm thickness. The measured coefficient of restitution decreases with the size of glass beads. The tangential coefficient of restitution was not considered.

Table 6.3. Restitution coefficient of glass beads of different glass bead sizes

Glass bead size (mm)	Mean restitution coefficient	Standard deviation
3	0.77	0.02
4	0.76	0.02
6	0.73	0.01

6.3.2. Numerical simulation procedures

The pressure drop across packed beds was computed by one-way coupling of DEM (Rocky 2.39) with CFD (Fluent 16.1). For each bead size, the model geometry satisfied packing length to bead diameter and tube diameter to bead diameter ratios

of greater than 10. This implied wall effects could be neglected during numerical simulation (Bai et al., 2009, 2004; Dixon, 1988; Eppinger et al., 2011; Furnas, 1931). In this study, DEM simulations were performed in such a manner that the number of generated particles approximately forms the same bed height regardless of the glass bead size. Corresponding tube/particle diameter ratios (D/d_p) for 3, 4 and 6 mm glass bead were respectively 47, 36 and 24, all significantly more than 10, and hence the wall effects were neglected. An unstructured mesh composed of tetrahedral elements was first created in Fluent CFD and imported in Rocky DEM. The packed bed was then simulated by simulating a stream of particles (glass beads) pouring into a column from a specified height. The filling process with glass beads of 3 mm in diameter is shown in Figure 6.3. For binary mixtures, the formation of a packed bed by Rocky DEM simulation was performed by assigning dumping velocities to fine and coarse particles, depending on their respective mass percentages so that each group of particles could be generated accordingly. The Rocky DEM simulations were performed using the parameters listed in Table 6.1 and Table 6.2.

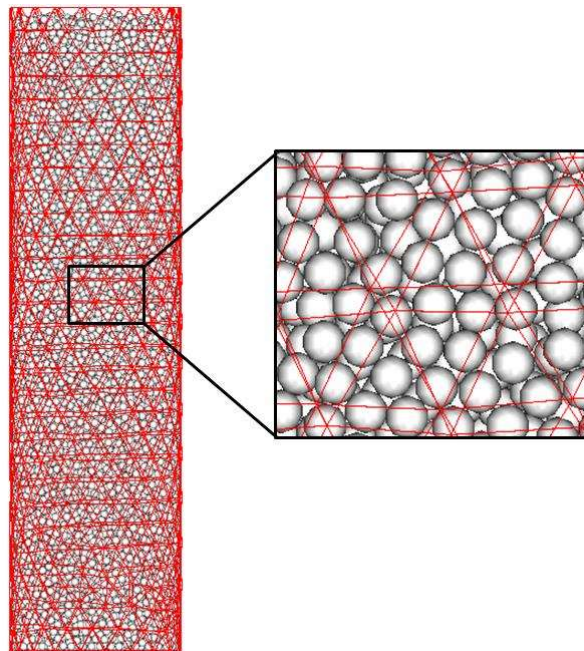


Figure 6.3. Schematic representation of the simulation model for packing of 3 mm glass beads into a permeameter

Once the packed bed was formed, meshed Rocky DEM simulated packing geometry was exported into CFD via a compiled file containing the profiles of porosity and momentum terms. Ansys Fluent 16.1 was the computational code used to solve the continuity and Navier - Stokes equations using a finite volume method. As the Reynolds numbers for 3 mm, 4 mm and 6 mm glass beads (220, 354 and 627 respectively) fell in the turbulence regime, a realizable k- ϵ turbulence model was selected to simulate the flow field through the modelled packed bed. SIMPLE (Semi-Implicit Methods for Pressure Linked Equations) scheme was selected for the computational procedure. Finally, the results of the pressure drop across the packing were retrieved from the Fluent solver.

The modelled packed bed was equally extended with empty sections at each end of the packed bed. This is necessary in order to minimize the effect of boundary conditions at the inlet and outlet of the tube in the CFD simulations. The empty sections allow flow to naturally develop as it is approaching or leaving the packed bed. The mass flow rate specified at the inlet is internally converted into a uniform velocity at the inlet boundary, thus eliminating possible end effects. The inlet velocity for 3, 4 and 6 mm glass beads is 1.41, 1.63 and 2.01 ms⁻¹ to reach the pressure drop of 9806 Pa. It is clear that the lower particle size, the lower the porosity and the lower the superficial velocity. In this study, the length of the empty sections was designed to be at least one tube diameter (Bai et al., 2009, 2004).

6.3.3. Simulation of angle of repose

There are several numerical techniques that have been developed to calibrate the static friction angle for DEM simulation (Rocky DEM, 2012; Zhou et al., 2001; Zhu et al., 2008). For the simulation of the angle of repose, glass beads were released from a fixed drop height into a tube seated on a plate. The tube was afterwards lifted at a velocity of 1mm/s to let glass beads form a pile (Figure 6.4). In this investigation, experimental parameters of glass beads (size, density and static friction) were used. The rolling friction coefficient was kept to one hundredth of the coefficient of static friction (Zhu and Yu, 2003). The elastic stiffness was set to a default value of 10⁷ Pa.

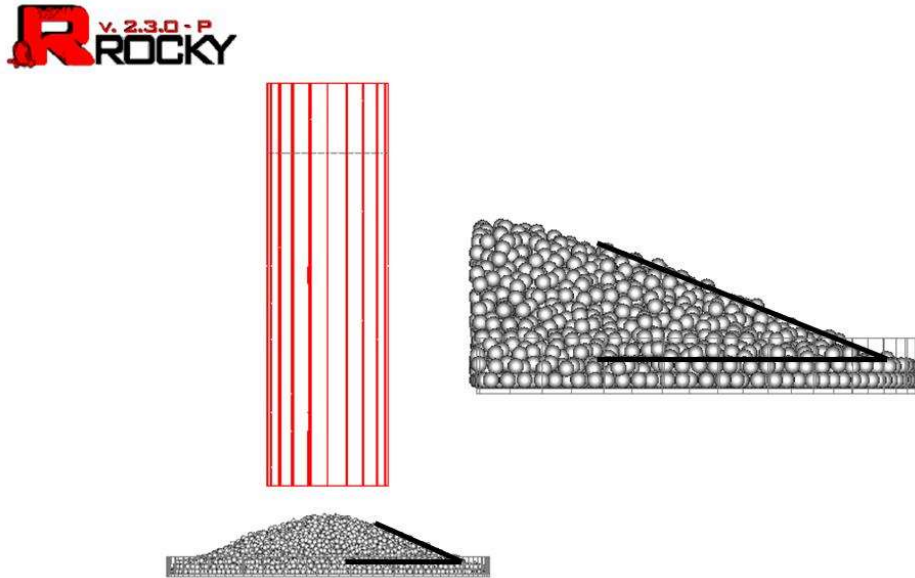


Figure 6.4. Rocky DEM simulation of pile formation test after release (3 mm diameter beads, 60 mm diameter of the tube, 150 mm diameter of the plate)

6.4. Results and discussion

6.4.1. Comparison between measured and simulated static friction of glass beads

Simulated and experimental static friction coefficients for different sizes of glass beads are shown in Figure 6.5. It can be seen that the simulation angle of repose (static friction) decreases with glass bead size. A similar observation was made when the static friction coefficient was determined experimentally. Good agreement between the simulated and experimental static friction values were obtained for different sizes of glass beads. The deviations fell within $\pm 10\%$.

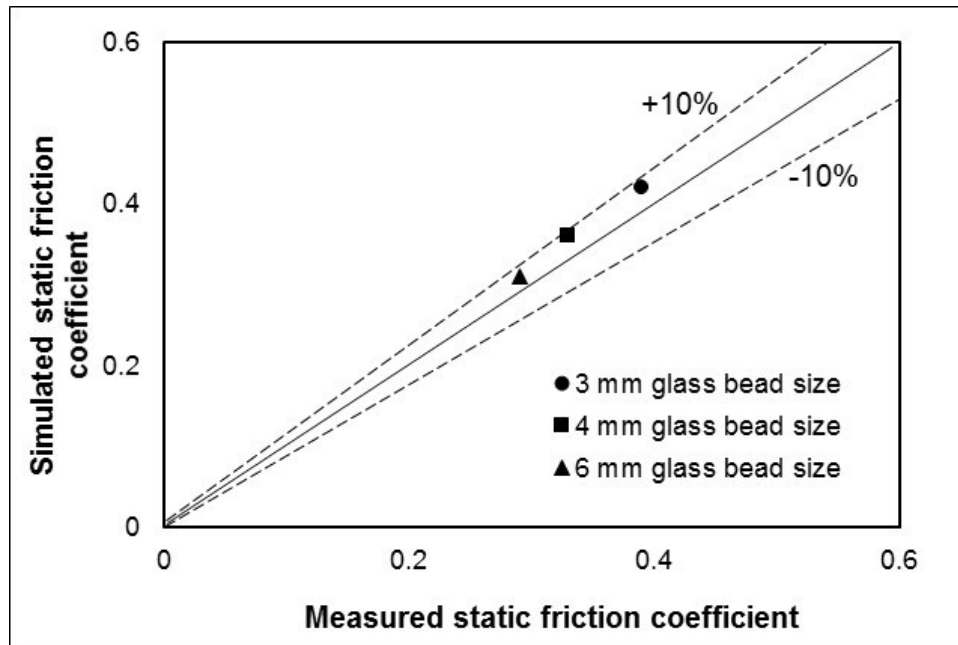


Figure 6.5. Comparison between measured and simulated coefficients of static friction

6.4.2. Predicted void fractions by DEM simulations and mathematical correlations

In the simulation of packed beds, the interactions between glass beads were represented by the properties listed in Table 6.4. For each simulation test, the void fraction was calculated by the Rocky DEM model by comparing the volume of the total number of particles generated during the simulation and the corresponding volume of the cylinder (tube) that contains the packed bed. The void fractions obtained by different methods are listed in Table 6.5. A comparison between the simulated, calculated and measured void fractions are also shown in Table 6.5 and Figure 6.6. The absolute deviations are 0.73 - 1.02% for DEM model, 0.24 - 2.81% for Dixon model and 1.28 - 3.45% for Furnas model. This shows good agreement between the predicted void fractions and measured void fraction data for 3 mm, 4 mm and 6 mm bead diameter. All deviations are within $\pm 10\%$ (Figure 6.6). Additionally it can be seen that very good correlations are obtained when comparing the void fractions predicted by DEM model and experimental data.

Table 6.4. Interaction properties of glass beads

Properties	Unit	Values		
		3 mm glass bead	4 mm glass bead	6 mm glass bead
Coefficient of static friction	(-)	0.42	0.36	0.31
Coefficient of rolling friction	(-)	0.42×10^{-2}	0.36×10^{-2}	0.31×10^{-2}
Coefficient of restitution	(-)	0.77	0.76	0.73
Elastic stiffness (default)	(-)	10^7 Pa	10^7 Pa	10^7 Pa

Table 6.5. Void fractions of the packed beds

Methods or equations	Glass bead packed bed					
	3 mm		4 mm		6mm	
	Void fraction	Absolute deviation	Void fraction	Absolute deviation	Void fraction	Absolute deviation
Rocky DEM model	0.396	1.02%	0.407	0.25%	0.413	0.73%
Experimental	0.392	-	0.406	-	0.410	-
Dixon's equation	0.403	2.81%	0.405	0.25%	0.409	0.24%
Furnas's equation	0.387	1.28%	0.392	3.45%	0.404	1.46%

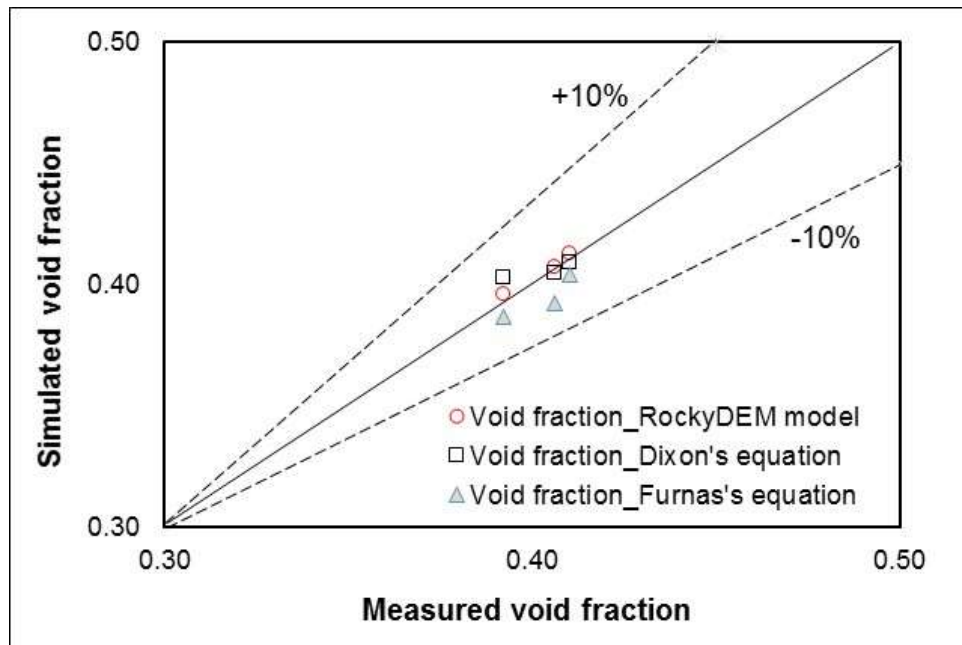


Figure 6.6. Comparison of predicted and measured void fractions. Rocky DEM, Dixon's and Furnas's equation used to predict void fraction

For binary mixtures, the mass percentage of large and small glass beads was varied between 0% and 100% in increments of 25% (Table 6.6). Different mass percentages of glass beads with diameters of 3 and 6 mm were simultaneously poured into the permeameter. In the simulation of void fraction, the two glass bead sizes were dropped into the simulated permeameter at relative velocities that were calculated according to the fraction ratio of 3 mm glass beads to 6 mm glass beads. The predicted void fractions of the binary mixtures were then compared with void fractions calculated by the Zheng et al. (1995) and the Furnas equations (Figure 6.7). The simulation of void fraction is in agreement with previous work, where size variation can allow particles to form a denser packing than monosized spheres (Williams and Philipse, 2003). The void fractions of the binary mixtures are lower than those of monodisperse packed beds.

Table 6.6 Calculated and predicted void fractions in binary mixtures of 3 mm and 6 mm glass beads

Mass percentage of large glass beads	0%	25%	50%	$X_L = 70\%$	75%	100%
Calculated porosity by Zheng's model	0.387	0.399	0.380	-	0.380	0.404
Predicted porosity by Rocky DEM	0.396	0.388	0.377	-	0.378	0.413
Calculated porosity by Furnas's model	0.387	-	-	0.157	-	0.404

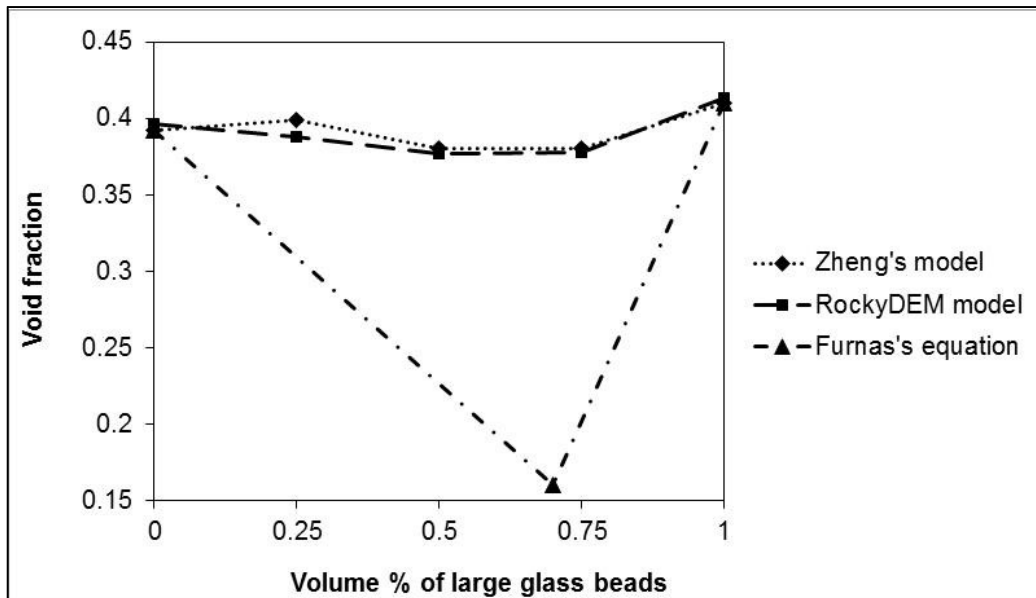


Figure 6.7. Comparison of predicted and calculated void fractions of beds randomly packed with binary mixtures of 3 mm and 6 mm glass beads

From Figure 6.7, the void ratio starts to decrease as the mass percentage of 6 mm glass beads is increasing. The addition of larger beads results in replacement of a group of smaller beads by one larger bead. Some voids (pores) in the binary mixture

are progressively occupied by larger beads. At approximately 65-73% of 6 mm beads, the void ratio starts to increase again. The volume of voids formed by packing of larger glass beads is greater than that of the smaller beads. It can also be seen that the Furnas equation under-predicts void fractions in binary mixtures. Close agreement between predicted values and void fractions calculated from Zheng's equation was achieved, with deviations between 0 and 2%.

6.4.3. Influence of mesh size on pressure drop

The specification of mesh size is an important part in CFD, especially in complex geometries such as those found in packed beds. Although the mesh size must be fine to describe enough detail of the flow through the bed, it must also be coarse enough to complete the simulation in reasonable time. To study the effect of mesh size on the pressure drops over a packed bed of glass beads, several numerical simulations with different mesh sizes were conducted while the particle size was held constant for each type of glass bead. A series of mesh sizes (6 mm, 12 mm, 24 mm, 36 mm and 48 mm) were selected in such a way that several particles could fit inside one CFD mesh element.

In the one-way Rocky DEM – CFD coupling, a realizable $k-\epsilon$ model and SIMPLE scheme were adopted for turbulence, velocity and pressure drop calculations. A uniform inlet velocity for packed bed constituted from 3, 4 and 6 mm glass beads was set to 1.41, 1.63 and 2.01 ms^{-1} respectively. The results showed that the pressure drop through the packed beds decreases with increasing the mesh size (Figure 6.8). It can also be seen that the pressure drop is almost independent of mesh size for larger mesh size (> 24 mm). These results did not support the common criteria where the mesh size is smaller than the particle size (Bai et al., 2009, 2004; Eppinger et al., 2011; Nemeč and Levec, 2005). An unstructured mesh (Tetrahedral) of 36 and/or 48 mm mesh size was therefore chosen for further simulations of the pressure drop.

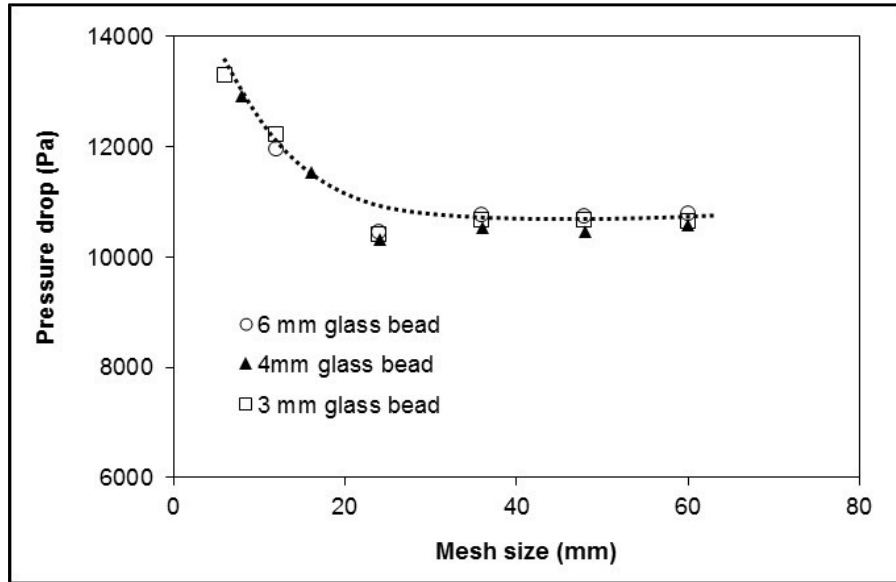


Figure 6.8. Effect of mesh size on pressure drop through the glass beads

The selected mesh sizes (36 mm and 48 mm) are in agreement with the approach based on the point-particle method (Anderson and Jackson, 1967; Pepiot and Desjardins, 2012; Vollmari et al., 2015; Zhang et al., 2008). These authors have established that the smallest local volume should be set to at least 10 times the particle volume. All variables can consequently be expected to be locally averaged-quantities over the smallest possible structure characterized by the finest mesh size. For a spherical particle, the finest mesh size was determined to be at least $1.74d_p$ (Anderson and Jackson, 1967; Pepiot and Desjardins, 2012; Zhang et al., 2008).

Another way to show the mesh independence was shown in Figure 6.9. Here, the deviation between the simulated and measured pressure drop is plotted against the mesh size. It can be seen that the deviation is almost constant from 36 mm mesh size and within $\pm 10\%$. It can be seen that this method allows large mesh size while maintaining good accuracy.

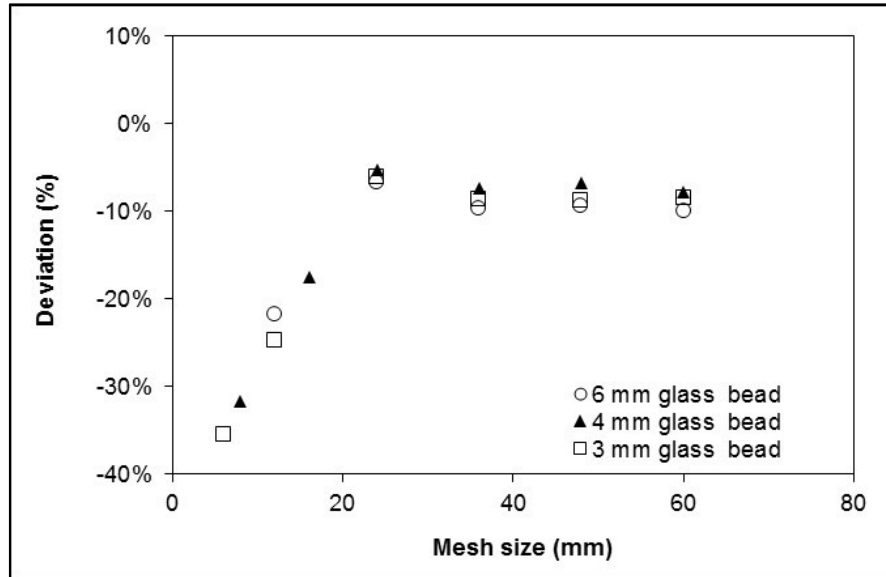


Figure 6.9. Variation in deviation (error) between the simulated and measured pressure drop with mesh size.

6.4.4. CFD Model Validation for monosized glass beads

The aim of this section is to compare the measured pressure drop through packed beds with the predicted data using Rocky DEM – CFD coupling. Particle and gas properties as well as experimental initial conditions were used in the simulation of the pressure drop through the mono-sized spheres. A mesh size of 36 mm was selected to perform the validation of CFD simulations of the three different sizes of glass beads. A comparison between the experimental pressure drops and the simulated pressure drops through beds of mono-sized glass beads is shown in Table 6.7. The deviations between the measured and predicted pressure drops are within $\pm 10\%$, which is acceptable in terms of accuracy of simulated or predicted pressure drops through packed beds (Bai et al., 2009, 2004). It can also be seen that the simulation over-predicts the pressure drops across all the examined mono-sized beds. The top surface of the DEM packed bed was not well-levelled. To measure the pressure drop at height of 535 mm (target value), the packed bed was extended of 0.2 - 3% above the target height. This resulted in an over-prediction of the pressure drop using DEM-CFD model.

Table 6.7. Comparison between simulated and measured pressure drops for monosized glass beads

Size of glass bead (mm)	Size ratio of mesh to glass bead	Predicted pressure drop (Pa)	Measured pressure drop (Pa)	Deviation (%)
36 mm mesh size				
3	12	10657	9806	- 8.68
4	9	10526	9806	- 7.34
6	6	10760	9806	- 9.73
48 mm mesh size				
3	16	10658	9806	- 8.70
4	12	10461	9806	- 6.68
6	8	10725	9806	- 9.38

6.4.5. Pressure drop through binary mixtures

The experimental and simulated pressure drops through binary mixtures were determined using a permeameter and Rocky DEM – CFD coupling respectively. For numerical simulations, the particle properties (density, coefficient of static friction, coefficient of restitution and stiffness) of 3 mm and 6 mm glass bead size are listed in Table 6.1 and Table 6.4. The mesh size was set to 36 mm and 48 mm to infer the effect of mesh size on pressure drop and deviation from experimental data. The Realizable k- ϵ model and SIMPLE scheme were chosen for the pressure velocity. The velocity at the inlet for binary mixtures with 25%, 50% and 75% of 6 mm glass beads was respectively set to 1.30, 1.34 and 1.44 ms⁻¹ to reach the pressure drop of 9806 Pa. The computational predictions for pressure drop were compared to measured pressure drops through the packed beds. The errors between the experimental data (measured pressure drops) and predictions are presented in Table 6.8.

Table 6.8. Comparison of measured pressure drop and predicted pressure drop for binary mixtures of 3 mm and 6 mm glass beads

Mass percentage of 6mm glass beads	Predicted pressure drop (Pa)	Measured pressure drop (Pa)	Deviation (%)
Mesh size = 36 mm			
25	8975	9806	8.48
50	8996	9806	8.26
75	9414	9806	4.00
Mesh size = 48 mm			
25	8995	9806	8.27
50	8922	9806	9.01
75	9505	9806	3.07

Good agreement between the predicted pressure drop of different packed beds and the measured pressure drop data was achieved for both selected mesh sizes of 36 and 48 mm (Table 6.8). Deviations between the predicted and measured pressure drops through the packed beds lie within 10%, which is acceptable for errors between simulations and experimental data (Bai et al., 2009, 2004). The results obtained with 36 mm and 48 mm mesh sizes were comparable (Figure 6.10).

The simulation underestimated the pressure drop through binary mixtures. This may be explained by the non-homogeneity of the spatial distribution of particles. The packing of a binary mixture generally creates zones with different void fractions due to a randomly particle distribution. In a homogeneous packed bed, the pathway of a fluid is shorter than that in a heterogeneous bed structure (Mota et al., 2001). In DEM packed bed, the spatial distribution of particles is uniform, resulting in an easy path of

airflow and thus less resistance. Consequently, the pressure drop will be lower than the experimental pressure drop through particles that are randomly distributed.

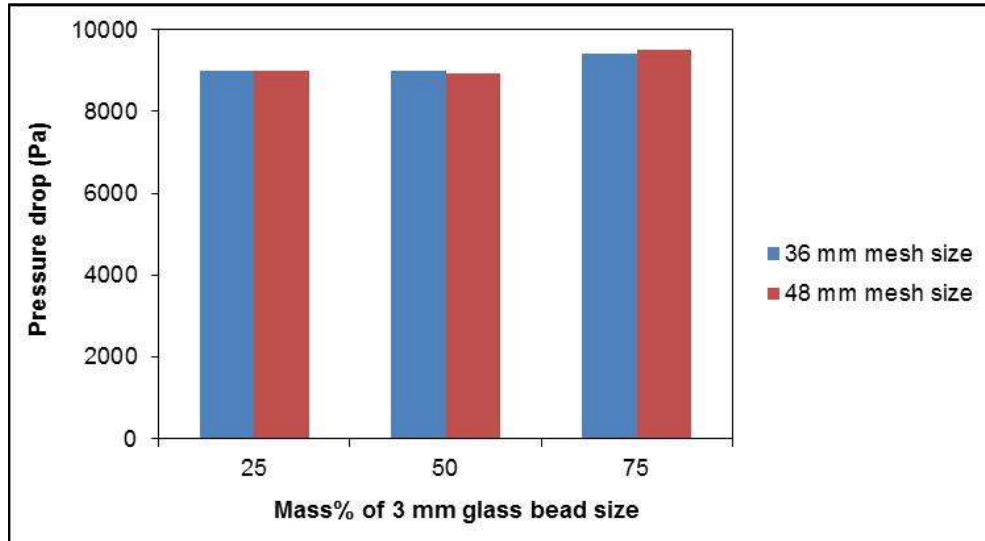


Figure 6.10. Comparison between pressure drops obtained with 36 mm and 48 mm mesh size for binary mixtures of glass beads

6.4.6. Scale down of the packed bed of glass beads

The scale down of packed beds is performed in order to reduce the computing time. In this study, the pilot-scale of packed beds constituted from glass beads was scaled down by setting the column-to-glass bead diameter ratio (D/d_p) and glass bead diameter-to-packing height ratio (d_p/H) to be larger than 10 and less than 0.05 respectively. Under these circumstances, it is expected that the pressure drop will not be affected by the porosity distribution or structure of the packed bed (Zou and Yu, 1995). The new packing was then reduced to a column packing with a diameter of 70 mm and height of 200 mm. For the reduced scale, the column-to-glass bead diameter ratio and glass bead diameter-to-packing height ratio are shown in Table 6.9. The pressure drop across the reduced packed beds was then simulated using Rocky DEM-CFD coupling with similar parameters as those used in the full-scale simulation. Good agreement was obtained between the simulated pressure drop across the reduced and full scale packed columns (Table 6.10). The deviations between the simulated pressure drops are within 3%.

Table 6.9. Column-to-glass bead diameter ratio and glass bead diameter-to-packing height ratio of full and reduced scale packing.

Packed bed	D/d _p		d _p /H	
	Full scale	Reduced scale	Full scale	Reduce scale
3 mm glass bead	47.33	23.33	0.01	0.02
4 mm glass bead	35.50	17.50	0.01	0.02
6 mm glass bead	23.67	11.67	0.01	0.03

Table 6.10. Deviation of the simulated pressure drop across full and reduced scale packed columns

Packed bed	Pressure drop (Pa/m)		Deviation (%)
	Full scale	Reduced scale	
Monosize mixture			
3 mm glass bead	19919	19665	1.28
4 mm glass bead	19674	19715	-0.20
6 mm glass bead	20112	19865	1.23
Binary mixture			
75% 3 mm, 25% 6 mm glass bead	16775	16470	1.82
50% 3 mm, 50% 6 mm glass bead	16814	17000	-1.10
25% 3 mm, 75% 6mm glass bead	17596	17140	2.59

6.4.7. Comparison with Ergun's equation

The Ergun equation was used to determine the pressure drop for flow over spherical particles (Ergun, 1952; Niven, 2002). The pressure drop was also calculated using MacDonald's equation for smooth particles (Macdonald et al., 1979). The measured pressure drops over different glass beads was compared to the predictions from the Ergun and MacDonald equations (Table 6.11). The measured pressure drop was set to 9806 Pa (1000 mmH₂O).

Table 6.11. Deviations between measured and predicted pressure drop using Ergun's equation and MacDonald's equation

	Ergun's equation		MacDonald's equation	
	Pressure drop (Pa)	Deviation (%)	Pressure drop (Pa)	Deviation (%)
Mono-size mixture				
3 mm glass bead	7368	24.86	7821	20.24
4 mm glass bead	6328	35.47	6651	32.17
6 mm glass bead	5600	42.90	5831	40.53
Binary mixture				
75% 3 mm, 25% 6 mm glass bead	5124	47.75	5421	44.71
50% 3 mm, 50% 6 mm glass bead	5592	42.98	5906	39.77
25% 3mm, 75% 6mm glass bead	5136	47.62	5397	44.96

Comparing the measured and calculated values using the Ergun and MacDonald equations for pressure drops through packed beds of glass beads, clear discrepancies

could be seen. The calculated pressure drop through glass beads deviated considerably from the measured pressure drop. The deviations ranged from 20% to 48%. Higher deviations were obtained with the Ergun equation. This shows that the Ergun equation is not universally applicable for calculation of the pressure drop (Ergun, 1952; Hicks, 1970; Macdonald et al., 1979; Nemeč and Levec, 2005; Winterberg and Tsotsas, 2000). The two constants must be tuned to fit the experimental pressure drops through beds of glass beads. The predictions using Ergun's equation were proven to be less accurate in determining the pressure drop across multi-sized particles (Luckos and Bunt, 2011).

6.5. Conclusions

This study was conducted in order to validate the simulated pressure drop through a randomly packed bed of glass beads in a permeameter using Rocky DEM – CFD Fluent coupling. Experimental tests and simulations were performed for beds constituted from three different mono-sized glass beads (3, 4 and 6 mm in diameter) and three different binary mixtures of 3 mm diameter glass beads containing 25, 50 and 75% of 6 mm diameter glass beads respectively. The point-particle method was used to determine the mesh size.

DEM simulations predicted void fraction values that compare with measured void fraction data of mono-sized and bi-sized glass beads. Pressure drop values obtained from the CFD model were validated against the experimental data. The agreement between the simulations and the experimental tests is within 10% for selected mesh sizes of 36 and 48 mm. For mesh sizes larger than the glass bead size, the mesh size had no significant effect on the pressure drop. CFD simulations over predicted the pressure drops through mono-sized glass beads while under predicted the pressure drop for binary mixtures. The prediction of pressure drop over the pilot-scale packed bed per unit length showed a good agreement with the data calculated from the reduced scale packed bed.

Applying the Ergun and MacDonald equations to the evaluation of pressure drop across the beds of glass beads, resulted in significant deviations from the measured pressure drops. The Ergun and MacDonald constants could not correctly predict the pressure drop through glass beads using a permeameter designed for the measurement of green granule permeability.

7. DEM – CFD coupling simulation of the pressure drop through a packed bed of iron ore granules

7.1. Introduction

The pressure drop across a granulated mixture is one of the most important parameters that affect the productivity of the sintering process. During the sintering process, the iron ore granules are agglomerated by heat exchange and partial fusion that are driven by suction of hot gas flow through the packed bed of moist granules. It was established that the lower the pressure drop over sinter bed, the higher the permeability of the sinter bed and the higher the productivity of the sintering process (Ball et al., 1973; Ellis et al., 2007; Formoso et al., 2003; Khosa and Manuel, 2007; Litster and Waters, 1988; Loo et al., 1992; Voice et al., 1953).

The measurement of the pressure drop through green granules before ignition is commonly carried out experimentally. This technique remains an “empirical art” in most sinter plants (Section 3.1.4). This may be due to the complexity of the mixtures consisting of moist deformable granules with randomly distributed irregular shapes, structures and sizes. These parameters were known to significantly affect the void fraction, angle of repose and permeability of the packed bed (Carstensen and Chan, 1976; Hinkley et al., 1994b; Kasai et al., 1989; Rankin et al., 1983; Rankin and Roller, 1985; Van Burkalow, 1945; Wooten, 1998; Zhou et al., 1999). Zhou et al. (2017) studied the pressure drop along the sinter bed during a pilot - scale - sintering process. CFD simulations were performed based on the reconstructed real geometry of sinter cakes by X-ray micro-tomography. For simplicity, a sample of 30*30*30 mm³ was excavated from the sintered zone in the centre region of the sinter cake, where the melt is supposed to solidify and no changes in structure occur. To obtain reliable values of the pressure drop (permeability), it was appropriate to simulate a large size of the sinter cake, which could unfortunately result in huge computational costs. Mitterlehner et al. (2004) predicted the fluid flow through a granulated material using Ergun equation. Ergun constants were adjusted by the method of least square fit and a very good agreement was obtained between the measured and calculated pressure drops.

The first step to study the simulation of the flow behaviour in packed beds is commonly to build a virtual packed bed. The particle properties such as size distribution, shape and contact forces between particles are implemented in a DEM model in order to accurately simulate the packed beds. Mohanty et al. (2016) studied the flow profile in packed beds using DEM simulation. They used mono-sized spherical particles to generate the packed bed and contact forces based on the Hertzian contact theory. Thornton et al. (2012) used a DEM model to investigate the particle size segregation in the chute-flow simulation for bi-sized systems. They reported that packed beds show slight asymmetry during segregation, whereby the large particles form a thick pure phase at the top while the small particles appeared in a thin pure layer at the base of the packed bed. Barrios et al. (2013) studied the bulk flow of iron ore pellets on the basis of the contact force parameters through DEM simulation of single spherical particles. Ishihara et al. (2013) investigated the collapse of the sinter bed during charging of granules on the sintering machine using a DEM model. They found that the collapse of the sinter bed occurred when the adhesion force coefficient is larger than 0.02 during the simulation. Ishihara et al. (2013) also found that an increase in the adhesion force increases the dynamic angle of repose for uniform and non-uniform granule sizes. This can explain the collapse of a wet and sticky sinter bed. Nakano et al. (2012) studied the size segregation in the feed bed of a sintering machine, using a DEM model. The size segregation was found to increase with a decrease in the chute angle during the charging of the sintering machine. This was in a good agreement with experimental observations.

Although DEM simulations are increasingly used to understand the behaviour of the bulk material, the modelling of realistic systems is a challenge when particle shape and size distributions are involved (Bai et al., 2009, 2004; Eppinger et al., 2011). The simulation time is short for uniform spherical particles and computer requirements are affordable (no need of GPU). The irregularity of granules often cause particles to interlock between each other, which makes the behaviour of non-spherical particles more difficult to model than the spherical particles (Coetzee, 2016; Coetzee and Els, 2009; Taylor et al., 2006). German (1989) reported that packing simulations are too expensive and computer-time consuming when using real shapes of particles. Thomas

and Bray (1999) found that it is too costly to model a huge number of particles, each with its real shape and size. They then proposed a concept of equivalent diameter and shape of particles. This could partially overcome the complexity of irregular packing by assuming that the behaviour of non-spherical particles could be similar to that of spheres with equivalent properties (size, shape, stiffness, coefficient of restitution, angle of repose and adhesion force).

The pressure drop through packed beds is commonly predicted by coupling DEM and CFD. A one-way and two-way coupling model was successfully applied to the calculation of pressure drops through glass beads in a permeameter. Good comparison between the numerical simulations and experimental measurements was achieved (Chapter 6 and Appendix F).

This chapter describes the extension of the developed DEM-CFD two-way coupling model to the calculation of the pressure drop through a green granule bed. The design of the packing was simulated by the discrete element method (DEM), whereby the size distribution, shape and adhesion force of moist granules were implemented in the simulation. Multiphase flow model was used to simulate the gas flow through the DEM packing. Pressure drop predictions were compared against the experimental data for mixtures with addition of concentrate and micropellets.

7.2. Key parameters of DEM – CFD coupling method

The pressure drop through packed beds is commonly predicted by the Lagrangian – Eulerian coupling approach. The current research used a two-way coupling of DEM (Rocky 3.9) and CFD (Fluent 16.1) to numerically calculate the pressure drop through the sinter bed (Appendix F). The behaviour of the particles was governed by Newton's second law of motion (Cundall and Strack, 1979), while fluid flow was computed by the Navier-Stokes equations (Anderson, 1995; Anderson and Jackson, 1967).

7.2.1. Numerical simulation of packed bed

Previous studies reported that a DEM model can be successfully used to simulate moist granular material and account for inter-particle forces (elastic stiffness, friction and adhesion), size distribution and shape of particles (Cundall and Strack, 1979; Ishihara et al., 2013; Nakano et al., 2012).

Cundall and Strack (1979) used a small overlap (δ) between particles to simulate the elastic deformation of particles (Figure 7.1). This overlap is combined with other physical quantities to understand the behaviour of particles subjected to a variety of loading conditions and determine force-overlapping relations (7.2.1.1).

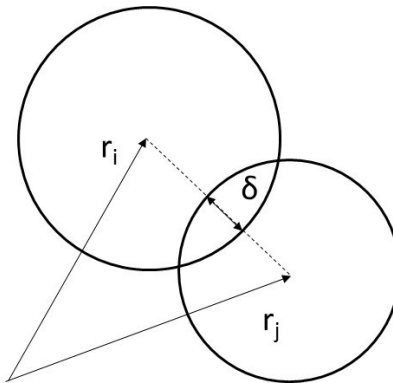


Figure 7.1. Two-particle contact with overlap in normal direction. r_i and r_j are the positions of particles i and j respectively.

Ishihara et al. (2013) investigated the factors that cause the collapse of the sinter bed and size segregation phenomena in the vertical direction of sinter bed at the charging point of raw materials using Discrete Element Method (DEM). An emphasis was put on the adhesion force between granules as one of the factors that contribute to the collapse and size segregation of the sinter bed. The degree of the size segregation in the vertical direction decreased with an increase in the adhesion force of granules. The collapse phenomena of the sinter bed occurred for an adhesion force coefficient larger than 0.02.

Nakano et al. (2012) studied the charging process in iron ore sintering and vertical size segregation in the sinter bed using DEM simulation. It was found that the size segregation in vertical direction increases with a decrease in chute angle. This result was in good agreement with plant data. The plasticity and stiffness of the sinter bed were expressed by a combination of elastic stiffness and rolling friction coefficient.

7.2.1.1. Inter-particle forces

The forces between particles are described as contact and adhesion forces and can be predicted by the soft-sphere collision model of Cundall and Strack (1979), whereby the particles are considered as viscoelastic spheres. There are different models that account for the contact forces and adhesion forces between each pair of particles (Hertz, 1882; Johnson et al., 1971; Mindlin, 1949; Thornton and Ning, 1998). The simple contact force model is the linear spring – dashpot model (Figure 7.2). The spring stiffness (k) and dashpot coefficient (η) are expressed through Young's modulus parameter and coefficient of restitution (ϵ_r) respectively. The friction sliders represent the friction between contact points, which is implemented with a friction factor μ_s (Mindlin, 1949; Sun et al., 2006; Walton, 1994; Walton and Braun, 1993).

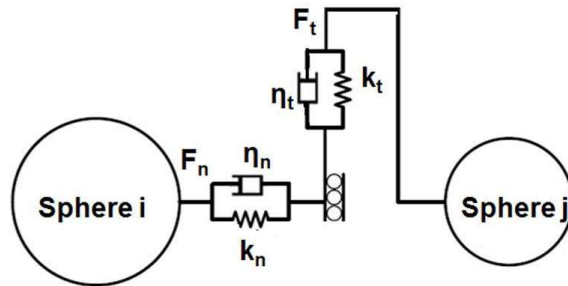


Figure 7.2. Spring dashpot model for contact forces between particles

The normal and tangential forces (F_n and F_t) can then be calculated by the relations (Mindlin, 1949):

$$F_n = k_n \delta_n + 2\beta \sqrt{m_{ij} k_n} v_n \quad \text{Eq. 7.1}$$

$$F_t = \min \left\{ \mu_s F_n, k_t \int v_t dt + \sqrt{m_{ij} k_t v_t} \right\} \quad \text{Eq. 7.2}$$

where $\beta = -\frac{\ln(\epsilon_r)}{\sqrt{\pi^2 + \ln^2(\epsilon_r)}}$ and $m_{ij} = \frac{m_i m_j}{m_i + m_j}$ are the dashpot ratio and reduced mass of particles i and j with masses m_i and m_j respectively, k_n is the normal stiffness, k_t is the tangential stiffness, v_n is the normal velocity and v_t is the tangential velocity. The particles are allowed to overlap and the normal overlap δ_n between two particles is determined by the stiffness (k_n) of the spring in the normal direction. The total tangential force F_t is limited by the Coulomb frictional limit $\mu_s F_n$.

The adhesion forces between particles are implemented in DEM simulations when moist, sticky and deformable particles are involved. These forces cause particles within wet granular materials to adhere together. The application of adhesion forces in a DEM model more closely represents the real forces between wet granules. The adhesion forces between two particles can represent the irreversible contact deformation and be load dependent (Itasca, 2003; Tomas, 2007). To represent the adhesion between iron ore granules, a contact bond model was used in DEM simulation (Ishihara et al., 2013; Jiang et al., 2015; Nakano et al., 2012). The contact bond model is shown in Figure 7.3.

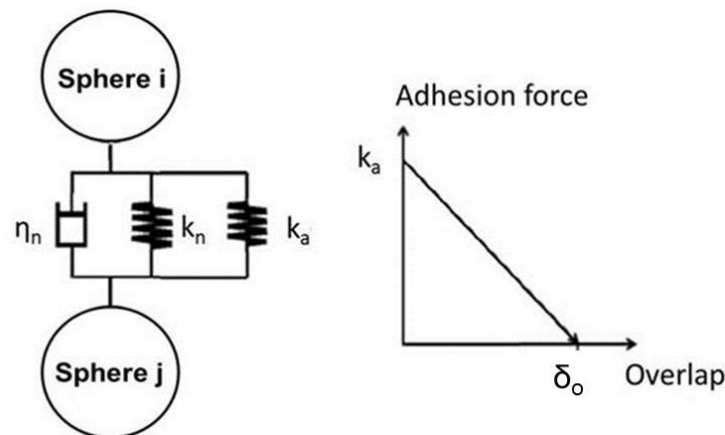


Figure 7.3. Contact bond model for a sticky material

The adhesion force (A_{adh}) between two bonded spherical bodies can be expressed by Eq. 7.3.

$$A_{adh} = k_a(\delta_0 - \delta) \quad \text{Eq. 7.3}$$

where k_a is the adhesive coefficient and δ is the overlap. δ_0 is the overlap when the adhesion force (k_a) equals to 0. The adhesion force reaches its maximum when the two granules touch each other. The model can return to a simple linear spring model if $k_n = k_a$. It is clear that the spring stiffness (k_n) of spheres in contact is not reliant on the adhesion force (k_a) acting between two spheres (Johnson et al., 1971).

In Rocky DEM, the contact and adhesion forces between particles are calculated from different models: elastic-plastic and adhesive normal contact models. The first model is appropriate for simulating non-adhesive and dry granular materials where no viscous damping term is used. This makes the energy dissipation to be independent on the relative velocities of neighbouring particles. For sinter beds where granules are wet and sticky, an adhesive normal contact model was used in order to capture the particle-particle interactions. The contact forces are time-dependent and can increase the adhesion and stiffness after initial contact. The magnitude of the normal adhesive force is given by (Rocky DEM, 2016b):

$$F_{n.adh}^t = 0 \text{ if } -\Delta\delta_n \geq \delta_{adh} \quad \text{Eq. 7.4}$$

$$F_{n.adh}^t = f_{adh} * \min(m_i, m_j) * g \text{ if } -\Delta\delta_n < \delta_{adh} \quad \text{Eq. 7.5}$$

$$\Delta\delta_n = \delta_n^t - \delta_n^{t-dt} \quad \text{Eq. 7.6}$$

if $\Delta\delta_n < 0$, particles separate

$\Delta\delta_n > 0$, particles approach each other

where $F_{n.adh}^t$ is the normal adhesive contact force at the current time, t . $\Delta\delta_n$ is the difference between the contact normal overlap values at the previous time (δ_n^{t-dt}) and

current time (δ_n^t). f_{ad} is the adhesion force fraction and g is the gravity acceleration. δ_{ad} is the maximum normal overlap beyond which there is no adhesion between particles. If the force fraction is 1.0, the adhesive force will be equal to the gravity force applied to the particle. In practice, Rocky DEM uses force fraction between 0 (0%) and 0.5 (50%) to make simulations to reproduce the real behaviour of wet and sticky particles. The implementation of an adhesion model in Rocky is based on the measurement of the two parameters:

- Minimum distance between particles before the adhesion forces are applied
- Adhesion force expressed in terms of fraction of the particle gravity force.

7.2.1.2. Particle size distribution

The size distribution of granules is one of the most important parameters that control the pressure drop over the sinter bed. The granule size distribution is set to be narrower than that of the feed particles (Figure 2.1). This leads to produce sinter beds with higher permeability (Ball et al., 1973; Ellis et al., 2007; Ennis and Litster, 1997; Formoso et al., 2003; Khosa and Manuel, 2007; Litster and Waters, 1988; Loo et al., 1992; Voice et al., 1953).

The behaviour of the granular materials is strongly dependent on the particle size distribution. The difference in particle size can lead to size segregation through the percolation mechanism whereby fines can sift through the voids of larger particles (Berger and Hrenya, 2014; Li et al., 2010; Standish, 1979). This can result in various types of collisions between particles (small-small, small-large and large-large particle collisions) and an increase in computational costs. The particle size distribution can strongly affect the pressure drop through the sinter bed (Kasai et al., 1989; Rankin et al., 1985). Narrower particle size distribution results in formation of looser packing than wider size distributions.

The particle size distribution is often a built-in function in a DEM model. It can be implemented as probability density functions for normal and logarithmic distributions (Cundall and Strack, 1979). The DEM model can then capture the virtual particle size

distribution through two parameters: the arithmetic size mean and standard deviation from the experimental size distributions. In Rocky DEM, the particle size distribution can be implemented as the cumulative percent finer (passing). This makes Rocky DEM particles to have the same size distribution as the real-world particles.

7.2.1.3. Particle shape

Sphere-based particles are often used to study the behaviour of the granular materials (Cundall and Strack, 1979). Spherical shapes are simple to implement in 3D modelling and fast computationally. However, the spheres cannot reproduce the interlocking phenomena that are obvious in the real-world particles. Spheres roll continuously and have lower shear resistance and lower friction coefficient than those of irregular and non-spherical particles.

Previous studies reported that real particles are very difficult to be accurately simulated. The shape of irregular particles can be modelled by using ellipsoid (Lin and Ng, 1997) and superquadratic shapes (Williams and Pentland, 1992). Another approach consists of simulating any particle shape by building a clump of overlapping spheres (Favier et al., 1999; Lim and McDowell, 2005; Majidi et al., 2015; Price et al., 2007). The contact properties between the spheres are set in a way to prevent any interactions between spheres within each clump. It is established that an increase in the number of spheres in the clump will lead to more accurate approximation of the particle shape and higher computational costs. Rocky package belongs to the family of the discrete element models, whereby a random 3D shape can be estimated from a broader collection of predefined shapes that include polygons, polyhedrons, rods, pellets and briquettes. It also offers a possibility to import a custom shape. Spheres can be used to approximate non-spherical particles if the resistance to rolling is activated in the DEM simulation.

7.2.2. Fluid flow simulation

Prediction of the pressure drop through a sinter bed was calculated by using a DEM – CFD two-way coupling approach (Chapter 6 and Appendix F). A multiphase flow model was used to simulate the fluid flow, whereby the air was set to be the first fluid

phase. The DEM simulated sinter bed was considered as the secondary fluid phase and was imported into the CFD model.

7.3. Numerical simulation configuration

In this study, the granules from the base mixture were selected for validation of granule properties. The structure of granules is complex as shown in Figure 3.6, Figure 4.8 and Figure 4.10. The adhering layer is fragile, deformable and sticky and this makes it difficult to characterise granule properties in terms of stiffness, coefficient of restitution and adhesion force (Ishihara et al., 2013; Nakano et al., 2012).

The measurement of the stiffness (Young's modulus), coefficient of restitution and adhesion force is not evident for irregular – deformable – sticky particles. A simple approach was adopted herein, whereby each parameter can be changed while the other ones are kept constants during DEM-CFD simulations. Thereby the appropriate combinations of particle size, shape and contact forces could be chosen. The Young's modulus was selected based on previous investigations of the behaviour of iron ore granules and pellets. The simulation of the collapse of the sinter bed on the sintering machine was effectively achieved by choosing a range of Young's moduli between 10^6 and 10^7 Pa (Ishihara et al., 2013; Nakano et al., 2012). Wang et al. (2015) studied the validation of the flow simulation of iron ore green pellets using a non-smooth discrete element method. Experimental and simulation results were comparable for a Young's modulus of 6.2 MPa for 12 mm pellet diameter size.

The adhesion force was expressed in terms of force fraction, which could vary from 0 to 0.5 (Rocky DEM, 2016b). The coefficient of restitution was difficult to determine due to the deformability and stickiness of granules. The coefficient of restitution was set to the lowest default value (0.1) that Rocky can capture. Spheres, rounded polygons and polyhedrons were used to represent the irregularity of granules. The custom shapes with overlapping spheres were not considered due to the limit of available computation resources. The rolling resistance was implemented in DEM to account for the particle shape effect on the overall behaviour of the granular flow. The size distribution and

friction coefficient of granules were captured as raw data obtained from sieving of partially dried granules and slump tests respectively (Chapter 3). The input parameters for DEM-CFD simulation are given in Table 7.1. The geometrical dimensions of the reduced scale packed bed are given in Section 6.4.6.

Table 7.1. Input parameters for DEM-CFD simulation

Parameters	Value
Granule density (kg/m ³)	2000
Granule shape	Sphere, rounded polygon and polyhedron
Force fraction (-)	0.05; 0.1; 0.2; 0.3; 0.5
Friction coefficient (-)	1.0
Young's modulus (MPa)	0.1 - 1
Coefficient of restitution (-)	0.1
Rolling resistance (default)	0.15
Air velocity (m/s)	0.68
Time step (DEM; CFD) (s)	6.10 ⁻⁶ ; 10 ⁻³

7.4. Results and discussion

7.4.1. DEM – CFD simulations for the base mixture

In this section, the effect of each parameter was determined by comparing the predictions to experimental pressure drops through granules from the base mixture.

7.4.1.1. Effect of spring stiffness (Young's modulus)

The stiffness of deformable and sticky granules can have a great influence on the overlapping between particles. Simulations were carried out using spheres with eight values of Young's modulus: 10⁵, 1.05x10⁵, 1.1x10⁵, 2x10⁵, 5x10⁵, 10x10⁵ Pa. The size distribution of granules was truncated at 0.5 mm to reduce the number of DEM particles. An increase in the Young's modulus from 10⁵ to 10⁶ Pa resulted in a

decrease in the pressure drop through the packed bed of iron ore granules (Table 7.2). Good agreement between the measured and predicted pressure drop was achieved at low Young's modulus (105000 and 110000 Pa), with deviations of less than 10%.

Table 7.2. Comparison of measured pressure drop and predicted pressure drop for different Young's modulus parameters

Young's modulus (Pa)	Predicted pressure drop (Pa)	Measured pressure drop (Pa)	Deviation (%)
100000	11770	9806	- 20.03
105000	10431	9806	- 6.38
110000	9500	9806	3.15
200000	5503	9806	43.88
500000	3776	9806	61.49
1000000	2563	9806	73.86

7.4.1.2. Effect of adhesion force (force fraction)

Five force fractions (0.02, 0.05, 0.1, 0.2 and 0.5) were used to study the effect of adhesion on the pressure drop over iron ore granules. The simulations were performed using spheres with equivalent size distribution of granules from the base mixture. The spring stiffness was set to 105000 Pa. From these results, it is clear that the pressure drop is not dependent on the adhesion force at constant stiffness (Figure 7.4). The simulations with different force fractions reproduced the measured pressure drop well, with deviations within 10% (Appendix G). For granules with no adhesion force (0% force fraction), the granules are considered as elastic particles. The adhesion force was not activated, resulting in higher deviation (29.46%) from the measured pressure drops (Figure 7.4).

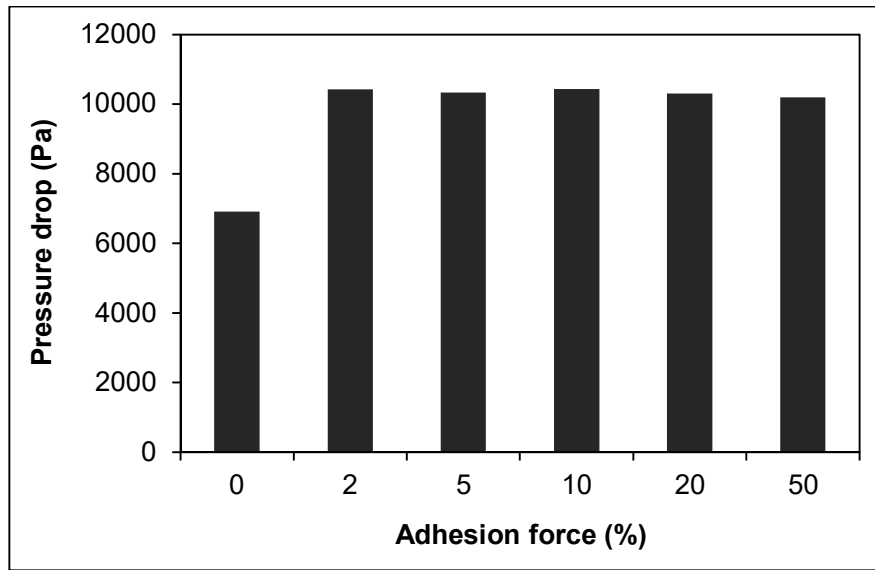


Figure 7.4. Variation of pressure drop with adhesion force (force fraction)

7.4.1.3. Effect of fine size fraction

The particle size distribution has a great influence on the computing time in DEM simulations. The simulation of narrow particle size distribution is known to run faster than boarder size distributions of particles (Berger and Hrenya, 2014). The presence of a large fraction of fine particles can increase the overall number of particles and computational costs for the same simulation conditions.

The effect of a narrower size distribution was studied by comparing pressure drops through granules with full and truncated size distributions. The cut-sieve was estimated at 5 mm size fraction, which commonly represents the cut-off size between adhesive fines and coarse particles. In this study, the finer size fraction (< 0.5 mm) was assumed to have been broken off from the big granules during screening. Hence, two size ranges from 0 to 10 mm and 0.5 to 10 mm (PSD truncated at 0.5 mm and normalised) were considered (Table 7.3). The numerical simulations were carried out with constant physical and dynamic properties listed in Table 7.1.

Table 7.3. Mass percentage of full and truncate size distributions for base case

Size fraction	Mass percentage (%)	
	Full PSD	Normalized truncated PSD at 0.5 mm
4.75 - 10.00 mm	51.00	51.14
2.00 - 4.75 mm	39.64	39.75
1.00 - 2.00 mm	7.86	7.88
0.50 - 1.00 mm	1.23	1.23
0.25 – 0.50 mm	0.19	0
< 0.25 mm	0.08	0
Total	100	100

The number of particles (168500 particles) in the simulation with wider size distribution (0 – 10 mm size fraction) was higher than that of the equivalent system (58089 particles) with a truncated size distribution (0.5 – 10 mm). The DEM simulation with wider PSD took 24.5 hours to complete. The computing time was substantially shorter (~ 2 hours) for a size distribution without the finer fraction. The presence of the finer fraction in the sinter bed resulted in an increase in pressure drop, with a deviation of 17.08% between the full and truncated size distributions. The predicted pressure drop through the sinter bed with a 0.50 – 10 mm size fraction was comparable to the measured pressure drop with a deviation of 6.37%, less than the accepted limit of 10% (Table 7.4).

Table 7.4. Comparison between simulations with full and truncated size distribution

Size distribution range (mm)	Number of particles	Computing time (hours)	Predicted pressure drop (Pa)	Measured pressure drop (Pa)	Deviation (%)
0 – 10 mm	168500	24.5	11481	9806	- 17.08
0.5 – 10 mm	58089	2.10	10430	9806	- 6.38

7.4.1.4. Effect of granule shape

It is well established that the particle shape is important to represent the behaviours of real particles in DEM simulation. The iron ore granules are of many individual shapes, but it is not practical to implement many individual shapes in DEM (German, 1989; Thomas and Bray, 1999).

The shapes of iron ore granules are complex and difficult to be represented from a geometric point of view. In this study, the effect of the granule shape was studied by carrying out simulations with spheres, rounded polygons (4 and 25 corners) and polyhedrons (4 and 25 corners). The examined shapes are shown in Table 7.5.

Table 7.5. Examined shapes of DEM particles

	Sphere	Rounded polygons		Rounded polyhedrons	
Shape					
Number of corners	∞	25	4	25	4
Order of angularity		Increase in angularity 			

The rounded polyhedrons are more angular than those of rounded polygons. The angularity in each shape group increases with a decrease in the number of corners. All the irregular shapes had an average ratio of width/length and thickness to width of 0.85 ($> 2/3$) and 0.68 ($> 2/3$) respectively, and matched with the spherical-shape group according to Zingg's classification (Zingg, 1935).

The irregular shape of the particles prevented the formation of a dense packing. The pressure drop through packed beds decreased with a decrease in sphericity of the particles and an increase in angularity (Figure 7.5). Spheres have no rolling resistance and percolate easily to form dense packed beds with higher pressure drops. The decrease in pressure drop was more significant in the case of rounded polyhedrons than that of rounded polygonal shapes. The interlocking forces are more significant in packed bed of particles with shaper corners (higher angularity) than that with rounded ones (Hinkley et al., 1994a, 1994b). Consequently rounded polyhedrons with 4 corners formed the loosest packed bed with the lowest pressure drop (Figure 7.5). The predicted and measured pressure drops through spheres and rounded polygons were comparable with deviations smaller than 10% (Appendix G).

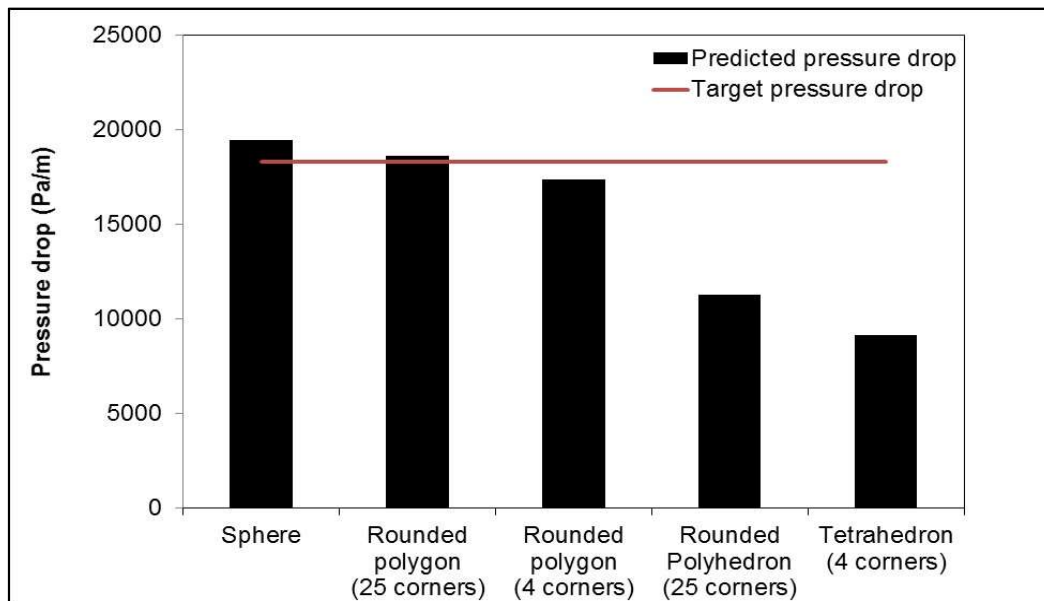
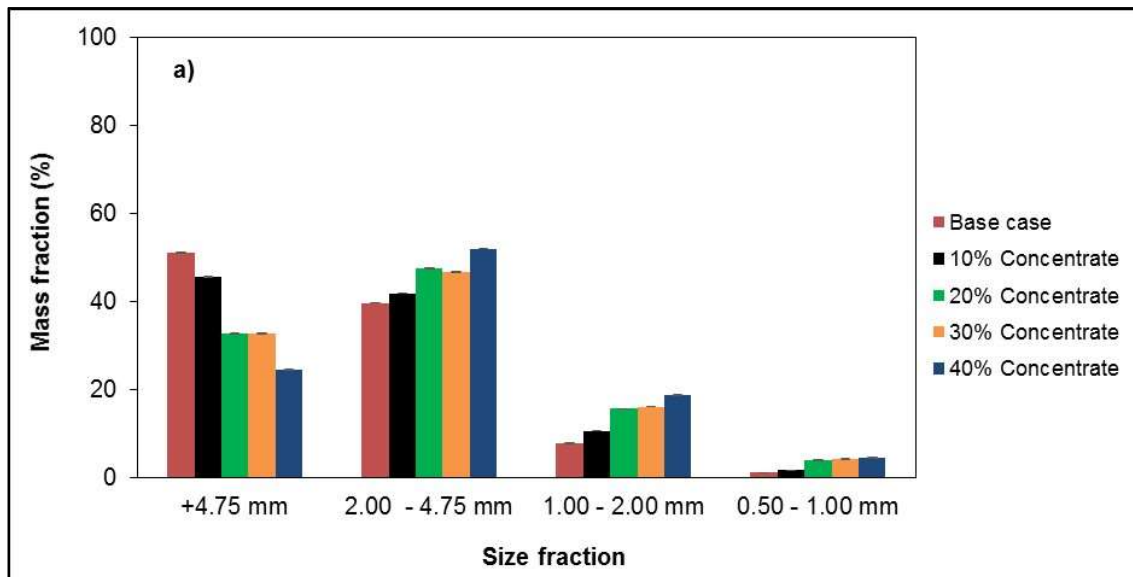


Figure 7.5. Variation of pressure drop with particle shape

7.4.2. DEM – CFD simulations for mixtures with concentrate and micropellets

In this section, spheres with equivalent dynamic properties (stiffness, friction and adhesion) were used during DEM – CFD simulations of the pressure drop through granulated mixtures with concentrate and micropellets. The simplification of the particle shape was adopted to avoid running DEM simulations beyond available computational resources. The adhesion force was kept constant (10% force fraction). The size distribution of granules was truncated at 0.5 mm size fraction. The truncated size distribution of the granules is given in Figure 7.6. The mass fraction of +4.75 mm granule size (big granules) decreased with addition of concentrate and micropellets, while that of small size fractions (less than +4.75 mm) increased. Addition of 40% micropellets increased the +4.75 mm size fraction due to the formation of granules from adherence of the micropellets to large granules (Figure 7.6).



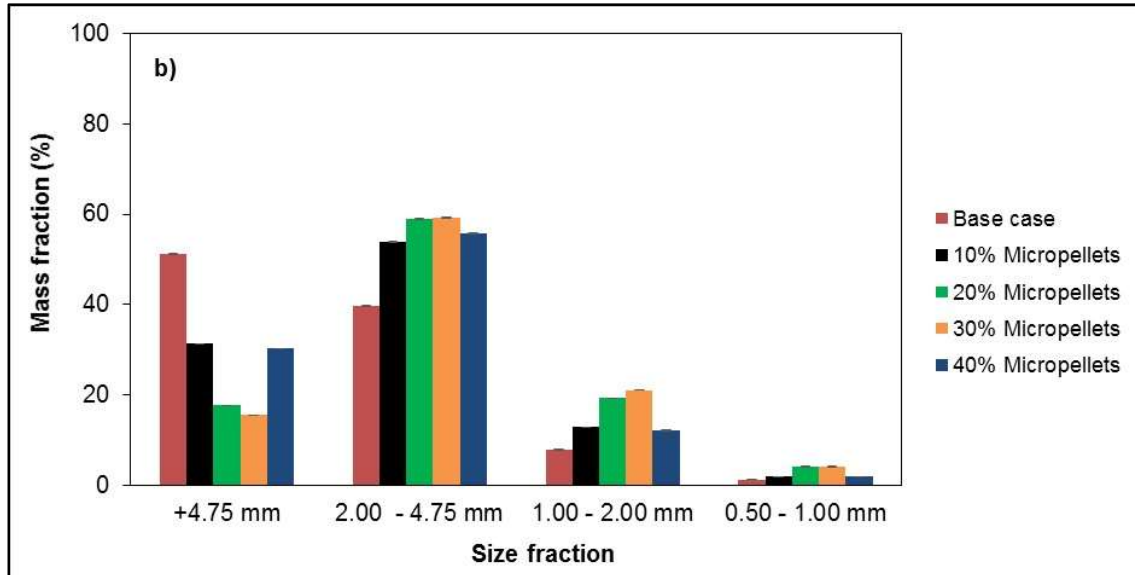


Figure 7.6. Variation of size fraction with the addition of concentrate and micropellets

The presence of small size fractions in multi-sized systems was reported to slightly increase the overall stiffness of the packing (Su et al., 2002). Guan et al. (2012) found that the macroscopic Young's modulus is inversely proportional to particle diameter for a packing rock layers. In this section, the stiffness (Young's modulus) was therefore adjusted to 130000 Pa to account for the increase in small size fractions with addition of concentrate and micropellets. The density of granules varied between 2000 to 2150 kg/m³. The addition of concentrate and micropellets (0 - 40%) decreased the static friction coefficient from 1 to 0.78 (45 to 38°) and 1 to 0.62 (45 to 32°) respectively for granules obtained at optimum moisture (Section 3.2.4.3). The flow rate of air was experimentally adjusted to obtain a constant pressure drop of 9806 Pa through all granulated mixtures. An increase in concentrate and micropellets resulted in a decrease in the bed permeability and velocity of air through the sinter beds (Section 3.2.2). The main input parameters that varied with addition with concentrate and micropellets are given in Table 7.6.

Table 7.6. Parameters for DEM - CFD simulations

Mixtures	Density (kg/m ³)	Stiffness (Pa)	Friction coefficient	Air velocity (m/s)
Base case	2000	105000	1.00	0.68
10% Concentrate	2050	105000	0.84	0.61
20% Concentrate	2100	130000	0.90	0.61
30% Concentrate	2100	130000	0.84	0.55
40% concentrate	2150	130000	0.78	0.51
10% Micropellets	2100	130000	0.81	0.61
20% Micropellets	2150	130000	0.84	0.55
30% Micropellets	2150	130000	0.81	0.55
40% Micropellets	2100	130000	0.62	0.58

The pressure drop through different granulated mixtures was calculated by coupled DEM – CFD simulations. The full description of the simulation approach was described in Appendix F. The number of DEM particles to fill the same packing volume increased with the addition of concentrate and micropellets (Figure 7.7). This was due to an increase in small size fractions (-4.75 mm). For a mixture with 40% micropellets, the number of DEM particles decreased due to a slight increase in the mass fraction of +4.75 mm granule size.

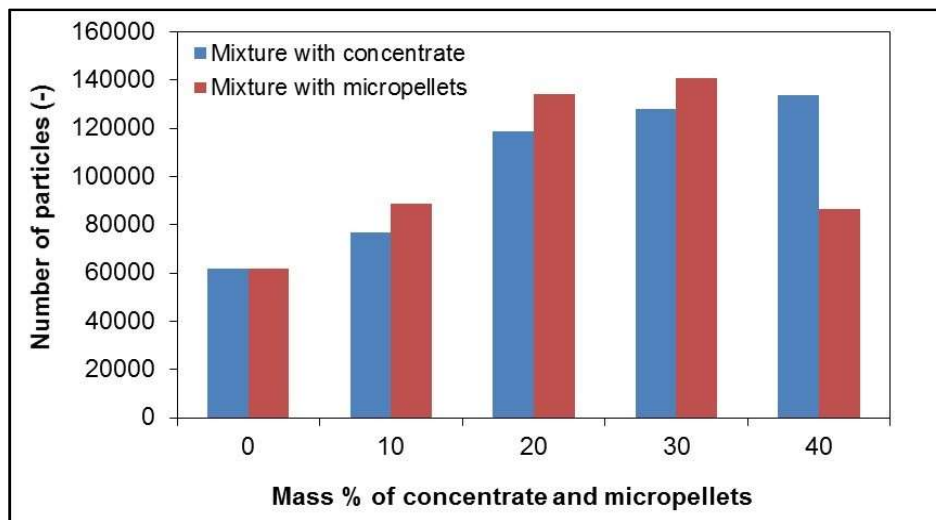


Figure 7.7. Variation of the number of DEM particles with the addition of concentrate and micropellets

The predicted and measured pressure drops were comparable for stiffness ranging from 105000 Pa to 130000 Pa. The selected values of the stiffness matched the range of stiffness coefficients that were used in the studies by Ishihara et al. (2013) and Nakano et al. (2012). The deviations between measured and predicted pressure drops through granulated mixtures with concentrate and micropellet addition were found to be within an acceptable accuracy of $\pm 10\%$ (Figure 7.8).

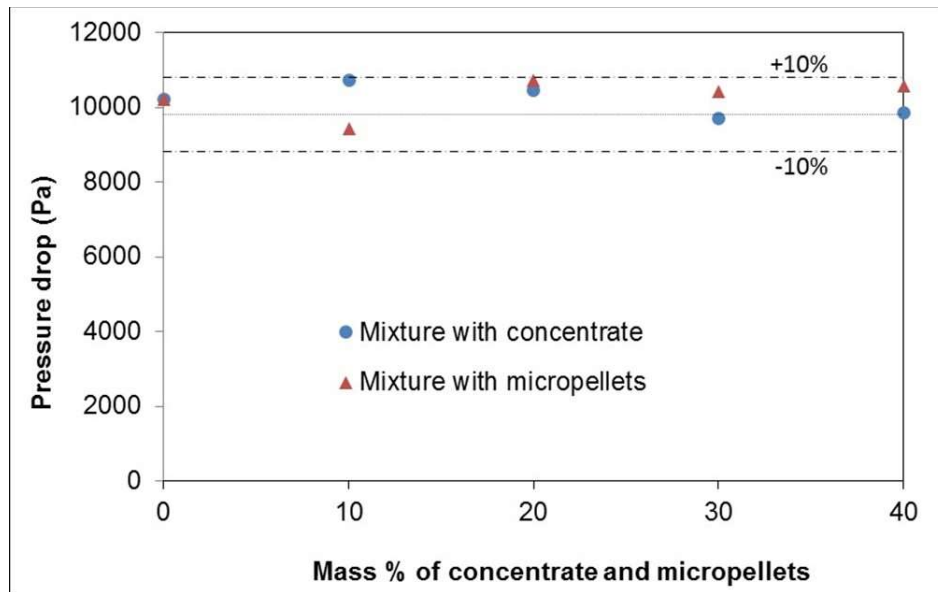


Figure 7.8. Comparison between the measured and predicted pressure drops through granulated mixtures with addition of concentrate and micropellets

7.5. Conclusions

Coupled DEM - CFD simulations of pressure drops across a simulated sinter bed, based on spheres and irregular particles, were investigated in this study. This approach was first applied to the base mixture to validate the spring stiffness, adhesion force fraction and size distribution range. The application of the model was extended to analyse the effect of Young's modulus, particle size distribution and irregularity of shape. The rolling resistance was also considered to represent the effect of the

irregularity of the granules. The major conclusions drawn from the study are summarized as follows:

- DEM – CFD simulations were carried out with Young's modulus values that are within the range of 0.1 to 1 MPa. For mixtures with addition of concentrate and micropellets, the Young's modulus was varied between 0.105 and 0.130 MPa in order to match the experimental measurements.
- The variation of the adhesion force fraction from 2% to 50% did not affect the pressure drop when other DEM parameters (shape, size distribution, Young's modulus, coefficient of static friction and coefficient of restitution) were kept constant.
- The particle shape had a strong effect on the pressure drop. For simulations with a constant Young's modulus, particles of angular shape (tetrahedron: 4 corners) produced lower pressure drop. While the predicted and measured pressure drops were in good agreement for the corresponding rounded polygon with 4 corners. The nature of corners (sharpness and roundness) could represent the level of the interlocking between irregular particles.
- The coupled DEM – CFD approach with spherical particles proved to be an important step towards understanding the packing of iron ore granules in the permeameter. The improvement of the computational resources (use of Graphics Process Unit, GPU) could help to carry out DEM simulations with complicated shapes.
- The simulation using spheres with equivalent parameters of irregular particles was in agreement with the experimental measurements for granulated mixtures with addition of concentrate and micropellets. The deviations were within $\pm 10\%$.

8. Conclusions

8.1. Introduction

This thesis presented experimental and numerical studies of the permeability of sinter beds that contain concentrate and micropellets. In Chapter 2, a comprehensive review of the green bed permeability was discussed. It was shown that the structure of the sinter bed determines its permeability (pressure drop) and therefore the productivity of the sinter plant. For a high productivity, a high permeability is required. The structure of the sinter bed, and therefore its permeability, is defined by its voidage, coefficient of static friction (angle of repose), granule size distribution and the shape of the granules.

Numerical experiments using a coupled DEM – CFD model could not be carried out without accurate information on bulk parameters of a sinter bed: voidage (Chapter 3), angle of repose (Chapter 3), shape and structure of granules (Chapter 4) and granule size distributions (Chapter 5). The DEM - CFD coupling algorithm was validated and verified through the use of glass beads (Chapter 6) and real measured data on granulated mixtures (base case, concentrate addition and micropellet addition) (Chapter 7).

8.2. Conclusions

The conclusions drawn from the experimental, analytical and DEM-CFD simulation studies are presented in the following sections.

8.2.1. Experimental and analytical studies

The voidage, coefficient of static friction (angle of repose), moisture, mean size, size distribution and shape of the granules are well-known to be critical parameters that significantly affect the permeability of sinter beds. The voidage and permeability of a sinter bed are strongly correlated. The higher the voidage the higher the permeability of the sinter bed. The angle of repose expresses the magnitude of static friction between granules. More friction indicates less mobility of a mass of granules resulting

in higher angle of repose and higher bed permeability. The mean size of granules influences the packing. Fine particles tend to form close packing with low permeability whereas coarse particles likely form loose packing with high permeability. Granules with high moisture content have less granule-to-granule interlocking and low angle of repose. This partially explains the drop of the bed permeability after reaching the maximum moisture content. The deformation of granules at higher moisture is also important. A build-up of fines around large particles produces a layer of fines that can easily deform. This may contribute to a decrease in bed voidage (Hinkley et al., 1994b). Granules with a wider size distribution form a closer packing, whereby the bed permeability are reduced due to obstruction of voids by fine fraction of granules. Shape of granules that deviates more from the sphere cause more granule-to-granule interlocking resulting in a loose packed bed with higher permeability.

A series of permeability tests were performed to investigate the effect of concentrate and micropellet addition on the green bed permeability. The experiment data showed that the permeability of beds decreases with addition of concentrate and micropellets. This is a consequence of a decrease in voidage, angle of repose, mean granule size and irregularity of granules. Mixtures containing concentrate and micropellets produced smaller granules with lower angle of repose. The decrease in voidage was significant for mixtures that contain concentrate, as the resulting granules can easily deform and form compact sinter beds with low voidage. Incorporating concentrate and micropellets in the base mixture decreased the angle of repose. The granules become more spherical and form sinter beds with lower angles of repose.

Based on optical microscopy and X-ray micro-tomography analysis, four mechanisms governing the formation of granules in mixtures that contain concentrate and micropellets were observed. Auto layering of fines around coarse particles was the main mechanism. With the addition of concentrate, a secondary mechanism was identified as coalescence of microgranules, while with the addition of micropellets, adhesions between micropellets and between granules and micropellets occurred. Litster's model was successfully applied in the prediction of the mean granule size for mixtures that contain concentrate and micropellets. The mean absolute percentage

error was less than 10%. The granule growth during granulation showed a strong correlation with the ratio of adhering fines to nuclei. The granule growth increased with an increase in concentrate content and ratio of adhering fines to nuclei. More adhering fines were available for the autolayering and coalescence mechanisms to take place. In mixtures with micropellet addition, the granule growth decreased with an increase in micropellet content due the deficiency in adhering fines. The average values of five shape parameters (operational sphericity, Krumbein sphericity, Corey shape factor and Janke form factor) were used to investigate the effect of concentrate and micropellet addition on the shapes of the produced granules. The addition of concentrate and micropellets increased the average sphericity of the granules. This result was confirmed by the sphericity distribution from Zingg diagram. The distribution of granule sphericity showed that the bed permeability decreased with an increase in the population of granules in the 0.9 - 1 for granules from mixtures with concentrate and micropellet addition.

8.2.2. DEM – CFD simulations

The purpose of the simulation study was to validate and extend a DEM – CFD coupling model to numerically predict the pressure drop through complex systems consisting of moist granules that are loaded into a permeameter. Base mixture was used to conduct a study of the effect of the size distribution, shape, stiffness and adhesion on the pressure drop simulations. The model was first implemented with packed beds, which consisted of monosized and bisized glass beads. The key conclusions are:

- Comparison between the simulated pressure drops through glass beads and those obtained in the experimental tests showed good agreement with a deviation within 10%. One and two-way DEM - CFD coupling models were validated for single and binary packed beds of glass beads.
- The Young's modulus was found to significantly influence the granule – granule interactions during loading. For tested granulated mixtures, the Young's modulus ranged from 0.103 MPa to 0.130 MPa. The addition of concentrate

and micropellets required an adjustment of the Young's modulus to higher values (0.13 MPa). This was due to an increase in small size fractions (- 4.75 mm) which consequently resulted in a slight increase in the bulk stiffness of the examined multi-sized systems (Su et al., 2002).

- An increase in the adhesion force fraction from 0.02 to 0.5 does not affect the pressure drops through packed beds of granules. Pressure drops through the granules from the base mixture were 10425 Pa and 10431 Pa when the adhesion force fractions were set to 0.02 and 0.1 respectively. The simulation of the pressure drop over granules with no adhesion (0% fraction force) resulted in a lower pressure drop of 6971 Pa. This confirms the importance of defining the adhesion force during DEM simulations of wet and sticky granules.
- The shape of granules was found to have a significant effect on the pressure drop through packed beds (granules). The tetrahedron with 4 corners had a higher potential for particle interlocking which contributed to the lower pressure drop (4900 Pa), while spheres easily moved and formed dense packing with the higher pressure drop (10430 Pa). Based on the current computational resources, the DEM is still unable to simulate a sinter bed with more complex granule shape.
- The application of the developed Rocky DEM – CFD coupling model in the simulation of pressure drops through granulated mixtures with addition of concentrate and micropellets showed good agreement between the measured and simulated results, with a deviation within $\pm 10\%$.

Green bed permeability depends on the properties of iron ore granules. Therefore, better understanding of how they influence practical applications is extremely important. The base mixture produced granules with a higher mean size and lower sphericity (0.7 - 0.8), which contributed to the formation of a sinter bed with high permeability. In the model of Litster, the ratio R of fines to coarse particles (nuclei) was

established to be an important parameter in the characterisation of raw materials (sinter feed). To obtain high bed permeability, the ratio R of fines to coarse particles must be set to an optimum value. Higher ratio R produced more microgranules (coalescence) while lower ratio R delayed the growth of granules. Both scenarios resulted in lower permeability of sinter beds that contain concentrate and micropellets. The first step to numerically measure the pressure drop using a coupled DEM – CFD model is to determine the properties of iron ore granules (size distribution, angle of repose, average shape and Young's modulus) as DEM inputs parameters. The size distribution of granules can be analytically determined by Litster's model while the other granule parameters can be estimated by comparing some numerical results with the bulk experiments (slump test and drop test).

9. Recommendations for future work

While this study provided a frame work whereby the pressure drop through granulated mixtures can be calculated, the determination of the DEM parameters (Young's modulus, adhesion force and coefficient of restitution) of iron ore granules remained a challenge. A comprehensive study of validation for the Young's modulus, adhesion force and coefficient of restitution could be necessary to confirm the values of these parameters.

More computational power would be needed in order to get rid of the restriction of the granule shape. For example, a GPU (Graphics Process Unit) could be used in DEM simulations of polydispersed granules in sizes and irregular shapes.

Furthermore, it could be important to study the effect of the fine particle fraction/particle size distribution of the mixtures on the dynamic properties (Young's modulus, adhesion force and coefficient of restitution) although the mechanical behaviour of the granulated mixtures is not yet fully understood.

Rocky packages predicted the pressure drop through mono sized glass beads and binary mixture. The over and under prediction of the pressure drop could be attributed to the non-uniformity of the spatial particle distribution in the packed bed. It is thus advisable to compare the packing composition of the experimental and simulated packed beds. This would certainly lead to understand the deviations observed in this study.

REFERENCES

- Abe, E., Hirose, H., Yokota, A., 1979. Pressure drop through a packed bed of binary mixture. *J. Chem. Eng. Japan* 12, 302–306.
- Adetayo, A.A., Litster, J.D., Pratsinis, S.E., Ennis, B.J., 1995. Population balance modelling of drum granulation of materials with wide size distribution. *Powder Technol.* 82, 37–49.
- Allen, T., 1990. Particle size measurement, 4th Editio. ed. Chapman and Hall, New York.
- Anderson, J.D., 1995. Computational Fluid Dynamics: The Basics with Applications. McGraw-Hill Education, New York.
- Anderson, T.B., Jackson, R., 1967. Fluid Mechanical Description of Fluidized Beds. Equations of Motion. *Ind. Eng. Chem. Fundam.* 6, 527–539.
- Ansys, I., 2012. ANSYS Fluent Theory Guide, Rel.14.5. Canonsburg.
- Aryaei, A., Hashemnia, K., Jafarpur, K., 2010. Experimental and numerical study of ball size effect on restitution coefficient in low velocity impacts. *Int. J. Impact Eng.* 37, 1037–1044.
- Bai, H., Theuerkauf, J., Gillis, P.A., Witt, P.M., 2009. A Coupled DEM and CFD Simulation of Flow Field and Pressure Drop in Fixed Bed Reactor with Randomly Packed Catalyst Particles. *Ind. Eng. Chem. Res.* 48, 4060–4074.
- Bai, H., Theuerkauf, J., Witt, P., Gillis, P., 2004. Modelling fluid flow and pressure drop in packed beds with coupling DEM and CFD. *AIChE 2004 Fall Annu. Meet.*
- Baker, M.J., Tabor, G.R., 2010. Computational analysis of transitional air flow through packed columns of spheres using the finite volume technique. *Comput. Chem. Eng.* 34, 878–885.
- Ball, D.F., Dartnell, J., Davison, J., Grieve, A., Wild, R., 1973. Agglomeration of iron ores. Heinemann Educational Books Ltd, London.
- Barksdale, R.D., Kemp, M.A., Sheffield, W.J., Hubbard, J.L., 1991. Measurement of aggregate shape, surface area, and roughness. Washington, DC.
- Barrett, P.J., 1980. The shape of rock particles, a critical review. *Sedimentology* 27,

291–303.

- Barrios, G.K.P., de Carvalho, R.M., Kwade, A., Tavares, L.M., 2013. Contact parameter estimation for DEM simulation of iron ore pellet handling. *Powder Technol.* 248, 84–93.
- Bartlett, C., Gerlach, W., Koepf, M., 2009. Options in sintering to meet future industry needs. *Millenn. Steel* 37–40.
- Bear, J., 1972. *Dynamics of fluids in porous media*. Elsevier, New York.
- Benyahia, F., O'Neill, K.E., 2005. Enhanced Voidage Correlations for Packed Beds of Various Particle Shapes and Sizes. *Part. Sci. Technol.* 23, 169–177.
- Berger, K.J., Hrenya, C.M., 2014. Challenges of DEM: II. Wide particle size distributions. *Powder Technol.* 264, 627–633.
- Bhuiyan, I.U., 2011. *Characterization of Iron Ore Green Pellets by Scanning Electron Microscopy and X-ray Microtomography*. Luleå University of Technology, Luleå, Sweden.
- Blott, S.J., Pye, K., 2008. Particle shape: A review and new methods of characterization and classification. *Sedimentology* 55, 31–63.
- Borges, W., Melo, C., Braga, R., Santos, E., Maria, C., Kojima, O., Sato, H., Arcelor, C.S.B., 2004. Application of HPS (Hybrid Pelletized Sinter) process at Monlevade Works * Application du procédé HPS (« Hybrid Pelletized Sinter ») à l'usine de Monlevade 189–194.
- Brawn, G.G., Foust, A.S., Katz, D.L., Schneidewind, R., White, R.R., 1950. *Unit Operations*. John Wiley and Sons, New York.
- Carstensen, J.T., Chan, P.-C., 1976. Relation between particle size and repose angles of powders. *Powder Technol.* 15, 129–131.
- Chauveteau, G., Thirriot, C., 1967. Régimes d'écoulement en milieu poreux et limite de la loi de Darcy. *La Houille Blanche* 22, 1–8.
- Coetzee, C.J., 2016. Calibration of the discrete element method and the effect of particle shape. *Powder Technol.* 297, 50–70.
- Coetzee, C.J., Els, D.N.J., 2009. Calibration of granular material parameters for DEM modelling and numerical verification by blade–granular material interaction. *J.*

Terramechanics 46, 15–26.

- Cores, A., Babich, A., Muñiz, M., Ferreira, S., Mochon, J., 2010. The Influence of Different Iron Ores Mixtures Composition on the Quality of Sinter 50, 1089–1098.
- Corey, T., 1949. Influence of shape on the fall velocity of sand grains. Colorado Agricultural and Mechanical College, Fort Collins, Colorado, USA.
- Cumberland, D.J., Crawford, R.J., 1987. The packing of particles. Vol. 6 Handb. powder Technol.
- Cundall, P.A., 1971. A computer model for simulating progressive large-scale movements in block rock mechanics. In: Proc. Symp. Int. Soc. Rock Mech. Nancy, France, pp. 128–132.
- Cundall, P.A., 1987. Distinct element models of rock and soil structure. In: E.T. Brown (Ed.), Analytical and Computational Methods in Engineering and Rock Mechanics. Allen and Unwin, pp. 129–163.
- Cundall, P.A., Strack, O.D.L., 1979. A discrete numerical model for granular assemblies. *Géotechnique* 29, 47–65.
- De Beer, F.C., 2005. Characteristics of the Neutron/X-ray tomography system at SANRAD facility in South Africa. *Nucl. Instr. Meth. Phys. Res. A* 542, 1–8.
- Debroux, F., Cleary, P.W., 2001. Characterising the angles of failure and repose of avalanching granular material using the discrete element method. In: 6th World Congress of Chemical Engineering. Melbourne, Australia.
- Di Felice, R., 1994. The Voidage function for fluid-particle interaction systems. *Int. J. Multiph. Flow* 20, 153–159.
- Dixon, A.G., 1988. Correlations for wall and particle shape effects on fixed bed bulk voidage. *Can. J. Chem. Eng.* 66, 705–708.
- Dudgeon, C.R., 1966. An experimental study of the flow of water through coarse granular media. *La Houille Blanche* 785–801.
- Dybbs, A., Edwards, R. V., 1984. A New Look at Porous Media Fluid Mechanics — Darcy to Turbulent. In: Jacob Bear; M. Yavuz Corapcioglu (Ed.), *Fundamentals of Transport Phenomena in Porous Media*. Springer Netherlands, Dordrecht, pp. 199–256.

- Ellis, B.G., Loo, C.E., Witchard, D., 2007. Effect of ore properties on sinter bed permeability and strength. *Ironmak. Steelmak.* 34, 10.
- Ennis, B.J., Litster, J.D., 1997. Particle size enlargement, R. Perry, D. Green (editors). *Perry's Chemical Engineers' Handbook*, 7th edition, McGraw-Hill, New York.
- Eppinger, T., Seidler, K., Kraume, M., 2011. DEM-CFD simulations of fixed bed reactors with small tube to particle diameter ratios. *Chem. Eng. J.* 166, 324–331.
- Erdoğan, S.T., 2003. *The Effect of Aggregates on the Properties of Concrete and Proportioning Methods*. The University of Texas at Austin.
- Erdoğan, S.T., Fowler, D.W., 2005. Determination of aggregate shape properties using X-ray topographic methods and the effect of shape on concrete rheology. Austin, Texas.
- Ergun, S., 1952. Fluid flow through the packed columns. *Chem. Eng. Prog.* 48, 89–94.
- Favier, J.F., Abbaspour-Fard, M.H., Kremmer, M., Raji, A.O., 1999. Shape representation of axi-symmetrical, non-spherical particles in discrete element simulation using multi-element model particles. *Eng. Comput.* 16, 467–480.
- Formoso, A., Moro, A., Fernández Pello, G., Menéndez, J.L., Muñiz, M., Cores, A., 2003. Influence of nature and particle size distribution on granulation of iron ore mixtures used in a sinter strand. *Ironmak. Steelmak.* 30, 447–460.
- Fraser, H.J., 1935. Experimental Study of the Porosity and Permeability of Clastic Sediments. *J. Geol.* 43, 910–1010.
- Fu, Y., 2005. *Experimental Quantification and Dem Simulation of Micro-Macro Behaviors of Granular Materials Using X-Ray Tomography Imaging*. Dep. Civ. Environ. Eng. Ph.D., 270.
- Furnas, C.C., 1929. Department of Commerce, Bureau of Mines, Report of Investigation Serial No. 2894, 1928. *Bull. US Bur. Mines* 73–84.
- Furnas, C.C., 1931. Grading Aggregates - I. - Mathematical Relations for Beds of Broken Solids of Maximum Density. *Ind. Eng. Chem.* 23, 1052–1058.
- Furui, T., M. Kawazy, Sugawara, K., Fujiwara, T., Kagawa, M., Sawamura, A., Uno, S., 1977. *Technology of preparation of raw materials to be sintered*. Japan.

- Gallas, J.J.A.C., Sokolowski, S., 1993. Grain non-sphericity effects on the angle of repose of granular material. *Int. J. Mod. Phys. B* 7, 2037–2046.
- Gan, M., Fan, X.H., Ji, Z.Y., Chen, X.L., Yin, L., Jiang, T., Yu, Z.Y., Huang, Y.S., 2015. Optimising method for improving granulation effectiveness of iron ore sintering mixture. *Ironmak. Steelmak.* 42, 351–357.
- Garboczi, E.J., 2002. Three-dimensional mathematical analysis of particle shape using X-ray tomography and spherical harmonics: application to aggregates used in concrete. *Cem. Concr. Res* 32, 1621–1638.
- German, R.M., 1989. *Particle Packing Characteristics*. Met. Powder Ind. Fed.
- Gidaspow, D., 1994. *Multiphase flow and fluidisation*, Academic P. ed.
- Gidaspow, D., Bezburuah, R., Ding, J., 1992. Hydrodynamics of circulating fluidized beds: Kinetic theory approach. In: 7th Engineering Foundation Conference on Fluidization, Fluidization VII. New York, NY: Engineering Foundation, Brisbane, Australia, pp. 75–82.
- Guan, C.Y., Qi, J.F., Qiu, N.S., Zhao, G.C., Yang, Q., Bai, X.D., Wang, C., 2012. Macroscopic Young's Elastic Modulus Model of Particle Packing Rock Layers. *Open J. Geol.* 2, 198–202.
- Haughey, D.P., Beveridge, G.S.G., 1969. Structural properties of packed beds — A review. *Can. J. Chem. Eng.* 47.
- Hausner, H., 1972. The role of Interparticulate friction in powder technology. In: 1. Int. Conf. Compacting Consol. Particulate Matter. Brighton, UK, pp. 7–12.
- Hekkala, L., Fabritius, T., Härkki, J., 2004. Mathematical model of heat and mass transfer in the steel belt sintering process. In: Tenth International Ferroalloys Congress: Transformation through Technology. Cape Town, pp. 586–592.
- Hertz, H., 1882. Über die Berührungsfester Elastischer Körper. *J. Reine Angew Math.* 92, 156–171.
- Hicks, R.E., 1970. Pressure Drop in Packed Beds of Spheres. *Ind. Eng. Chem. Fundam.* 9, 500–502.
- Hinkley, J., Waters, A.G., Litster, J.D., 1994a. An investigation of pre-ignition air flow in ferrous sintering. *Int. J. Miner. Process.* 42, 37–52.

- Hinkley, J., Waters, A.G., O'Dea, D., Litster, J.D., 1994b. Voidage of ferrous sinter beds: new measurement technique and dependence on feed characteristics. *Int. J. Miner. Process.* 41, 53–69.
- Hsieh, L.-H., 2005. Effect of Raw Material Composition on the Sintering Properties. *ISIJ Int.* 45, 551–559.
- Hu, J.Q., Rose, E., 1993. Simulation of iron ore sinter plant. *ACSE Res. Rep.* 488.
- Ishihara, S., Soda, R., Zhang, Q., Kano, J., 2013. DEM Simulation of Collapse Phenomena of Packed Bed of Raw Materials for Iron Ore Sinter during Charging. *ISIJ Int.* 53, 1555–1560.
- Itasca, I., 2003. PFC3D User Manual, Itasca Consulting Group Inc. Minneapolis, USA.
- Iveson, S.M., 2002. Limitations of one-dimensional population balance models of wet granulation processes. *Powder Technol.* 124, 219–229.
- Iveson, S.M., Holt, S., Biggs, S., 2004. Advancing contact angle of iron ores as a function of their hematite and goethite content: Implications for pelletising and sintering. *Int. J. Miner. Process.* 74, 281–287.
- Iveson, S.M., Litster, J.D., 1998. Growth Regime Map for Liquid-Bound Granules 44.
- Iveson, S.M., Litster, J.D., Hapgood, K., Ennis, B.J., 2001. Nucleation, growth and breakage phenomena in agitated wet granulation processes: a review. *Powder Technol.* 117, 3–39.
- Janke, N.C., 1966. Effect of shape upon the settling velocity of regular convex geometric particles. *J. Sediment. Petrol.* 36, 370–376.
- Jiang, M.J., Liu, J., Sun, C., Chen, H., 2015. DEM analyses of shear behaviour of rock joints by a novel bond contact model. *IOP Conf. Ser. Earth Environ. Sci.* 26, 12021.
- Jin-Sui, W., Shang-Xian, Y., 2009. A Micro-Mechanism Model for Porous Media. *Commun. Theor. Phys.* 52, 936–940.
- Johnson, K.L., Kendall, K., Roberts, A.D., 1971. Surface Energy and the Contact of Elastic Solids. In: *Proceedings of the Royal Society A: Mathematical, Physical and Engineering Sciences.* pp. 301–313.
- Kapur, P.C., Kapur, P., Fuerstenau, D.W., 1993. An auto-layering model for the

- granulation of iron ore fines. *Int. J. Miner. Process.* 39, 239–250.
- Kasai, E., Rankin, W.J., Gannon, J.F., 1989. The effect of raw mixture properties on bed permeability during sintering. *ISIJ Int.* 29, 33–42.
- Ketcham, R.A., Carlson, W.D., 2001. Acquisition, optimization and interpretation of X-ray computed tomographic imagery: applications to the geosciences. *Comput. Geosci.* 27, 381–400.
- Khosa, J., Manuel, J., 2007. Predicting Granulating Behaviour of Iron Ores Based on Size Distribution and Composition. *ISIJ Int.* 47, 965–972.
- Krumbein, W.C., 1941. Measurement and Geological Significance of Shape and Roundness of Sedimentary Particles. *SEPM J. Sediment. Res.* 11, 64–72.
- Krumbein, W.C., Sloss, L.L., 1963. *Stratigraphy and Sedimentation*, 2nd Ed. ed. W.H. Freeman, San Francisco.
- Leva, M., Grummer, M., 1947. Pressure Drop through packed tubes: Part III. Prediction of voids in packed tubes. *Chem. Eng. Prog.* 43, 713–718.
- Li, J., Yu, A.B., Bridgwater, J., Rough, S.L., 2010. Spontaneous inter-particle percolation: A kinematic simulation study. *Powder Technol.* 203, 397–403.
- Lim, W.L., McDowell, G.R., 2005. Discrete element modelling of railway ballast. *Granul. Matter* 7, 19–29.
- Lin, X., Ng, T.T., 1997. A three-dimensional discrete element model using arrays of ellipsoids. *Géotechnique* 47, 319–329.
- Litster, J., Ennis, B., 2004. *The Science and Engineering of Granulation Processes*, Particle Technology Series. Springer Netherlands, Dordrecht.
- Litster, J.D., Waters, A.G., 1986. Fundamentals of granulation of iron ore for ferrous sinter production. *Chemica* 86, 72–77.
- Litster, J.D., Waters, A.G., 1988. Influence of the material properties of iron ore sinter feed on granulation effectiveness. *Powder Technol.* 55, 141–151.
- Litster, J.D., Waters, A.G., 1990. Kinetics of iron ore sinter feed granulation. *Powder Technol.* 62, 125–134.
- Litster, J.D., Waters, A.G., Nicol, S.K., 1986. A model for predicting the size distribution

- of product from a granulating drum. *Trans. Iron Steel Inst. Japan* 26, 1036–1044.
- Loo, C.E., Williams, R.P., Matthews, L.T., 1992. Influence of material properties on high temperature zone reactions in sintering of iron ore. *Trans. Institutions Min. Metall. C* 101, 7–15.
- Luckos, A., Bunt, J.R., 2011. Pressure-drop predictions in a fixed-bed coal gasifier. *Fuel* 90, 917–921.
- Lv, X.W., Bai, C.G., Zhou, C.Q., Xie, H., Shi, R.M., 2010. New method to determine optimum water content for iron ore granulation 37, 407–413.
- Lwamba, E., Garbers-Craig, A.M., 2008. Control of the grain size distribution of the raw material mixture in the production of iron sinter. *J. South. African Inst. Min. Metall.* 108, 293–300.
- Macdonald, I.F., El-Sayed, M.S., Mow, K., Dullien, F.A.L., 1979. Flow through Porous Media-the Ergun Equation Revisited. *Ind. Eng. Chem. Fundam.* 18, 199–208.
- Maire, E., Buffière, J.Y., Salvo, L., Blandin, J.J., Ludwig, W., Létang, J.M., 2001. On the Application of X-ray Microtomography in the Field of Materials Science. *Adv. Eng. Mater.* 3, 539–546.
- Majidi, B., Melo, J., Fafard, M., Ziegler, D., Alamdari, H., 2015. Packing density of irregular shape particles: DEM simulations applied to anode-grade coke aggregates. *Adv. Powder Technol.* 26, 1256–1262.
- Makridakis, S., Wheelwright, S.C., 1989. *Forecasting Methods for Management*, John Wiley. ed. New York.
- Marigo, M., Stitt, E.H., 2015. Discrete element method (DEM) for industrial applications: Comments on calibration and validation for the modelling of cylindrical pellets. *KONA Powder Part. J.* 32, 236–252.
- Matsumura, T., Maki, T., Amano, S., Sakamoto, M., Iwasaki, N., 2009. Effect of Moisture Absorption Behavior on Optimal Granulation Moisture Value of Sinter Raw Material. *ISIJ Int.* 49, 618–624.
- Mead, S.R., Cleary, P.W., Robinson, G.K., 2012. Characterising the failure and repose angles of irregularly shaped three-dimensional particles using DEM. *Ninth Int. Conf. CFD Miner. Process Ind.* CSIRO, Melbourne, Aust. 1–6.

- Meriam, J.L., Kraige, L.G., 2002. Engineering mechanics dynamics, 5th ed. ed. John Wiley & Sons, New York.
- Mindlin, R.D., 1949. Compliance of elastic bodies in contact. *ASME J. Appl. Mech.* 16, 259 – 268.
- Mitterlehner, J., Loeffler, G., Winter, F., Hofbauer, H., Schmid, H., Zwittag, E., Buegler, T.H., Pammer, O., Stiasny, H., 2004. Modelling and simulation of heat front propagation in the iron ore sintering process. *ISIJ Int.* 44, 11–20.
- Mohanty, R., Mohanty, S., Mishra, B.K., 2016. Study of flow through a packed bed using discrete element method and computational fluid dynamics. *J. Taiwan Inst. Chem. Eng.* 0, 1–10.
- Mora, C.F., Kwan, A.K.H., 2000. Sphericity, shape factor, and convexity measurement of coarse aggregate for concrete using digital image processing. *Cem. Concr. Res.* 30, 351–358.
- Mota, M., Teixeira, J.A., Bowen, W.R., Yelshin, A., 2001. Binary spherical particle mixed beds: Porosity and permeability relationship measurement. *Trans. Filt. Soc.* 1, 101–106.
- Mueller, G.E., 1991. Prediction of radial porosity distributions in randomly packed fixed beds of uniformly sized spheres in cylindrical containers. *Chem. Eng. Sci.* 46, 706–708.
- Mueller, G.E., 1997. Numerical simulation of packed beds with monosized spheres in cylindrical containers. *Powder Technol.* 92, 179–180.
- Nakano, M., Abe, T., Kano, J., Kunitomo, K., 2012. DEM Analysis on Size Segregation in Feed Bed of Sintering Machine. *ISIJ Int.* 52, 1559–1564.
- Nemec, D., Levec, J., 2005. Flow through packed bed reactors: 1. Single-phase flow. *Chem. Eng. Sci.* 60, 6947–6957.
- Newitt, D.M., Conway-Jones, J.M., 1958. A contribution to the theory and practice of Granulation. *Trans. Inst. Chem. Engrs.* 36, 422–442.
- Nijemeisland, M., Dixon, A.G., 2001. Comparison of CFD simulations to experiment for convective heat transfer in a gas–solid fixed bed. *Chem. Eng. J.* 82, 231–246.
- Nijemeisland, M., Dixon, A.G., 2004. CFD study of fluid flow and wall heat transfer in

a fixed bed of spheres. *AIChE J.* 50, 906–921.

- Niven, R.K., 2002. Physical insight into the Ergun and Wen and Yu equations for fluid flow in packed and fluidized beds. *Chem. Eng. Sci.* 57, 527–534.
- Nyembwe, A.M., Cromarty, R.D., Garbers-Craig, A.M., 2016a. Prediction of the granule size distribution of iron ore sinter feeds that contain concentrate and micropellets. *Powder Technol.* 295, 7–15.
- Nyembwe, A.M., Cromarty, R.D., Garbers-Craig, A.M., 2016b. Effect of concentrate and micropellet additions on iron ore sinter bed permeability. *Miner. Process. Extr. Metall.* 125, 178–186.
- Pahl, M., 1975. . Über die Kennzeichnung diskret disperser Systeme und die systematische Variation der Einflußgrößen zur Ermittlung eines allgemeingültigeren Widerstands-gesetzes der Porenströmung. University of Karlsruhe.
- Pal, J., Ghorai, S., Venkatesh, P., Goswami, M.C., Bandyopadhyay, D., Ghosh, S., 2013. Development of fluxed micropellets for sintering utilising iron oxide waste fines. *Ironmak. Steelmak.* 40, 498–504.
- Patankar, S.V., 1980. Numerical heat transfer and fluid flow. Hemisphere Publishing Corp., Washington, DC.
- Pepiot, P., Desjardins, O., 2012. Numerical analysis of the dynamics of two- and three-dimensional fluidized bed reactors using an Euler-Lagrange approach. *Powder Technol.* 220, 104–121.
- Perry, R.H., Green, D.W., Maloney, J.O., 1997. *Chemical Engineer's Handbook*, 7th Editio. ed. Mc Graw Hill, New York.
- Pietsch, W., 2002. *Agglomeration Processes: Phenomena, Technologies, Equipment.* Wiley-VCH, Weinheim, Germany.
- Powers, M.C., 1953. A New Roundness Scale for Sedimentary Particles. *SEPM J. Sediment. Res.* Vol. 23, 117–119.
- Price, M., Murariu, V., Morrison, G., 2007. Sphere clump generation and trajectory comparison for real particles. In: *Proceedings of Fifth International Conference on Discrete Element Methods.* Brisbane, Australia.

- Rankin, W.J., Roller, P.W., 1985. The measurement of void fraction in beds of granulated iron ore sinter feed. *Trans. Iron Steel Inst. Japan* 25, 1016–1020.
- Rankin, W.J., Roller, P.W., Batterham, R.J., 1983. Quasi-particle formation and the granulation of iron ore sinter feeds. In: *Proc. Joint Symp. ISIJ and AIMM*. Tokyo, Japan, pp. 13–28.
- Rankin, W.J., Roller, P.W., Batterham, R.J., 1985. Analysis of the Permeability of Granulated Iron Sinter Feeds Using the Ergun Equation. *Miner. Metall. Process.* 53–59.
- Ricklick, M., Baran, O., 2014. Analytical scaling of DEM particles for efficient packed-bed simulations. In: *10th International Conference on Heat Transfer, Fluid Mechanics and Thermodynamics*. Orlando, Florida, pp. 1131–1137.
- Rocky DEM, I., 2012. User Manuel, Rel. 2.39.
- Rocky DEM, I., 2015. User Manuel, Rel. 3.10.
- Rocky DEM, I., 2016a. Particle Drag Laws Implemented in the Rocky DEMCFD One - Way and Two - Way Coupling Modules.
- Rocky DEM, I., 2016b. A brief introduction to DEM and an overview of contact force models in Rocky, Rel. 3.10.
- Roller, P.W., 1982. Granulation of iron ore. *BHP Tech. Bull.* 26, 44–45.
- Rousé, P.C., Fannin, R.J., Shuttle, D.A., 2008. Influence of roundness on the void ratio and strength of uniform sand. *Géotechnique* 58, 227–231.
- Rumpf, H., 1958. Principles and Methods of granulating. *Chem. Eng. Tech.* 30, 144–158.
- Salman, A.D., Hounslow, M.J., Seville, J.P., 2007. Granulation. In: *Handbook of Powder Technology*. Elsevier Inc., London, UK.
- Santamarina, J., Cho, G., 2004. Soil behaviour: The role of particle shape. *Adv. Geotech. Eng. Proc. Skempton Conf.* 1–14.
- Sastry, K.V.S., Fuerstenau, D.W., 1973. Mechanisms of agglomerate growth in green pelletization. *Powder Technol.* 7, 97–105.
- Schneebeli, G., 1955. Experiences sur la limite de validite de la loi de Darcy et

- l'apparition de la turbulence dans un écoulement de filtration. *La Houille Blanche* 10, 141–149.
- Shatokha, V., Korobeynikov, I., Maire, E., Adrien, J., 2009. Application of 3D X-ray tomography to investigation of structure of sinter mixture granules 36.
- Sherrington, P.J., Oliver, R., 1981. *Granulation*. Heyden & Son, London, UK.
- Shinohara, K., Oida, M., Golman, B., 2000. Effect of particle shape on angle of internal friction by triaxial compression test. *Powder Technol.* 107, 131–136.
- Silva, O.S., Rocha, S.C.S., 2002. Analysis of the growth and agglomerate formation in the granules coating process. In: 13th International Drying Symposium (IDS). Beijing, China.
- Socalici, A., Heput, T., Ardelean, E., Ardelean, M., 2011. Ferrous waste processing by pelletizing, briquetting and mechanically mixed 5, 532–540.
- Standish, N., 1979. *Principles in Burdening and Bell-less Charging*, 1st Ed. ed. Nimaroo Publishers, Wollongong, Australia.
- Su, J.K., Cho, S.W., Yang, C.C., Huang, R., 2002. Effect of sand ratio on the elastic modulus of self-compacting concrete. *J. Mar. Sci. Technol.* 10, 8–13.
- Sun, J., Battaglia, F., Subramaniam, S., 2006. Dynamics and structures of segregation in a dense, vibrating granular bed. *Phys. Rev. E* 74, 13–14.
- Taylor, M.A., Garboczi, E.J., Erdogan, S.T., Fowler, D.W., 2006. Some properties of irregular 3-D particles. *Powder Technol.* 162, 1–15.
- Thakur, S.C., Ooi, J.Y., Ahmadian, H., 2016. Scaling of discrete element model parameters for cohesionless and cohesive solid. *Powder Technol.* 293, 130–137.
- Thomas, P.A., Bray, J.D., 1999. Capturing Nonspherical Shape of Granular Media with Disk Clusters. *J. Geotech. Geoenvironmental Eng.* 125, 169–178.
- Thornton, A., Weinhart, T., Luding, S., Bokhove, O., 2012. Modeling of particle size segregation: Calibration using the Discrete Particle Method. *Int. J. Mod. Phys. C* 23, 1240014.
- Thornton, C., Ning, Z., 1998. A theoretical model for the stick/bounce behaviour of adhesive, elastic-plastic spheres. *Powder Technol.* 99, 154–162.

- Tomas, J., 2007. Adhesion of ultrafine particles—A micromechanical approach. *Chem. Eng. Sci.* 62, 1997–2010.
- Van Burkalow, A., 1945. Angle of repose and angle of sliding friction: An experimental study. *Bull. Geol. Soc. Am.* 56, 669–707.
- Venkataramana, R., Gupta, S.S., Kapur, P.C., 1999. A combined model for granule size distribution and cold bed permeability in the wet stage of iron ore sintering process. *Int. J. Miner. Process.* 57, 43–58.
- Vidal, R., Meunier, G., Poot, E., 1985. R. Vidal, G. Meunier, E. Poot,. In: *Agglomeration. ISS-AIME*, p. 181.
- Voice, E.W., Brooks, S.H., Gledhill, P.K., 1953. The permeability of sinter beds. *J. Iron Steel Inst.* 174, 136–139.
- Vollmari, K., Oschmann, T., Wirtz, S., Kruggel-Emden, H., 2015. Pressure drop investigations in packings of arbitrary shaped particles. *Powder Technol.* 271, 109–124.
- Wadell, H., 1932. Volume, shape, and roundness of rock particles. *J. Geol.* 40, 443–451.
- Wadell, H., 1933. Sphericity and roundness of rock Particles. *J. Geol.* 41, 310–331.
- Wadell, H., 1934. Shape determination of large sedimental rock fragments. *Pan- Am. Geol.* 61, 187–220.
- Walton, O.R., 1994. Numerical simulation of inelastic frictional particle–particle interaction. In: M.C. Roco (Ed.), *Particulate Two-Phase Flow*. Butterworth-Heinemann, London, UK, pp. 884–911.
- Walton, O.R., Braun, R.L., 1993. Simulation of rotary-drum and repose tests for frictional spheres and rigid sphere clusters. In: *5th Joint DOE/NSF Workshop on Flow of Particulates*. Ithasa, New York.
- Wang, D., Servin, M., Berglund, T., Mickelsson, K.-O., Rönnbäck, S., 2015. Parametrization and validation of a nonsmooth discrete element method for simulating flows of iron ore green pellets. *Powder Technol.* 283, 475–487.
- Waters, A.G., Litster, J.D., Nicol, S.K., 1989. A mathematical model for the prediction of granule size distribution for multicomponent sinter feed. *ISIJ Int.* 29, 274–283.

- Wen, C.Y., Yu, Y.H., 1966. A generalized method for predicting the minimum fluidization velocity. *AIChE J.* 12, 610–612.
- Westman, A.E.R., 1936. The packing of particles: Empirical equations for intermediate diameter ratios. *J. Am. Ceram. Soc.* 19, 127–129.
- White, H.E., Walton, S.F., 1937. Particle packing and particle shape. *J. Am. Ceram. Soc.* 20, 155–166.
- Wildeboer, W.J., Litster, J.D., Cameron, I.T., 2005. Modelling nucleation in wet granulation 60, 3751–3761.
- Williams, J.R., Pentland, A.P., 1992. Supraquadratics and modal dynamics for discrete elements in interactive design. *Eng. Comput.* 9, 115–127.
- Williams, S.R., Philipse, A.P., 2003. Random packings of spheres and spherocylinders simulated by mechanical contraction. *Phys. Rev. E* 67, 1–9.
- Winterberg, M., Tsotsas, E., 2000. Impact of tube-to-particle-diameter ratio on pressure drop in packed beds. *AIChE J.* 46, 1084–1088.
- Witt, K.J., Brauns, J., 1983. Permeability-Anisotropy Due to Particle Shape. *J. Geotech. Eng.* 109, 1181–1187.
- Wooten, J., 1998. Dense and sock catalyst loading compared. *Oil Gas J.* 12, 66–70.
- Wright, D.E., 1968. Nonlinear Flow Through Granular Media. *J. Hydraul. Div.* 94, 851–872.
- Yu, A.B., Standish, N., 1988. An analytical—parametric theory of the random packing of particles. *Powder Technol.* 55, 171–186.
- Yu, A.B., Standish, N., 1993. Characterisation of non-spherical particles from their packing behaviour. *Powder Technol.* 74, 205–213.
- Zhang, D.Z., Zou, Q., VanderHeyden, W.B., Ma, X., 2008. Material point method applied to multiphase flows. *J. Comput. Phys.* 227, 3159–3173.
- Zhao, J., Shan, T., 2013. Coupled CFD – DEM simulation of fluid – particle interaction in geomechanics. *Powder Technol.* 239, 248–258.
- Zheng, J., Carlson, W.B., Reed, J.S., 1995. The packing density of binary powder mixtures. *J. Eur. Ceram. Soc.* 15, 479–483.

- Zhou, H., Zhou, M., Cheng, M., Guo, W., Cen, K., 2017. Experimental study and X-ray microtomography based CFD simulation for the characterization of pressure drop in sinter bed. *Appl. Therm. Eng.* 112, 811–819.
- Zhou, Y.C., Wright, B.D., Yang, R.Y., Xu, B.H., Yu, A.B., 1999. Rolling friction in the dynamic simulation of sandpile formation. *Phys. A Stat. Mech. its Appl.* 269, 536–553.
- Zhou, Y.C., Xu, B.H., Yu, A.B., Zulli, P., 2001. Numerical investigation of the angle of repose of monosized spheres. *Phys. Rev. E* 64, 1–7.
- Zhu, H.P., Yu, A.B., 2003. The effects of wall and rolling resistance on the couple stress of granular materials in vertical flow. *Physica A* 325, 347–360.
- Zhu, H.P., Zhou, Z.Y., Yang, R.Y., Yu, A.B., 2008. Discrete particle simulation of particulate systems: A review of major applications and findings. *Chem. Eng. Sci.* 63, 5728–5770.
- Zingg, T., 1935. Beitrag zur Schotteranalyse. *Mineral. und Petrol. Mitteilungen* 15, 39–140.
- Zou, R., Yu, A.B., 1995. The packing of spheres in a cylindrical container: the thickness effect. *Chem. Eng. Sci.* 50, 1504–1507.

Appendix A

Chemical analysis of iron ores and concentrate and raw material mixtures

Table A.1. Chemical composition (mass %) of raw materials

	Ore 1	Ore 2	Concen- trate	Micro- pellets	Return fines	Coke	Lime	Dolomite
Fe (tot)	63.60	63.20	64.80	65.60	54.55	1.20	1.08	0.74
FeO	0.10	0.10	0.04	4.40	0.22	0.81	0.00	0.90
Fe ₂ O ₃	90.80	90.30	92.60	90.50	77.76	0.82	1.54	0.06
P	0.04	0.06	0.06	0.01	0.04	0.04	0.00	0.00
S	0.00	0.01	0.01	0.01	0.07	0.80	0.02	0.00
K ₂ O	0.09	0.24	0.27	0.01	0.17	0.24	0.06	0.03
Na ₂ O	0.01	0.02	0.03	0.02	0.03	0.12	0.01	0.06
CaO	0.33	0.27	0.14	0.02	11.79	0.74	53.20	29.60
MgO	0.41	0.07	0.06	0.04	2.05	0.22	1.12	20.10
MnO	0.44	0.05	0.08	0.16	0.39	0.05	0.64	0.81
Al ₂ O ₃	0.84	1.72	1.56	0.13	1.42	3.79	0.14	0.22
SiO ₂	5.54	6.01	3.72	3.30	6.06	10.10	0.83	2.61
LOI	1.06	1.05	1.14	1.18	0.00	81.60	42.60	45.30

*LOI: Loss of ignition

Table A.2. Particle size distribution (mass %) of raw materials

Sieve size (mm)	Ore 1	Ore 2	Concen- trate	Micro- pellets	Return fines	Coke	Lime	Dolomite
4.75	17.62	13.73	0.07	0.29	0.98	10.10	0.17	1.07
2.00	28.64	51.45	0.24	45.32	55.22	28.10	20.65	19.02
1.00	14.24	18.37	0.17	41.06	22.77	17.20	21.73	16.21
0.50	11.77	7.84	0.58	1.40	11.00	17.66	14.44	27.97
0.25	8.85	5.23	2.23	0.80	5.02	11.14	9.18	16.41
0.125	11.17	2.37	17.76	2.13	2.36	7.50	14.99	11.31
0.63	5.80	0.93	52.87	4.22	1.61	5.12	17.03	7.33
Pan	1.91	0.08	26.09	4.79	1.05	3.17	1.81	0.68
	100.00	100.00	100.00	100.00	100.00	100.00	100.00	100.00

Table A.3. Chemical composition (mass %) of raw material mixtures

	Base mixture	Mixture with concentrate				Mixture with micropellets			
		10%	20%	30%	40%	10%	20%	30%	40%
Fe (tot)	48.23	48.50	48.78	49.05	49.34	48.57	48.91	49.27	49.63
FeO	0.19	0.19	0.19	0.19	0.18	0.43	0.67	0.91	1.16
Fe ₂ O ₃	68.75	69.13	69.54	69.92	70.34	69.06	69.37	69.70	70.04
P	0.04	0.04	0.04	0.04	0.04	0.04	0.03	0.03	0.03
S	0.06	0.06	0.06	0.06	0.06	0.06	0.06	0.06	0.06
K ₂ O	0.15	0.16	0.16	0.17	0.18	0.14	0.14	0.13	0.12
Na ₂ O	0.03	0.03	0.03	0.03	0.03	0.03	0.03	0.03	0.03
CaO	10.42	10.24	10.05	9.86	9.66	10.21	10.00	9.78	9.55
MgO	1.81	1.81	1.81	1.81	1.80	1.81	1.80	1.80	1.79
MnO	0.34	0.33	0.32	0.31	0.30	0.34	0.33	0.33	0.32
Al ₂ O ₃	1.26	1.28	1.30	1.32	1.34	1.20	1.14	1.08	1.02
SiO ₂	5.36	5.26	5.16	5.06	4.97	5.24	5.12	5.00	4.88
LOI	11.43	11.31	11.18	11.06	10.93	11.30	11.16	11.01	10.86
Basicity									
CaO/SiO ₂	1.95	1.95	1.95	1.95	1.95	1.95	1.95	1.96	1.96

Appendix B

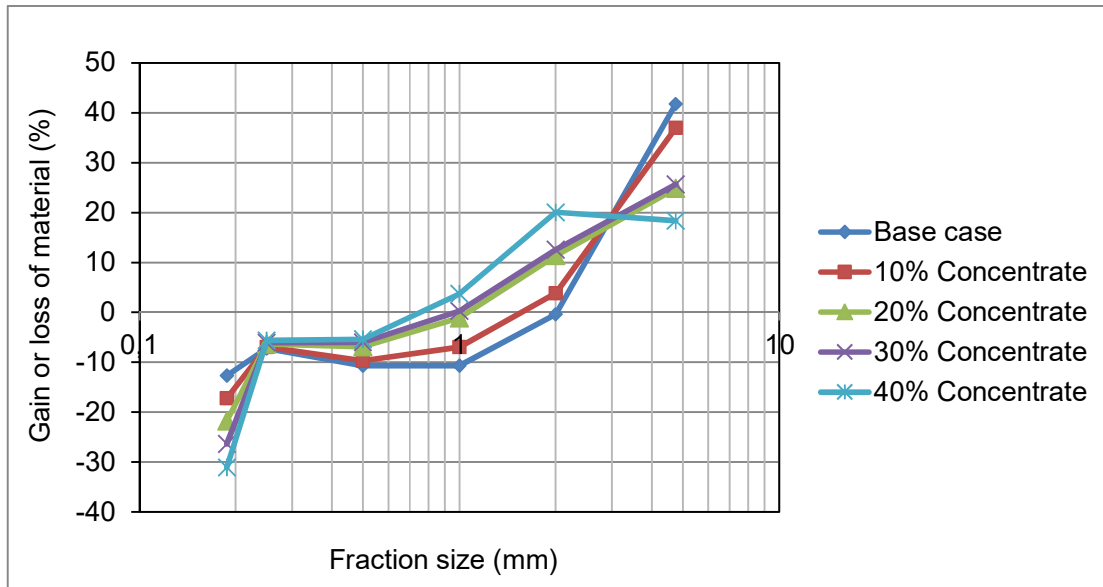
Material transfer between the size fractions

Granulation processes are based on the elimination of fine particles that can adhere onto coarse ones and consequently form big granules. This process is carried out by transferring material between different granulometric classes. The gain and loss of material is determined by comparing the mass fractions of each granulometric class before and after granulation. By plotting the variation of material transfer against the size fraction, a size limit X was defined as an imaginary size fraction at which the variation of the material transfer between granulometric classes switches from gain to loss. In iron ore granulation, the particles with size less than the size limit are considered as adhering fines (Hsieh, 2005; Lwamba and Garbers-Craig, 2008).

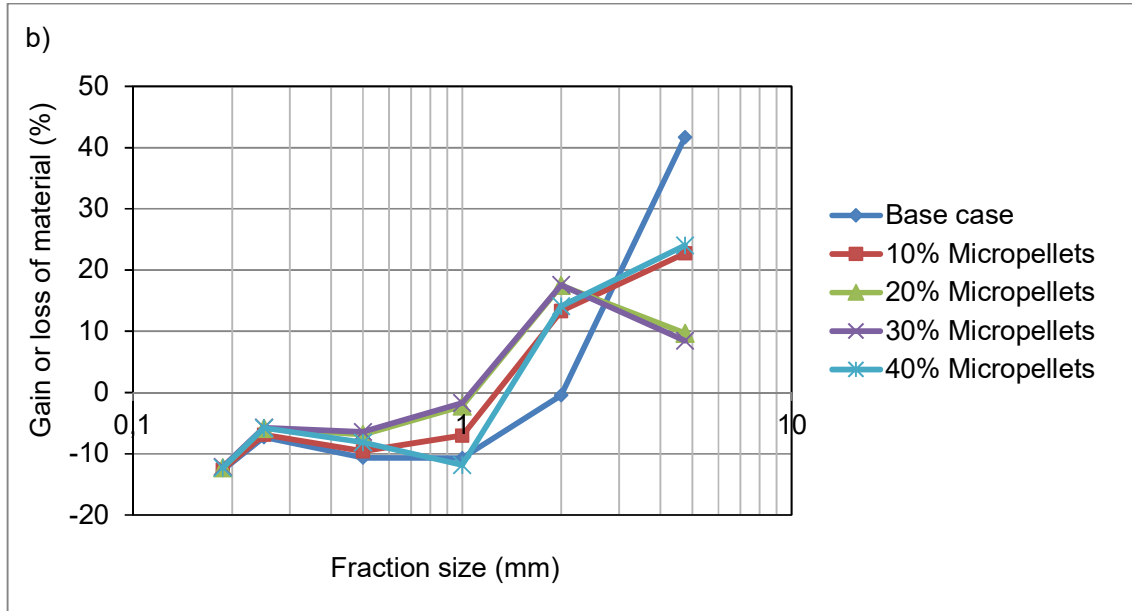
The gain and loss of material transfer between the size fractions before and after granulation were calculated for mixtures with concentrate and micropellet addition at optimum moisture content (Table B.1 and Figure B.1). The size limit X corresponds to the sieve size at which there is no gain and loss. The addition of concentrate and micropellets to base mixture shifts the material transfer curve from right to left. This means that the size fraction defined as finer material (adhering fines) will consequently decrease with an increase in concentrate and micropellet fraction in the ore mixture (Figure B.2).

Table B.1. Gain or loss and size limit X

Mixtures	Gain or loss of material transfer (mass %)						Size limit X mm
	+4.75 mm	+2.00 mm	+1.00 mm	+0.50 mm	+0.25 mm	<0.125 mm	
Base case	41.71	-0.42	-10.71	-10.68	-7.26	-12.67	2
10%concentrate	36.98	3.83	-6.96	-9.70	-6.95	-17.20	1.5
20%concentrate	24.85	11.37	-1.14	-6.91	-6.35	-21.78	1.05
30%concentrate	25.66	12.59	0.24	-6.02	-6.08	-26.37	1
40%concentrate	18.36	20.06	3.68	-5.37	-5.65	-31.10	0.72
10%Micropellets	22.74	13.31	-7.03	-9.59	-6.89	-12.59	1.1
20%Micropellets	9.70	17.50	-2.20	-6.88	-5.87	-12.26	1.02
30%Micropellets	8.43	17.57	-1.72	-6.42	-5.76	-12.15	1.02
40%Micropellets	24.04	14.10	-11.86	-8.16	-5.78	-12.30	1.2



(a)



(b)

Figure B.1. Variation of material transfer between size fractions of mixtures with a) concentrate and b) micropellet addition

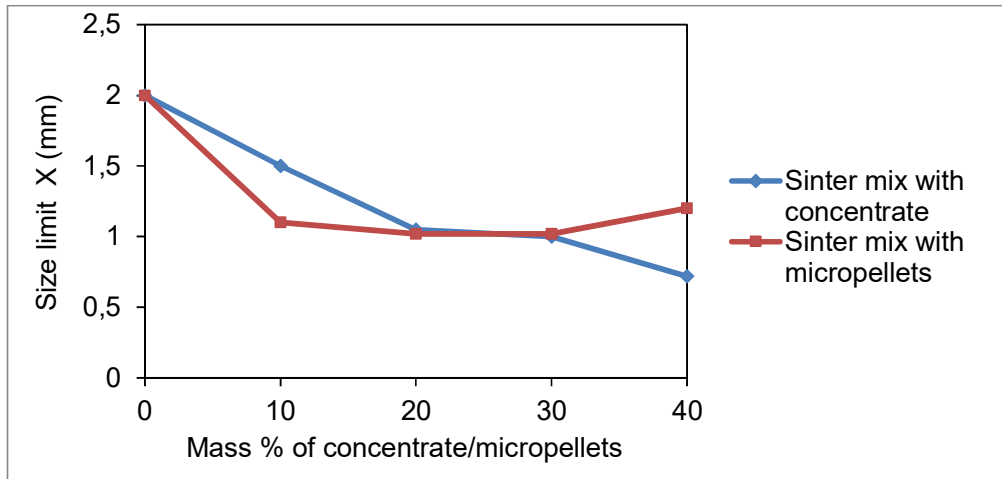


Figure B.2. Variation of the size limit X with concentrate and micropellet addition

Another parameter, E_x (%), was defined to measure the efficiency of elimination of adhering fines with size fraction less than X mm. This coefficient was calculated by the relation (Lwamba and Garbers-Craig, 2008; Li-Heng, 2005):

$$E_x = 100 * ((\% < X)_{BG} - (\% < X)_{AG}) / (\% < X)_{BG}$$

Eq. A.1

where $(\% < X)_{AG}$ and $(\% < X)_{BG}$ are mass fractions of particle sizes less than X after and before granulation respectively.

The efficiency of granulation for the examined mixtures was calculated and plotted in Figure B.3. It can be seen that the efficiency increases with addition of concentrate and micropellets. This could potentially increase the permeability of the corresponding mixtures. However, the fine particles were shared between different mechanisms: auto-layering of coarse particles and micropellets (granules of Group I) and coalescence of microgranules (granules of Group II). This was identified as factors that hinder the growth of granules and improvement of the bed permeability (Section 3.2.4).

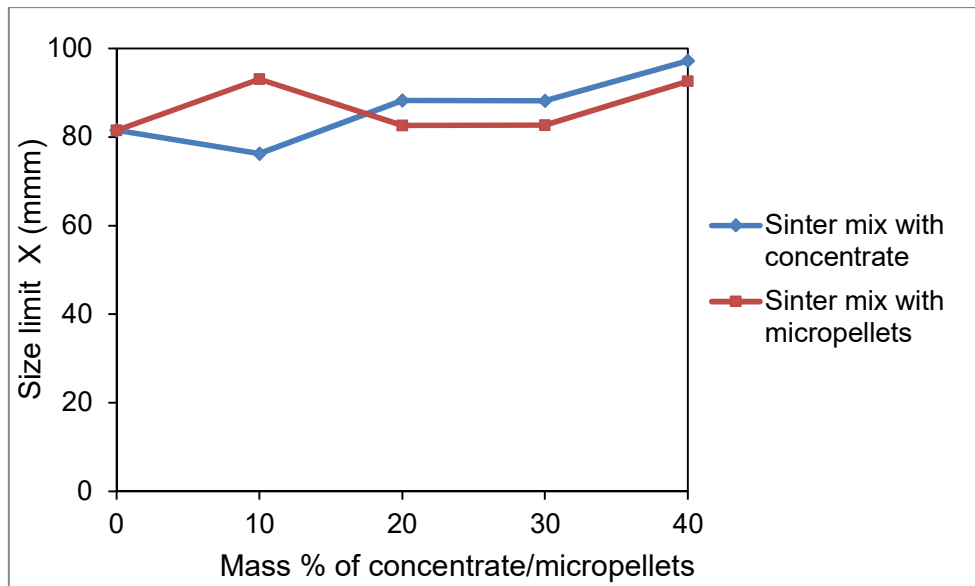
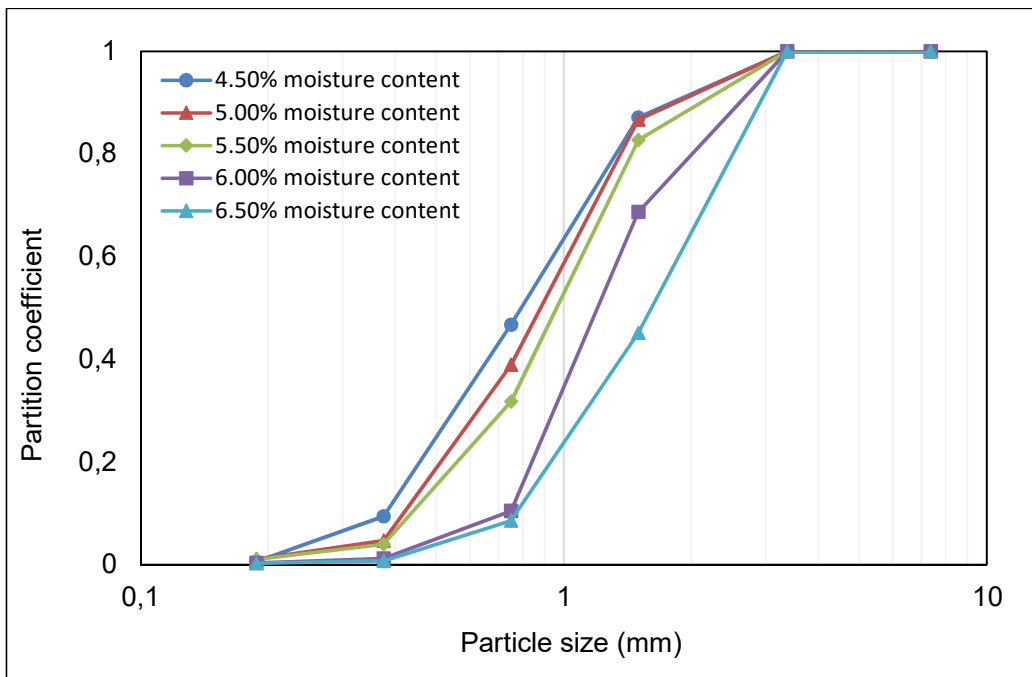


Figure B.3. Variation of the efficient with addition of concentrate and micropellets

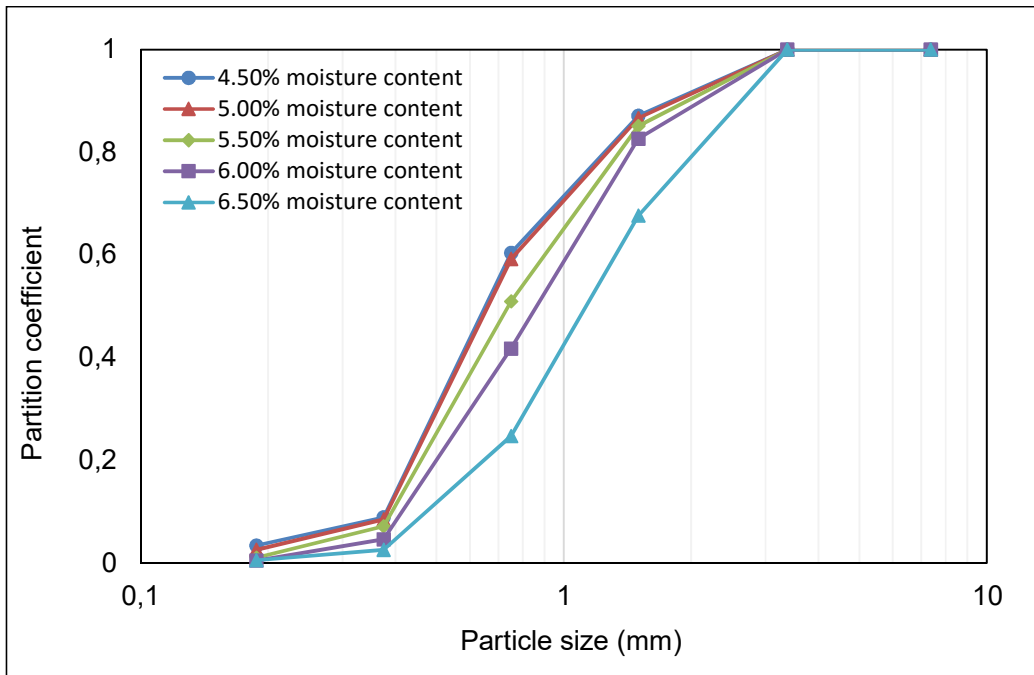
Appendix C

Particle partition distribution

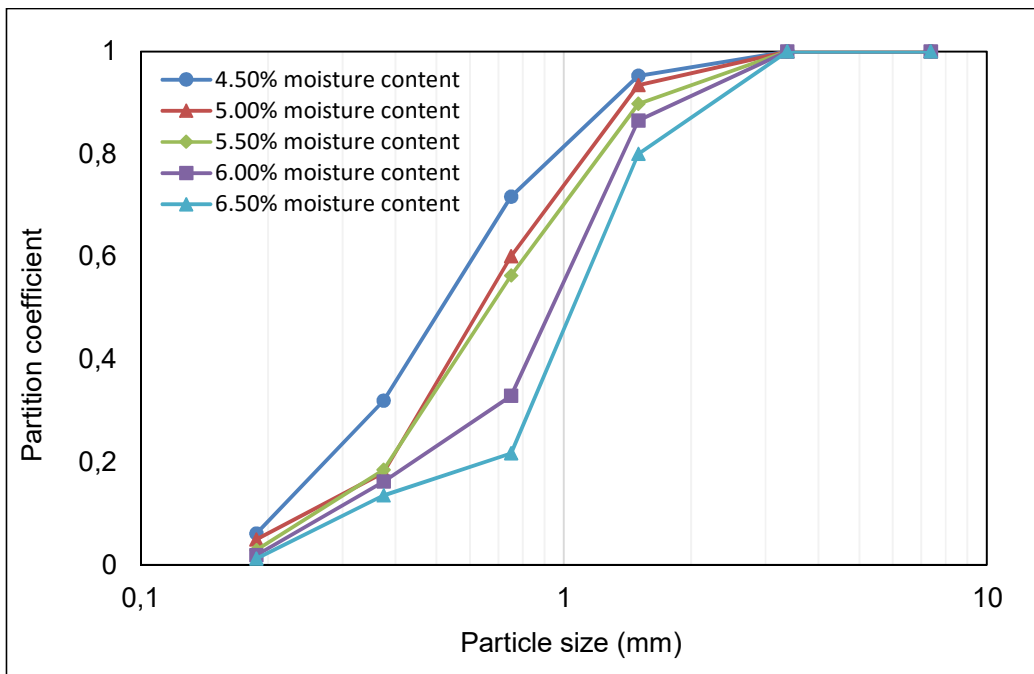
The effect of the moisture content on the particle partition distribution is shown in Figure C.1. The partition distribution curves shifted from the left to the right hand side with an increase in moisture. Similar observations were reported in previous studies (Litster et al., 1986; Litster and Waters, 1986).



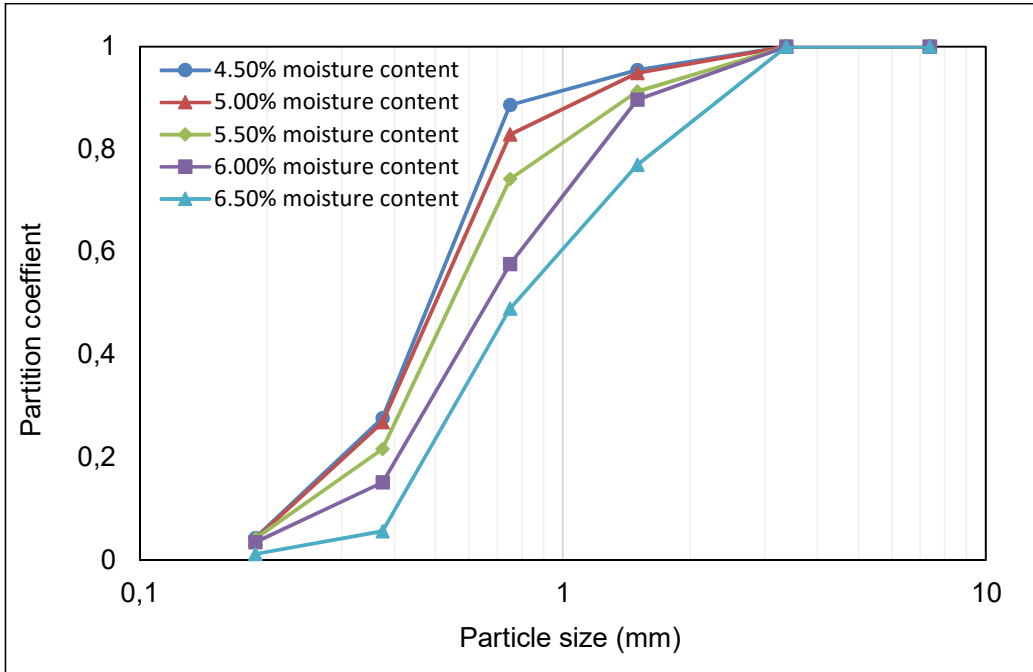
(a)



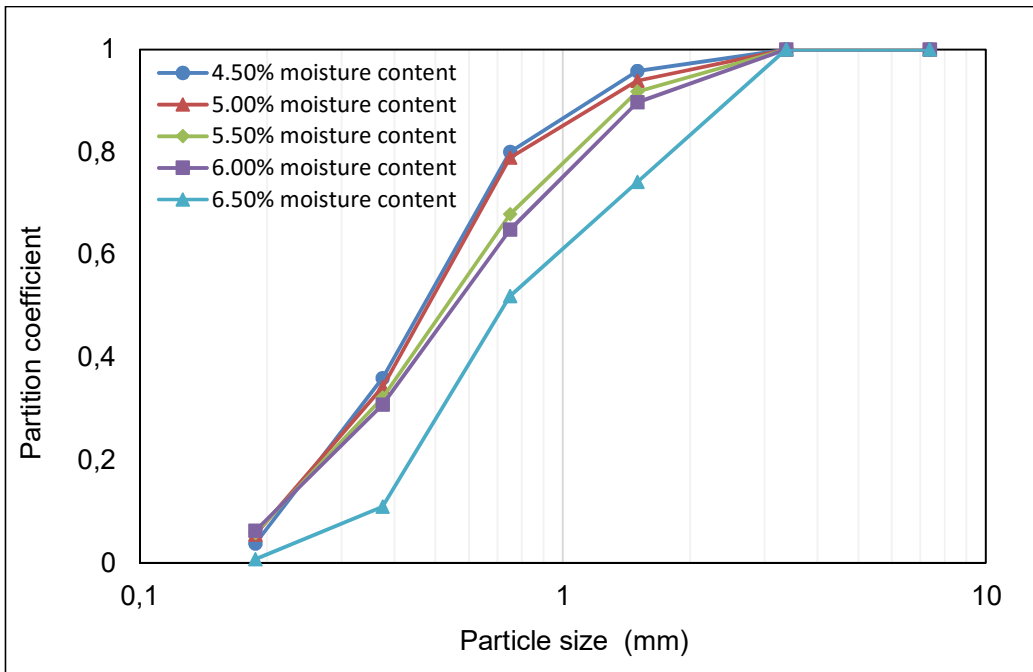
(b)



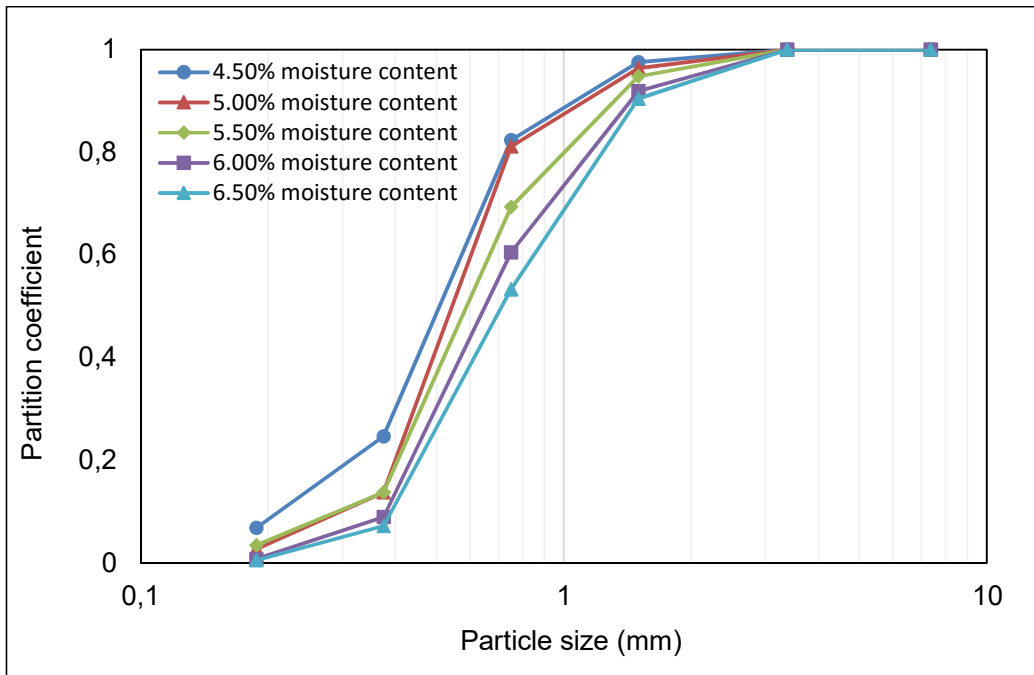
(c)



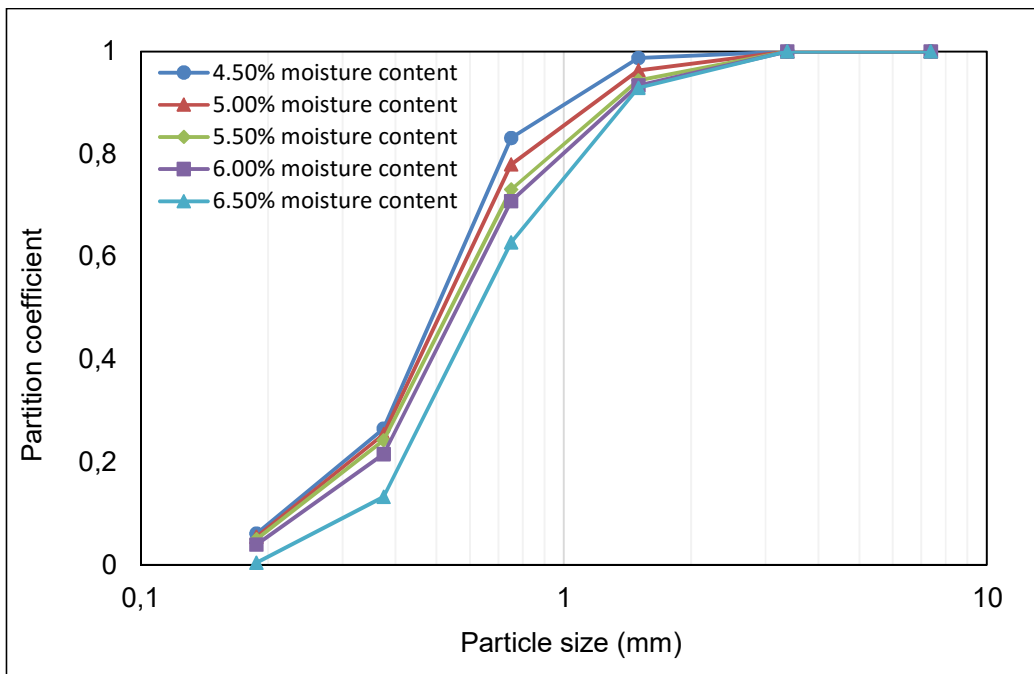
(d)



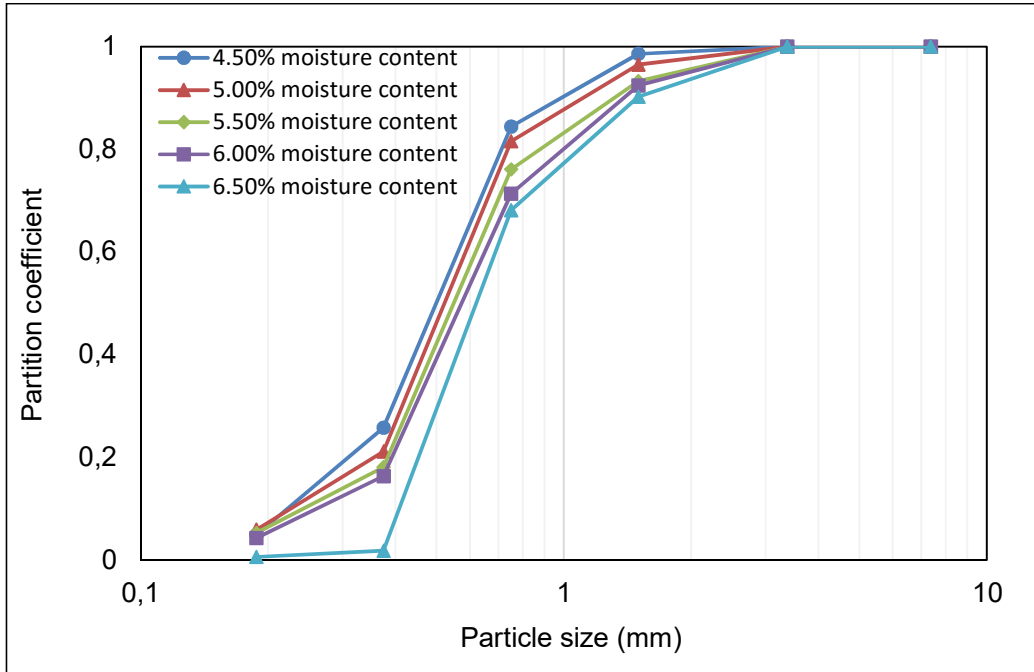
(e)



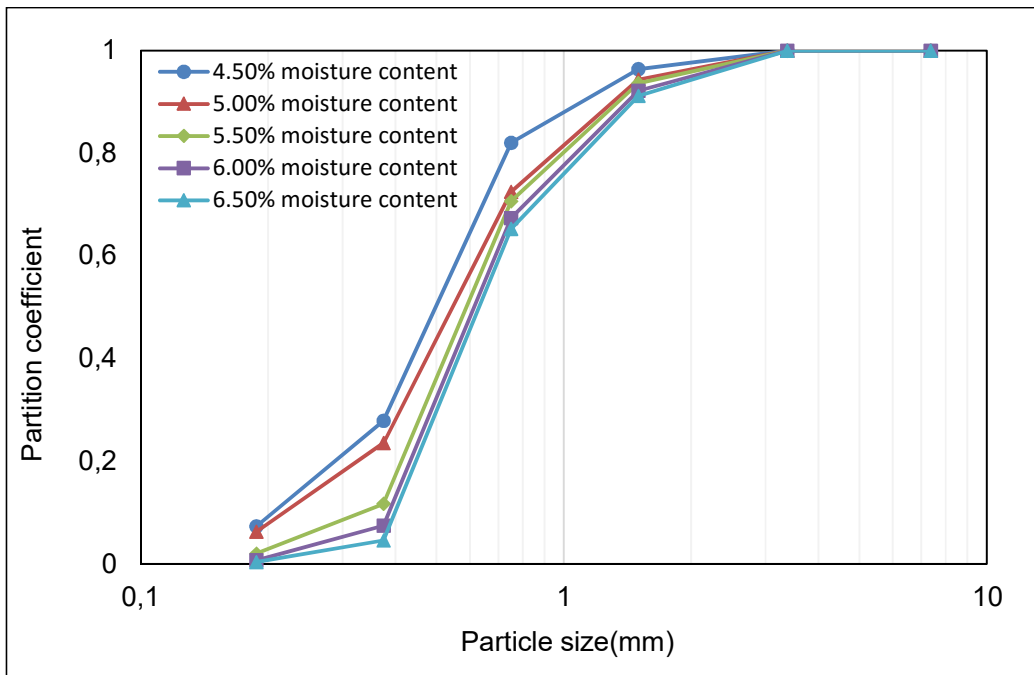
(f)



(g)



(h)



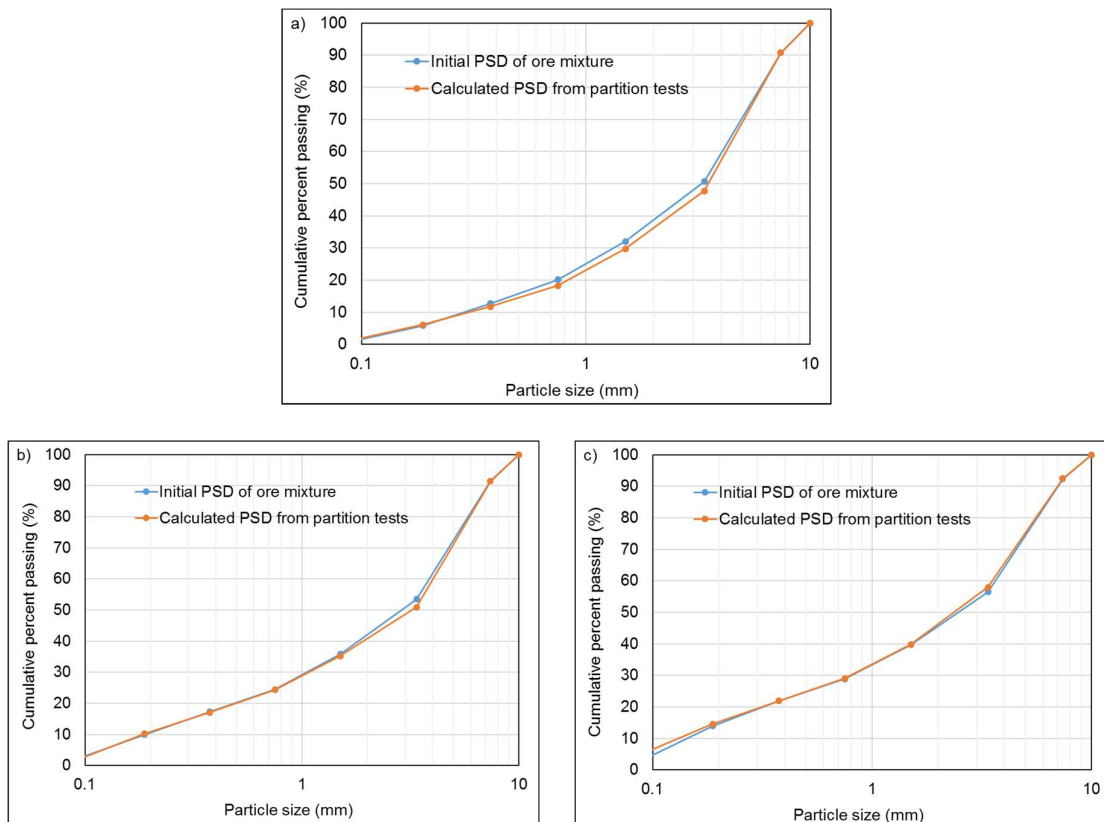
(i)

Figure C.1. Partition distribution of (a) base mixture and mixtures with b) 10% concentrate, c) 20% concentrate, d) 30% concentrate, e) 40% concentrate, f) 10% micropellets, g) 20% micropellets, h) 30% micropellets and i) 40% micropellets

Appendix D

Comparison between initial particle size distributions (PSD) and calculated particle size distributions from partition tests for raw material mixtures with concentrate and micropellets

Good correlations were achieved between the initial size distributions of primary mixtures and sizing distributions of primary materials that were back calculated from partition tests (Figure D.1). Deviations between the two sets of data were not significant.



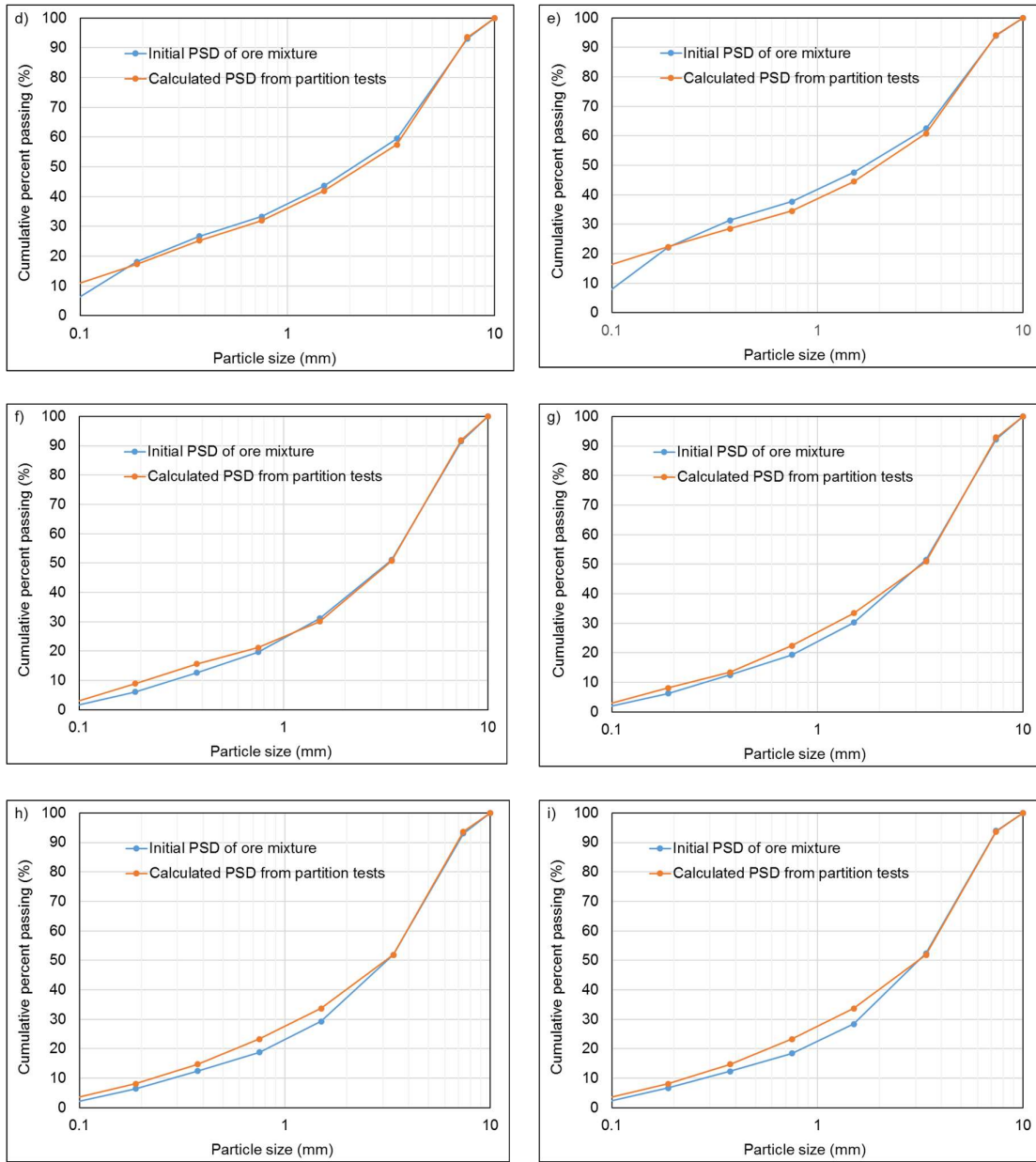


Figure D.1. Initial PSD of primary mixtures and calculated PSD from partition testing results (a) base mixture and mixtures with b) 10% concentrate, c) 20% concentrate, d) 30% concentrate, e) 40% concentrate, f) 10% micropellets, g) 20% micropellets, h) 30% micropellets and i) 40% micropellets

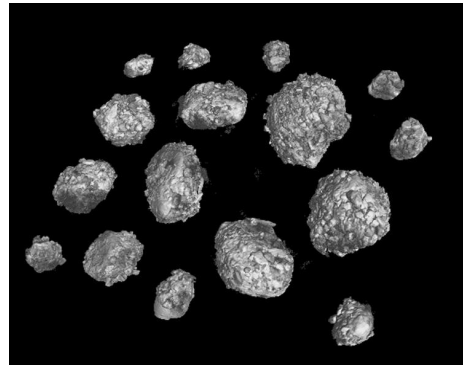
Appendix E

X-ray microtomography images of granules from granulated mixtures with addition of concentrate and micropellets

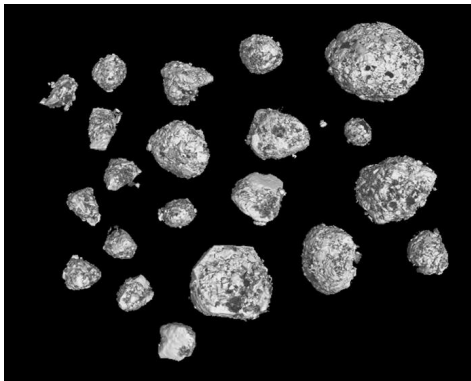
The addition of concentrate and micropellets to the base mixture led to the formation of more spherical particles (Figure E.1).



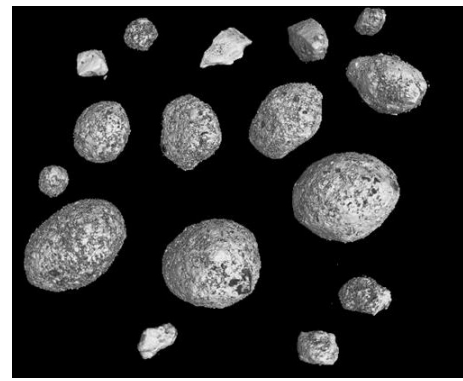
10% Concentrate



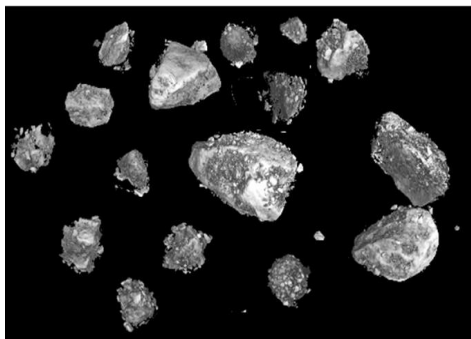
20% Concentrate



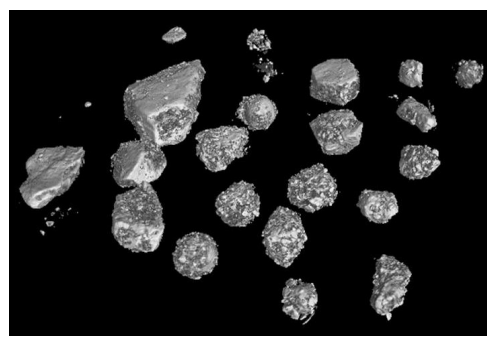
30% Concentrate



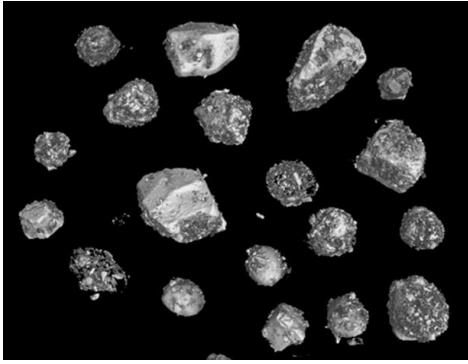
40% Concentrate



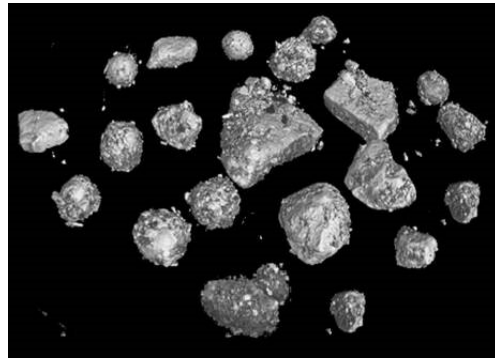
10% Micropellets



20% Micropellets



30% Micropellets



40% Micropellets

Figure E.1. X-ray microtomography images of selected granules from mixtures with addition of concentrate and micropellets

Appendix F

Validation of the pressure drop through glass beads: Two-way coupling simulation

The validation of the pressure drop through glass beads was previously performed using a one-way coupling model. The Rocky DEM 2.39 and Ansys CFD 14.5 coupling was used to calculate the pressure drop. In this approach, the particles were assumed affecting the fluid flow and the results were presented in Chapter 6.

The upgrade of Rocky DEM from version 2.39 to 3.9 resulted in the calculation of the pressure drop through the same glass beads using a two-way coupling model. This approach uses a neighbour cell averaging procedure whereby the mesh size is set to be larger than the largest particle size throughout the simulation domain (Anderson and Jackson, 1967; Pepiot and Desjardins, 2012; Zhang et al., 2008). In the Rocky DEM – CFD two-way coupling scheme, both solvers can run in parallel, which is a gain in simulation time if the solvers do not compete for resources (Rocky DEM, 2015).

In the two-way coupling simulation, a CFD case file was created from the Eulerian multiphase setup where the number of fluid phases was 2 (air was the first phase while the second one was the particle phase). The mesh size was selected to be 36 mm. Particles were regarded as the continuous phase and their location was described by the spatial distribution of the mass percentages of the particles. The particle mass percentage and velocities were set to 0 during the case initialization, and should come from Rocky DEM solver. The Phase Coupled SIMPLE method and First Order were used as pressure velocity coupling method and transient scheme respectively. Solution data export was set to CFD-post processing in order to enable transient solution files as usually done in Fluent.

The pressure drops through glass beads calculated by DEM – CFD one-way and two-way coupling simulation were comparable with a deviation within 10% (Table F.1). This means that the two-way coupling method could be used for further simulations.

Table F.1. Comparison between the pressure drop predicted by one-way and two-way coupling simulation

Packed bed	Pressure drop (Pa/m)		Deviation (%)
	One-way coupling	Two-way coupling	
Monosize mixture			
3 mm glass bead	19665	18473	6.06
6 mm glass bead	19865	18654	6.10
Binary mixture			
75% 3 mm, 25% 6 mm glass bead	16470	16733	-1.60
50% 3 mm, 50% 6 mm glass bead	17000	16718	1.66
25% 3mm, 75% 6mm glass bead	17140	16583	3.25

Appendix G

Comparison of the predicted and measured pressure drops through granulated mixtures

Table G.1. Comparison of measured pressure drop and predicted pressure drop for different adhesion force fractions

Force fraction (%)	Predicted pressure drop (Pa)	Measured pressure drop (Pa)	Deviation (%)
0	6971	9806	29.46
5	10333	9806	- 5.38
10	10431	9806	- 6.38
20	10302	9806	- 5.06
50	10196	9806	- 3.97

Table G.2. Comparison between the measured and predicted pressure drops for selected granule shapes

Granule shape	Predicted pressure drop (Pa)	Measured pressure drop (Pa)	Deviation (%)
Sphere	10431	9806	- 6.37
Rounded polyhedron (25 corners)	6053	9806	38.27
Rounded polyhedron (4 corners)	4899	9806	50.04
Rounded polygon (25 corners)	9299	9806	5.16
Rounded polygon (4 corners)	9976	9806	- 1.74

Table G.3. Comparison of the pressure drop as predicted through DEM – CFD simulations and experimental measurement

Mixtures	Number of particles	Predicted pressure drop (Pa)	Measured pressure drop (Pa)	Deviation (%)
Base case	61678	10199	9806	- 4.01
10% Concentrate	76789	10734	9806	- 9.46
20% Concentrate	118782	10449	9806	- 6.56
30% Concentrate	128064	9714	9806	0.93
40% concentrate	133748	9838	9806	- 0.33
10% Micropellets	88850	9425	9806	3.89
20% Micropellets	134329	10449	9806	- 6.56
30% Micropellets	140747	10727	9806	- 9.39
40% Micropellets	86385	10581	9806	- 7.90

Appendix H

Particle size segregation at the top and base of the packed beds

DEM simulation of binary systems results in a slight asymmetry in segregation of the particle size at the top and base of the packed bed (Thornton et al., 2012). A thick pure layer of large particles forms at the top of the packed bed. At the base of the packing, small particles rearrange as a thin pure layer. In this study, similar segregation was obtained for granulated mixtures. The segregation was noticeable at the top of the packed beds for the base mixture and mixtures with 10% concentrate and micropellets, while non-existent in sinter beds with 40% concentrate and micropellets (Figure H.1). It is clear that the decrease in +4.75 mm size reduced the segregation at the top of the sinter bed.

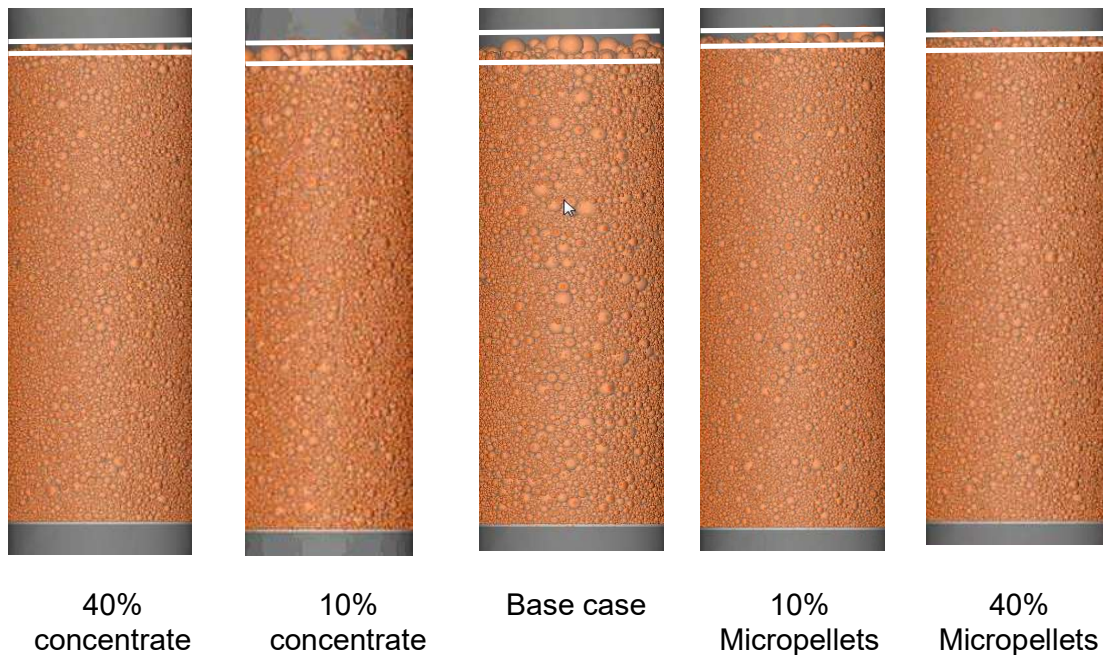


Figure H.1. Asymmetric segregation of particle size in the sinter beds: base mixture and mixtures with 10% and 40% concentrate and micropellets.